ACTIVATION AND SUPPRESSION OF NON-BASAL SLIP AND EXTENSION TWINNING IN MAGNESIUM AND MAGNESIUM ALLOYS

A Dissertation

by

DEXIN ZHAO

Submitted to the Graduate and Professional School of
Texas A&M University
in partial fulfillment of the requirements for the degree of

DOCTOR OF PHILOSOPHY

Chair of Committee,	Kelvin Xie
Committee Members,	Ibrahim Karaman
	Michael Demkowicz
	Dinakar Sagapuram
Head of Department,	Ibrahim Karaman

December 2021

Major Subject: Materials Science and Engineering

ABSTRACT

Magnesium (Mg) and its alloys are promising lightweight and high specific strength structural materials, especially for transportation and aerospace applications. However, pure Mg and many Mg alloys exhibit low room-temperature ductility and formability, which is due to the low-symmetry hexagonal close-packed crystal structure and high plastic anisotropy. Therefore, a comprehensive understanding of the fundamental deformation behavior in Mg and its alloys is critical to further improve the mechanical performance of Mg. In this dissertation, advanced characterization techniques (scanning electron microscopy, transmission electron microscopy, etc.) were used to study the activation and suppression of non-basal slips (non-basal $< a >$ and $< c + a >$) and $\{10\bar{1}2\} < \bar{1}01\bar{1} >$ extension twinning in deformed pure Mg and Mg alloys.

In the first part, the effect of Schmid factor was examined on the activation and suppression of $< c+a >$ dislocation and extension twinning. Textured Mg-3Al-1Zn (AZ31) alloy was selected as the model material. Regarding $< c + a >$ dislocations, statistical analyses on the normal-direction compressed AZ31 revealed that the activation and suppression of $< c+a >$ dislocations in individual grains are primarily dictated by the overall texture rather than the crystallographic orientation of each grain. (Global texture prevails!) Regarding extension twinning, statistical analyses on the deformed Mg under multiply deformation conditions (normal-direction compression and tension, rolling-direction compression and tension, and 45° compression) revealed extension twinning generally obeys the Schmid law for individual grains rather than the global stress state that favors extension twinning or not. (Schmid factor of individual grain prevails!)

In the second part, the effect of non-rare earth (RE) alloying was investigated on the activation and suppression of $< c + a >$ dislocation and extension twinning. Moreover, the operation of specific deformation mode on the sample ductility was discussed. Non-RE Mg (pure Mg and AZ31) with similar initial microstructures (i.e., grain size and texture) were chosen. To uncover the fundamental mechanisms for the much improved ductility in AZ31, statistical analyses on the pure Mg and AZ31 after rolling-direction tension at different strain levels were performed. The

observations revealed a significant disparity of non-basal dislocation activities between the pure Mg and AZ31. For the pure Mg, $< c + a >$ dislocations were activated since the early stage of plastic deformation. For AZ31, $< c+a >$ dislocations were largely absent at all strain levels, even in the strain-to-failure samples. The promotion of the non-basal $< a >$ dislocation activities and the suppression of $< c+a >$ dislocations in AZ31 are expected to offer more sustainable hardening, which could elucidate the absence of apparent shear banding and much-improved ductility in AZ31 compared to pure Mg.

In the third part, the effect of RE alloying was investigated on the activation and suppression of $< c+a >$ dislocation and extension twinning, and the influence on sample ductility was discussed. The microstructure of a newly developed Mg RE alloy (Mg–2Zn-0.3Ca-0.2Ce-0.1Mn) alloy with an exceptionally high tensile ductility was characterized. Compared with the pure Mg and AZ31 alloy microstructure at the same deformation condition in the second part, our results revealed that the high ductility of the ZXEM2000 could be attributed to four key factors: weaker texture, finer grain size, reduced twinning, and increased cross-slip frequency of $< c + a >$ dislocations.

Taken together, this dissertation explores the roles of Schmid factor and alloying on the operation of non-basal slip and extension twinning in Mg and Mg alloy. Both above deformation mechanisms have a significant impact on the ductility of Mg and Mg alloys. The fundamental mechanisms uncovered in this work are anticipated to help guide the future Mg alloy design, especially in the area of simultaneously achieving high strengthen, high ductility, and improved formability.

DEDICATION

To my parents for always loving and supporting me.

ACKNOWLEDGMENTS

Looking back to this four years' journey from 2017 to 2021, I was able to live and learn in this beautiful campus, Texas A&M University, to finish the "specialist" target in my life, Doctors of Philosophy, which acts as a good ending to my twenty-two years learning experience in school. Meanwhile, I have the chance to live and work with a lot of friendly people, who helped and guided me during this journey. I feel so lucky to meet all these people in my late twenties.

Foremost, I would express my deepest gratitude to my Ph.D. advisor, Professor Kelvin Y. Xie, who always supports me no matter what happens. It's my great pleasure to work with him and my great honor to be his first graduate student. I learned a lot during this four-year journey with him, from the fundamental theory to the basic operation to the complex material systems, from how to become a good researcher to how to become a decent person. With his support, I have the chance to attend various conferences and travel across the United States, from the east coast of Boston to the west coast of San Diego, from Harvard to MIT to Yale. Dr. Kelvin is not only a good teacher for me but also a good friend to me. As an international student who stays in the U.S., Dr. Kelvin makes me feel our group likes home. I still remember the whole story with Dr. Kelvin starts from a "random" message exchange during the class to a "random" interview via Skype, and finally, it becomes the most significant and unforgettable memory in my life. I believe this is fate and destiny, and this is my fortune.

I would like to thank all my friends and colleagues in Dr. Kelvin's group. The first and the most important person that comes to my mind is Dr. Xiaolong Ma, who joined our group at the beginning of my second year. Although he only stayed in our group for one year, I learned so many things from Dr. Ma and with his proper guide, I published my first paper in 2020. He is a role model for me as a great researcher. Thank Dr. Sisi Xiang, our group's first postdoc and pioneer, and Hsuming Lien, our group's first master student. We spent a lot of time together during the first two years. Thank Digvijay Yadav, Griffin Turner and Jiaqi Dong, three following graduate students from 2019 to 2020. Our group can not be such productive without their support. Thank my undergraduate

students from the Department of Computer Science, Aniket Patel and Aaron Barbosa. We worked together during the last two years and finally a paper is coming. Thank my undergraduate student from our department, Peter Evans, Zachary Theimer and Nicholas Williams, who worked in the ARL lab with me during the last two years. I appreciate these two valuable experiences as a mentor to guide all these undergraduate students, and I will never forget their enthusiastic attitude toward the future.

I also want to thank all my friends at Texas A&M University. My special thanks go to Dandan Tu, who accompanied me for countless days and nights. We drove to all the major cities within Texas and traveled together across the U.S. Thank Zeyi Tan, my old friend back in 2011 in HIT. He helped me a lot when I applied for Texas A&M University and introduced most of my following friends here. Thank Qing Zhou, my first roommate in the U.S., who supported me during the transition stage, including teaching me how to drive. Thank Yuwei Zhang, Baiyu Zhang, Zhiqiang Zhan, Lai Jiang and Xinzhu Zheng. So many PUBG games, BBQ, and hot pot events with you makes my Ph.D. life more colorful.

I want to say thanks to all my friends outside Texas A&M University. Thank Zhenhan Huang, my best friend back to HIT as an undergraduate student. We traveled together, from Texas to the east coast. Thank Xingyao Gao, who is extremely helpful during my graduate school application and recent job finding. I missed the camping, kayak and BBQ in Lake Somerville with you, Zeyi Tan on the 2018 Spring break.

I also want to acknowledge all professors and staff in the Department of Materials Science and Engineering. The valuable knowledge and various activities provided by my department make my time at Texas A&M University a great experience. Thank my committee members, Dr. Karaman, Dr. Demkowicz, and Dr. Sagapuram, for their guidance and support throughout this research. At the same time, I deeply appreciate all the services and education from Texas A&M University, including ISS, Rec, Evans Library, Health Center, Microscopy Center, Career Center, etc. I'm so proud to be an Aggie.

Finally, thank my father, Weiru Zhao and my mother, Shuzhi Xu, for their "virtual" accompany

during my entire Ph.D. Both of them are incredibly supportive of my career path. I still remember the moment my father and I went to Beijing together to collect information about study abroad back in 2015. I Sill remember the moment I said goodbye to them in the airport back in 2017. I feel so sorry for this four-year absence from their daily life. I am deeply appreciative of all that you have sacrificed for me.

I cherish this beautiful journey with all of you. My best wish and hope will be here, along with this dissertation, forever.

CONTRIBUTORS AND FUNDING SOURCES

Contributors

This work was supported by a dissertation committee consisting of Professor Kelvin Xie (advisor), Professor Ibrahim Karaman (member) and Professor Michael Demkowicz (member) of the Department of Materials Science and Engineering and Professor Dinakar Sagapuram (member), jointly appointed in the Department of Industrial and Systems Engineering and the Department of Materials Science and Engineering.

The compression and tension tests in this dissertation were conducted by Professor Ibrahim Karaman's group in the Department of Materials Science and Engineering at Texas A&M University. The magnesium rare earth alloy in Chapter 5 was provided by Professor Alan Luo's group in the Department of Materials Science and Engineering at Ohio State University.

All other work conducted for the dissertation was completed by the student independently.

Funding Sources

The graduate student was supported by Texas A&M University President's Excellence Fund X-Grants Program and National Science Foundation (NSF-DMR) under Grant Number 1709865. The graduate student was also supported by funding from the Department of Materials Science and Engineering at Texas A&M University and Texas A&M Engineering Experiment Station (TEES).

NOMENCLATURE

Mg	Magnesium
RE	Rare Earth
Mg-3Al-1Zn	AZ31
HCP	Hexagonal Close Packed
TEM	Transmission Electron Microscopy
SEM	Scanning Electron Microscopy
EBSD	Electron Backscattered Diffraction
BF	Bright Field
WBDF	Weak Beam Dark Field
PED	Precession Electron Diffraction
PFs	Pole Figures
IPF	Inverse Pole Figure
MUD	Multiple of Uniform Density
CRSS	Critical Resolved Shear Stress
SFs	Schmid Factors
ND	Normal Direction
RD	Rolling Direction
TTs	Tension Twins

TABLE OF CONTENTS

Page

LIST OF FIGURES

FIGURE Page

LIST OF TABLES

TABLE Page

1. INTRODUCTION

1.1 Background and Motivation

Magnesium (Mg) is the lightest structural metal with a density of only 1.74 g/cm^3, which is 23% that of steel (8.05 g/cm^3) and 66% that of aluminum (Al, 2.71 g/cm^3). It is also a widely available metal which is the eighth-most abundant element in the earth's crust and the third most plentiful element dissolved in the seawater. These unique properties make Mg a promising candidate to substitute steel and aluminum alloy in the transportation and automobile industry to overcome energy crises and carbon-neutral challenges. The usage of Mg for structural material purposes can be traced back to German military aircraft during World War I and II. In the 21st century, driven by lightweighting and energy saving, the application of Mg alloy receives unprecedented research and industrial interest. For example, in the automobile industry, the Renault EOLAB hybrid car (Figure 1.1a), made from Mg alloys, was able to run 100 kilometers on a liter of gas, which is only a quarter of gas consumption compared with the regular sedan vehicles [1, 15]. Moreover, in the electronic industry, Microsoft launched a new Surface series (Figure 1.1b) using Mg alloy as bodies and frames, which replace traditional aluminum alloy [2].

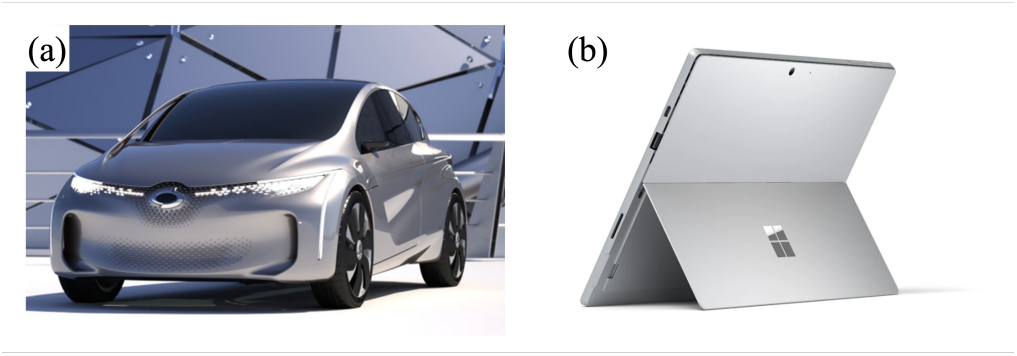

Figure 1.1: (a) Renault EOLAB hybrid car made from Mg. (b) Microsoft's Surface series with Mg alloy bodies and frames. Images adapted from ref [1, 2].

The usage of Mg for structural applications is much less than those of steels and aluminum alloys. The most significant barrier to the wider applications of Mg as a structural material is its poor ductility and formability at room temperature. The pure Mg is brittle and fractures only at $\sim$10% single-pass thickness reduction during the cold rolling. This is in strong contrast to pure Al, which can be easily cold rolled till 90% reduction [16]. Although hot rolling can increase the formability of Mg, there is an increase in energy consumption. Moreover, hot rolling develops a strong basal texture in Mg, which makes further deformation and forming difficult [5].

1.1.1 Deformation Mechanisms

To achieve improved formability and ductility, a comprehensive understanding of the fundamental deformation behavior in Mg and Mg alloys is critical. Mg has a hexagonal closed-packed (HCP) crystal structure with the c/a ratio of 1.623, slightly lower than the ideal c/a ratio for HCP (1.633). There are mainly three types of slip systems (basal $< a >$ slip, non-basal $< a >$ slip, and pyramidal $< c + a >$ slip) and two types of twinning modes (extension twinning and contraction twinning), as shown in Figure 1.2.

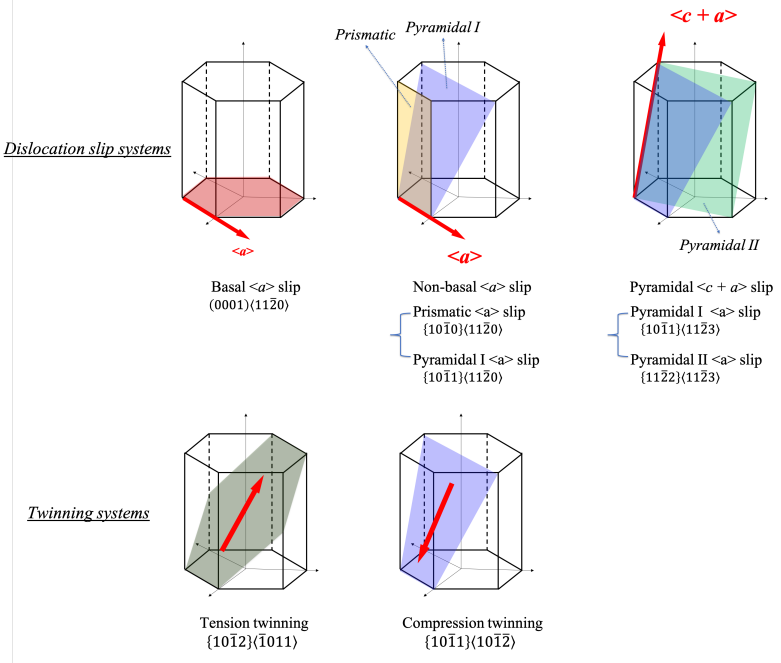

Figure 1.2: The major deformation mechanisms in HCP Mg.

Of the multiple possible dislocation slip systems in Mg (Figure 1.2), the basal $< a >$ slip (burgers vector $\mathbf{b} = \frac{1}{3} < 11\bar{2}0 >$) is the easiest and most ubiquitous slip, which has a critical resolved shear stress (CRSS) of only ∼0.5 MPa [17]. However, the basal $< a >$ slip cannot accommodate the strain along the c-axis and can only provide two independent slip systems. To satisfy the Von Mises criteria of five independent slip systems for polycrystalline material arbitrary shape change [18], extra three independent deformation mechanisms are required.

Non-basal $< a >$ dislocation, which slips on the prismatic and pyramidal I planes, can provide extra slip modes. Non-basal $< a >$ slip is considered as the dominated deformation mode in Mg single crystal during tension along the basal plane [19]. However, non-basal $< a >$ dislocations are much more difficult to activate than the basal $< a >$ dislocations due to their much higher CRSS, which is in the range of 30-50 MPa [20, 21].

Although the non-basal $< a >$ slip can provide extra deformation modes, the c-axis strain cannot be accommodated with $< a >$ type dislocation. The pyramidal $< c + a >$ dislocation, which has a burgers vector $\mathbf{b} = \frac{1}{3} < 11\bar{2}3 >$, can accommodate c-axis compression. The CRSS of the $< c + a >$ dislocation is even higher than the non-basal $< a >$ dislocation and is roughly 100 times that of the basal $< a >$ dislocation [7]. The $\{10\bar{1}0\} < 11\bar{2}3 >$ pyramidal I and $\{112\bar{2}\} < 11\bar{2}3 >$ pyramidal II $< c + a >$ slip systems can be activated under c-axis compression on Mg single crystal when the zero or low Schmid factor on the basal plane prohibits the easy basal glide [22, 7, 9, 23, 24, 25].

In addition to the pyramidal $< c + a >$ slip, deformation twinning can also accommodate the c-axis strain. Among the multiply twinning systems, the $\{10\bar{1}2\} < \bar{1}011 >$ extension twinning, which rotates the crystal by 86°, is the most frequently observed and reported twinning system [12, 14]. For Mg single crystals, the extension twins can be activated when the samples are pulled parallel to the c-axis or compressed perpendicular to the c-axis (c-axis tension). In contrast to the extension twinning, the contraction twins, which rotates the crystal by 56°, can be activated under c-axis compression but are much harder to form due to much higher CRSS [12, 14, 13].

1.1.2 Plastic Anisotropy

Due to the low-symmetry nature of the HCP crystal structure in Mg, the plastic anisotropy is large. During the rolling process, there is much larger deformation resistance perpendicular to the basal plane direction (compression) than parallel to the basal plane direction (Figure 1.3a). Under this circumstance, a strong basal texture is easily formed after rolling with the c-axis aligned perpendicular to the rolled surface (Figure 1.3b). An example of the electron backscattered diffraction (EBSD) orientation map from the pure Mg normal plane is shown in Figure 1.4. The inverse pole figure (IPF) map, (0001) pole figure, and the schematic illustrate a strong basal texture, which has most of grains' c-axis close to the normal direction.

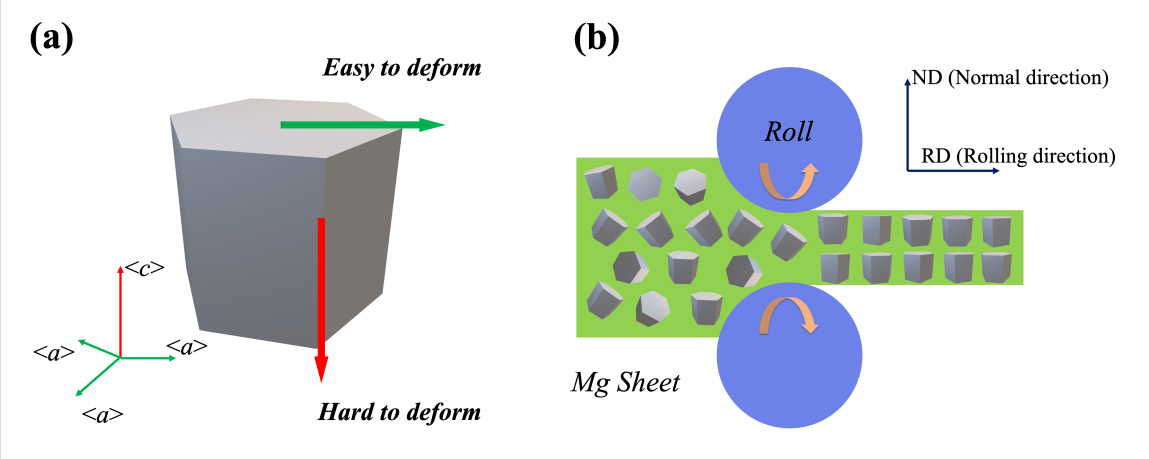

Figure 1.3: During rolling process at room temperature, (a) strong anisotropy of Mg HCP and (b) strong basal texture formed.

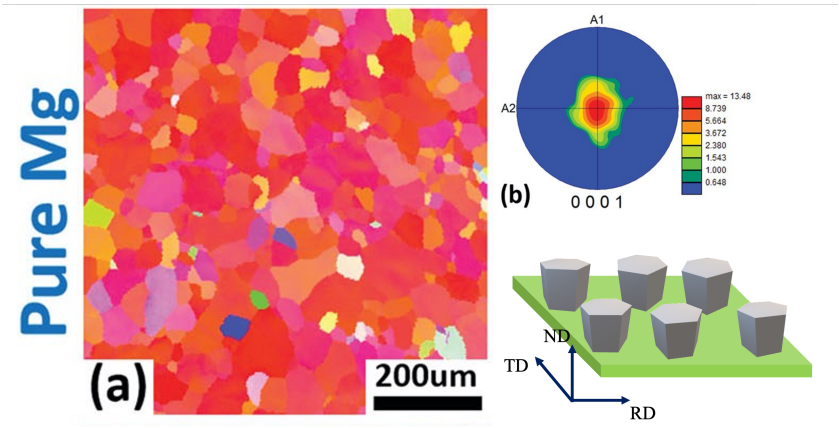

Figure 1.4: EBSD IPF maps (out-of-plane crystal orientation) of pure Mg plate normal plane, along with the corresponding (0001) pole figure indicating the strong basal texture. Image adapted from Ref [3].

Furthermore, the strong plastic anisotropy will influence the deformation of the highly-textured Mg. As shown in Figure 1.5, the apparent different stress-strain curves from compression and tension along different directions indicate such an anisotropy. The CA0ND0 compression test (red dashed curve) is close to the c-axis direction, and $< c + a >$ slip system is considered as the dominant slip system. The high work hardening is associated with the exhaustion of mobile $< c + a >$ dislocations [7, 10]. In contrast, CA0ED0 compression (a-axis compression, blue dashed line) introduces extension twinning instead of the $< c + a >$ dislocations. The sigmoidal-shaped stress-strain curve indicates the low CRSS and extension twinning. For the tension tests, TA90ND0 tension (black curve) activates the non-basal $< a >$ dislocation (prismatic $< a >$ dominated), which also has a relatively large strain hardening rate than extension twinning.

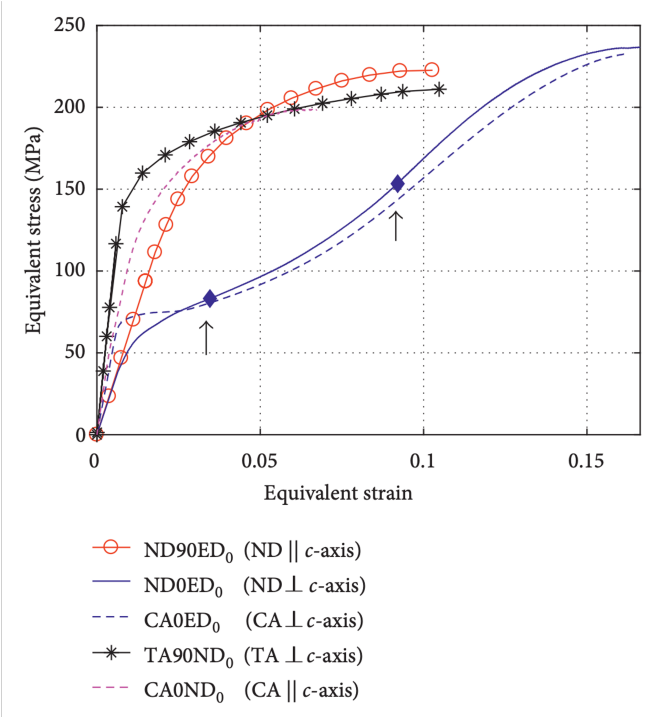

Figure 1.5: Stress-strain curves of pure Mg at room temperature under different mechanical tests including plane strain compression (ND90ED0 and ND0ED0), simple compression (CA0ED0 and CA0ND0), and uniaxial tensile (TA90ND0). Image adapted from Ref [4].

1.1.3 Mg Alloys

Driven by the design of more ductile Mg alloys, Mg alloying has attracted extensive research interest during the past decade [26, 27, 5, 28, 8, 29, 30, 31]. Depending on whether rare earth (RE) element is used, Mg alloys can be divided into non-rare earth (non-RE) Mg alloys and RE (e.g., Y, Gd, Ce, Er and Nd) Mg alloys. The primary commercial alloys for non-RE Mg alloys are the AZ/AZM series (Mg-Al-Zn-Mn) and ZK series (Mg-Zn-Zr), with the most famous one as AZ31. AZ31 attracts the most attention and exhibits a much better ductility than pure Mg[8]. For the Mg RE alloys, the currently used commercial ones are the AE series (Mg-Al-RE), EZ series (Mg-RE-Zn) and WE series (Mg-RE-Zr).

The improved ductility from Mg alloying can be explained by easing certain deformation modes and weakening texture. As shown in Figure 1.6, Sandlobe *et al.* demonstrated the im-

proved ductility of Mg-Al-Ca alloy is from the more active $< c + a >$ dislocations, which can accommodate larger c-axis strain than pure Mg to avoid early-stage fracture. The alloying elements could modify the non-basal slip systems activities and reduce the strong anisotropy in wrought Mg. [27, 8, 32, 33, 34, 35]. Additionally, texture weakening (mainly by RE and Ca elements) can also reduce the strong anisotropy in wrought Mg. As shown in Figure 1.7, with the addition of Ca and Ce, more random texture and spread pole were achieved comparing with pure Mg (Figure 1.4). Thus, more uniform deformation can be introduced.

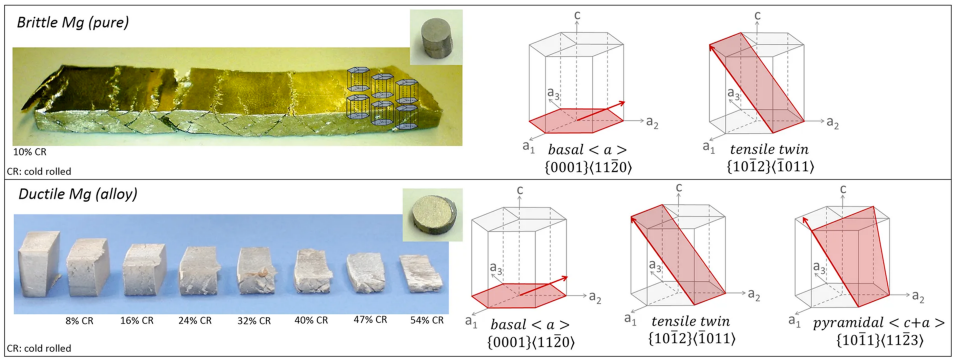

Sandlöbes *et al.* Scientific Reports (2017)

Figure 1.6: Mg-Al-Ca alloy exhibits much improved ductility than pure Mg at room temperature due to the enhanced $< c + a >$ dislocation activity to accommodate the c-axis strain. Image adapted from Ref [5].

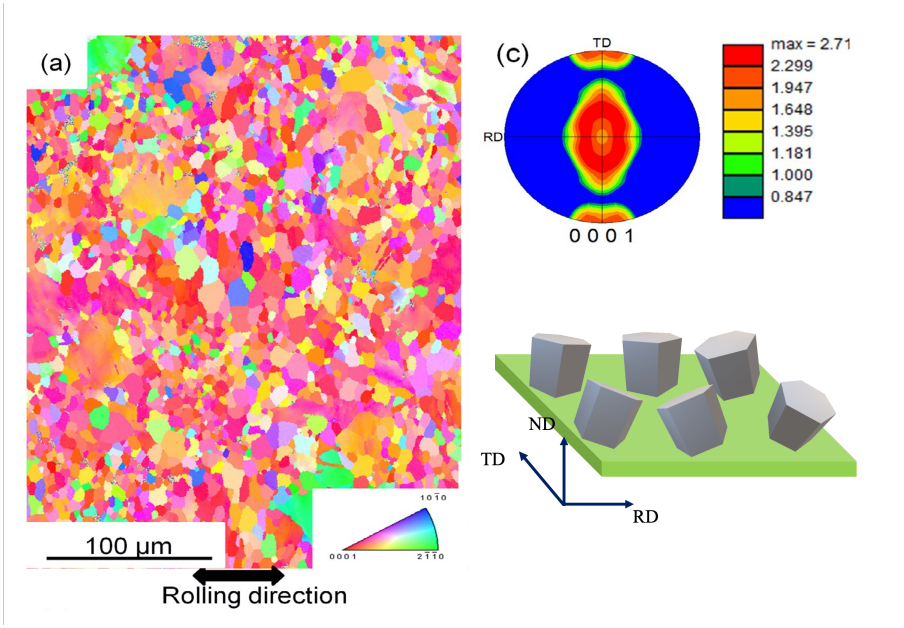

Figure 1.7: EBSD IPF maps (out-of-plane crystal orientation) of Mg–Zn-Ca-Ce alloy plate normal plane, along with the corresponding (0001) pole figure indicating the much weaker basal texture than the pure Mg. Image adapted from Ref [6].

1.1.4 Microscopy Characterizations of Dislocations and Twins in Mg

With the help of advanced characterization techniques, dislocation and twinning microstructure in Mg can be resolved and correlated with the mechanical properties.

Transmission electron microscopy (TEM) is the main tool to study dislocations in Mg (and in any other materials). The samples are usually thinned down to $\sim$100 nm to achieve electron transparency. The micrographs are then formed from the 2D projections of the 3D line features. Obara *et al.* pioneered using TEM to study dislocations in Mg back to 1973. The author performed two-beam condition TEM imaging on the c-axis compressed Mg single crystals and revealed the presence of $< c + a >$ dislocations, describing them as "long and straight" lying parallel in the basal plane (Figure 1.8a) [7]. $< c + a >$ dislocations were confirmed as the dominant deformation mode to accommodate Mg single crystal c-axis or wrought Mg polycrystal normal-direction compression. In contrast, non-basal $< a >$ slip is considered as the dominant deformation mode to accommodate rolling-direction tension with $< c + a >$ activated, as demonstrate by Agnew *et al.*

in AZ31 alloy (Figure 1.8b) [8]. However, the $< c+a >$ dislocation "basal-bound" puzzle was not solved until 2015. Geng *et al.* performed high angle annular dark-field scanning TEM (HADDF-STEM) imaging on the dislocation core and observed the $< c+a >$ dislocations dissociate into two edge partials with a stacking fault in between [9] (Figure 1.8c). In the same year, Wu and Curtin explained experimental observed $< c + a >$ dislocation dissociation using molecular dynamics simulation (Figure 1.8c) [10]. The $< c + a >$ dislocation dissociation process can be written as $\frac{1}{3} < 11\bar{2}3 > \rightarrow \frac{1}{6} < 20\bar{2}3 > + SF_{(0001)} + \frac{1}{6} < 02\bar{2}3 >$. More recently, Xie *et al.* conducted careful tilting experiments and observed the majority of $< c + a >$ dislocations dissociated into curved partial dislocations on the basal plane instead of straight partial dislocations(Figure 1.8d) [11]. Note that the slip planes for $< c+a >$ dislocations are pyramidal, not basal. Therefore, these basal-bound $< c + a >$ dislocations are sessile and cannot provide sustainable strain hardening, which leads to a high hardening and a low strain to failure.

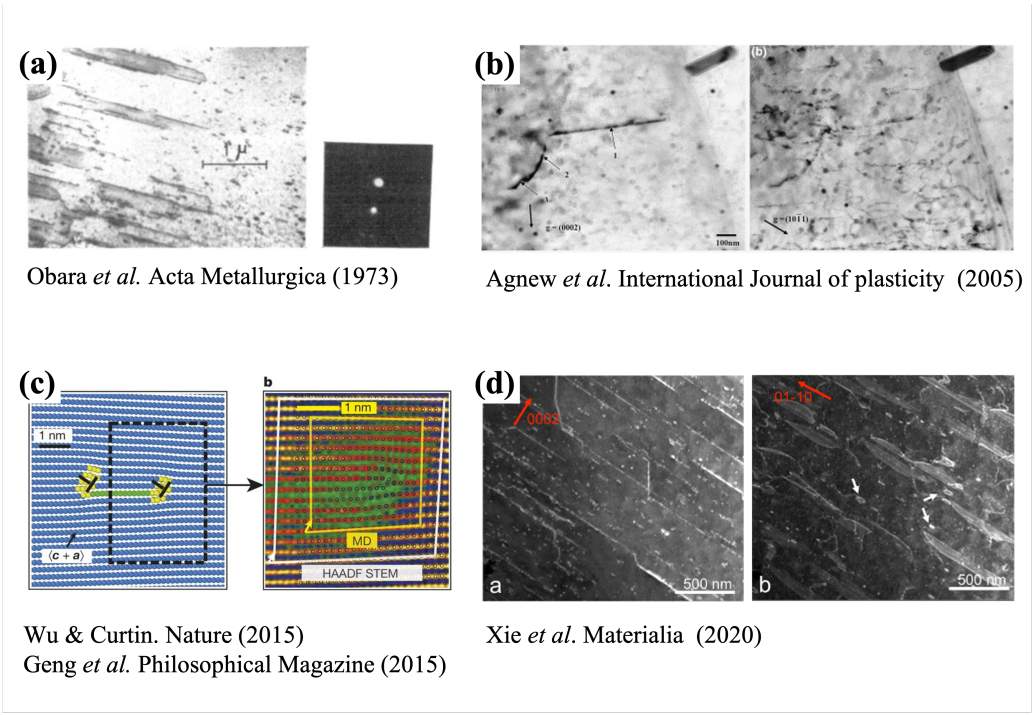

Obara *et al.* Acta Metallurgica (1973)

Agnew *et al.* International Journal of plasticity (2005)

Wu & Curtin. Nature (2015)
Geng *et al.* Philosophical Magazine (2015)

Xie *et al.* Materialia (2020)

Figure 1.8: Selected TEM characterization work Mg dislocations. Image adapted from Ref [7, 8, 9, 10, 11].

To study Mg extension twinning and contraction twinning, scanning electron microscopy (SEM) equipped with the electron backscattered diffraction (EBSD) capability was adapted by Barnett *et al.* back in 2007 (Figure 1.8a-b) [12]. Inverse pole figure maps were acquired to reveal the crystal orientation before and after extension twinning, contraction twinning, and double twinning (Figure 1.8a-b). Moreover, in 2010, Hong *et al.* discovered the extension twin variants were dependent on strain path based on the EBSD results [13]. Although both normal-direction tension and rolling-direction compression can activate extension twinning, more twin variants were observed in the normal-direction tension samples than the rolling-direction compression samples due to the Schmid factor effect (Figure 1.8c). In the same year, Beyerlein *et al.* also reported the Schmid factor effect in extension twinning and concluded Schmid factor of individual grain greatly influences the propensity for twinning in the grain, where a higher value of the Schmid factor leads to a larger area fraction, a larger number, and thicker twins (Figure 1.8d) [14].

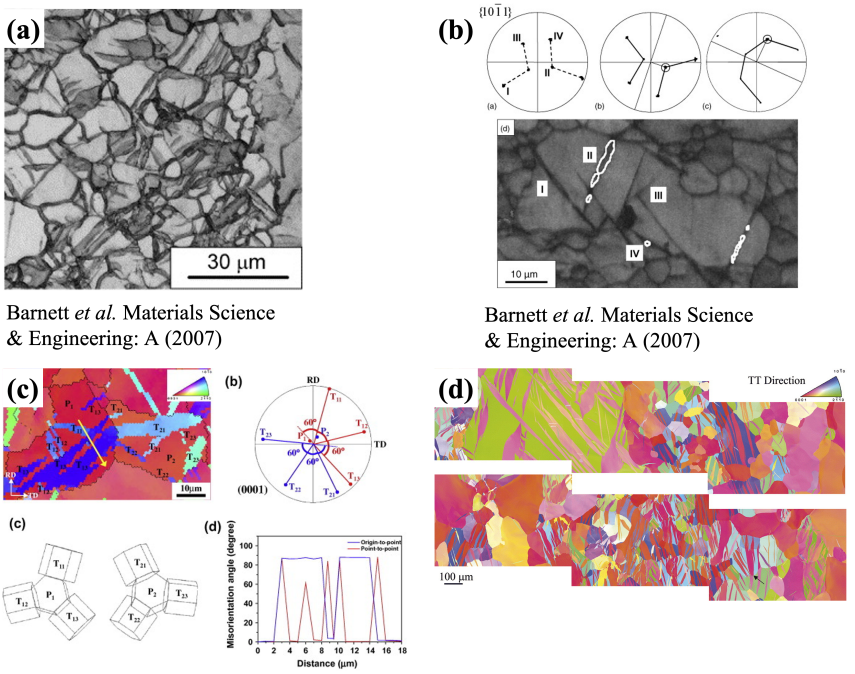

Figure 1.9: Selected EBSD characterization of Mg extension twins. Image adapted from Ref [12, 13, 14].

1.2 Motivation and Thesis Objectives

As discussed in the 1.1.4, most of the studies of the activation of $< c + a >$ dislocation focus on Mg single crystals. For Mg polycrystal, due to different grains' orientations and grain boundary effect, the activation of $< c + a >$ dislocation could be more complex. In this case, whether the activation of $< c+a >$ is determined by the orientation of the individual grain or the global texture of the polycrystal is unclear. The first scientific question we ask is how the polycrystalline nature of the material affects the activation of $< c + a >$ dislocation (Chapter 2).

Followed by the studies of the activation of $< c + a >$ in polycrystal Mg, the next intuitive scientific question is how the polycrystalline nature of material affects the activation of $\{10\bar{1}2\} < \bar{1}011 >$ tension twinning. In 1.1.4, it has been reported that twins are more easily activated in those grains orientated favoring twinning. However, most previous investigations focus on the loading conditions where twinning is favored. It is important to point out that even when the loading conditions do not generally favor twin formation, some twins could be observed locally. Thus, the second scientific question to ask is what is the effect of the individual grains' orientation on their twinning behavior when the loading condition does not apparently favor twinning (Chapter 3).

Mg AZ31 alloy and Mg–2Zn-0.3Ca-0.2Ce-0.1Mn exhibit approximately 3 times and 6 times better ductility than pure Mg, respectively. Yet, there lacks the understanding of the fundamental mechanisms that govern the improved ductility. Where is the enhanced ductility from? How non-RE alloying (e.g., Al and Zn) affects the $< c + a >$ dislocation and extension twinning activities? How RE alloying (e.g., Ce) affects the $< c + a >$ dislocation and extension twinning activities? Those scientific questions will be addressed in Chapter 4 and 5.

The primary objective of the project is to study the activation and suppression of non-basal slips (non-basal $< a >$ and $< c+a >$) and $\{10\bar{1}2\} < \bar{1}011 >$ extension twinning in deformed pure Mg and Mg alloys by advanced electron characterization techniques (SEM, TEM, etc.). The long-term goal is to utilize the uncovered fundamental mechanisms gained from the above observations to guide the design of new generation Mg alloys that exhibit a combination of excellent strength and ductility. The implementation of the discoveries would enable lightweighting and reduce energy

consumption. There are five parts in this dissertation:

Chapter 1 provides: 1) Background of Mg and Mg alloy, including the current application and potential challenges; 2) Mg major deformation mechanisms, unusual rolling texture, associated plastic anisotropy and Mg alloying; 3) Milestones of the Mg dislocation and twinning characterization.

Chapters 2 and 3 focus on understanding the Schmid factor effect on $< c + a >$ dislocation and $\{10\bar{1}2\} < \bar{1}011 >$ extension twinning activation and suppression. Textured AZ31 alloy was selected as the model material. In chapter 2, $< c + a >$ dislocation activation and suppression was studied on the normal-direction and 45° compressed AZ31. Statistical analyses from the correlative microscopy results (EBSD and TEM) revealed that the activation and suppression of $< c + a >$ dislocations in polycrystalline Mg are primarily governed by the overall texture, regardless of the crystallographic orientation of each grain. This observation is explained by the requirement of five independent slip systems, reduced anisotropy, and twin-induced strain localization. In chapter 3, $\{10\bar{1}2\} < \bar{1}011 >$ extension twinning was studied on the deformed Mg under multiple deformation conditions (normal-direction compression and tension, rolling-direction compression and tension, and 45° compression). Statistical analyses from the EBSD results revealed extension twinning generally obeys the Schmid law for individual grains, regardless of whether the global stress state favors extension twinning or not. The strong dependence of extension twinning on the Schmid factor is in contrast to the weak correlation of $< c + a >$ dislocations.

Chapter 4 investigates the effect of non-RE alloying on the activation and suppression of $< c + a >$ dislocation and extension twinning. Moreover, the operation of specific deformation mode on the sample ductility was discussed. Non-RE Mg (pure Mg and AZ31) with similar initial microstructures (i.e., grain size and texture) were chosen as model materials. Systematic tilting experiments and statistical analyses were performed on both pure Mg and AZ31 after rolling-direction tension at different strain levels. The observations revealed a significant disparity of non-basal dislocation activities between pure Mg and AZ31. For pure Mg, $< c + a >$ dislocations were activated since the early stage of plastic deformation. The $< c + a >$ dislocations display

a much shorter dissociation distance under tension as compared to the ones reported from c-axis compression. Increasing strain level appears to promote the cross slip of $< c + a >$ dislocations. For AZ31, $< c+a >$ dislocations were largely absent at all strain levels, even in the strain-to-failure samples. Non-basal $< a >$ dislocations, including prismatic and pyramidal $< a >$ dislocations, were observed. The promotion of the non-basal $< a >$ dislocation activities and the suppression of $< c + a >$ dislocations in AZ31 are expected to offer more sustainable hardening, which could elucidate the absence of apparent shear banding and much-improved ductility in AZ31 compared to pure Mg.

Chapter 5 extends the idea of chapter 4 and focuses on the effect of RE alloying on the activation and suppression of $< c + a >$ dislocation and extension twinning. Meanwhile, the influence on sample ductility was also discussed. The microstructure of a newly developed Mg RE alloy (Mg–2Zn-0.3Ca-0.2Ce-0.1Mn) with an exceptionally high tensile ductility was characterized by SEM and TEM at selected strain levels. Compared with the pure Mg and AZ31 microstructure at the same deformation conditions (chapter 4), our results revealed that the high ductility of ZXEM2000 could be attributed to four key factors: weaker texture, finer grain size, reduced twinning, and increased cross-slip frequency of $< c + a >$ dislocation.

Chapter 6 provides a summary of the key findings and suggests future work.

2. ACTIVATION AND SUPPRESSION OF <C + A> DISLOCATIONS IN A TEXTURED MG-3AL-1ZN ALLOY[1]

2.1 Introduction

Magnesium (Mg) and its alloys have attracted extensive research interests as they are promising lightweight and high specific strength structural materials. However, pure Mg and most Mg alloys are brittle and difficult to form at room temperature [8, 36]. The limited ductility and formability are attributed to the low mobility of pyramidal $< c+a >$ dislocations, which usually accommodate c-axis compression [22, 21, 26, 37, 38, 10, 39, 27]. Thus, the detailed understanding of $< c+a >$ dislocation behavior could potentially guide the design of ductile and formable Mg alloys.

The activation of pyramidal slip has been well studied in Mg single crystals [22, 7, 23, 9, 25, 40, 41]. When compressed along the c-axis, $< c+a >$ dislocations were observed to be the dominant deformation mechanism. Obara *et al.* [7] performed detailed two-beam condition analyses using transmission electron microscopy (TEM) and concluded that the Burgers vector of $< c+a >$ dislocations is $< 11\bar{2}3 >$ [7]. Recent experimental studies [22, 42] and molecular dynamics simulations [43] demonstrated that $< c+a >$ dislocations can glide on both $\{10\bar{1}1\}$ pyramidal I and $\{11\bar{2}2\}$ pyramidal II planes. The critical resolved shear stress (CRSS) of $< c+a >$ pyramidal slip measured ∼40 MPa [7], which is much higher than that of basal slip (0.5 MPa, with the Burgers vector $< 11\bar{2}0 >$) [21, 17]. Due to this substantial anisotropy, if the c-axis is a few degrees off the loading direction in Mg single crystals, according to Schmid's law, basal $< a >$ slip will be activated to accommodate the plastic deformation. As a result, $< c+a >$ slip will be suppressed.

The $< c+a >$ dislocation activities in polycrystalline Mg samples are more complex than in single crystals [29]. When compressing a hot-rolled Mg plate along the normal direction, although many grains have their c-axis aligned close to the loading direction, the activation of $< c+a >$

[1]Reprinted with permission from "Activation and suppression of< c+ a> dislocations in a textured Mg–3Al–1Zn alloy" by Dexin Zhao, Xiaolong Ma, Sezer Picak, Ibrahim Karaman, Kelvin Xie. Scripta Materialia, vol. 179, pp.49-54. Copyright (2020).

dislocations could depend on two factors: 1) the orientation of the individual grain and 2) the global texture of the bulk material. For a grain whose c-axis is aligned away from the loading direction, the Schmid factor analysis predicts no or very few $< c + a >$ dislocations in such grain, as the basal slip would be the dominant deformation mechanism. On the other hand, the deformation of such grain may also be constrained by the highly textured neighboring grains to satisfy strain compatibility, leading to profuse $< c + a >$ dislocation activities. The scientific question we aim to answer is which of the two aforementioned factors - the individual grain orientation or the global texture - is more dominant for $< c + a >$ dislocation activation. In this work, we selected a highly textured hot-rolled Mg-3Al-1Zn (AZ31) as the model material and developed a correlative microscopy technique to link the crystal orientation with the $< c + a >$ dislocation microstructure to address the above question.

2.2 Materials and Methods

A hot-rolled AZ31 sheet was purchased from MetalMart International Inc. The bulk sample was annealed at 350 °C for 12 h with Ar flow to remove the stored dislocations. Rectangular compression specimens (4 mm × 4 mm × 8 mm) were electrical discharge machined (EDM) from the center of the hot-rolled plate. Quasi-static compression tests were conducted along the normal direction (ND) and 45° off-normal direction (refer to 45°) at a strain rate of 5×10^{-4} s^{-1}. The representative stress-strain curves were obtained from two specimens compressed to failure. All presented microscopy studies were performed on the specimens compressed to $\sim$2.6% plastic strain.

Correlative microscopy specimens were cut from the center region of the compression samples. To measure the off-angle between the c-axis of the grains of interest and the loading axis, non-circular TEM foils with one straight edge parallel to loading direction were fabricated. These discs were then twin-jet electropolished using a Tenupol-5 polishing system with a solution of 15.9 g lithium chloride, 33.5 g magnesium perchlorate, 1500 ml methanol and 300 ml 2-butoxy-ethanol at -40 °C. Electron backscattered diffraction (EBSD) was carried out on TEM foils after ion mill at liquid nitrogen temperature using a Tescan FERA scanning electron microscope equipped with

an EBSD detector from Oxford Instrument. Dislocations were imaged using the 2-beam bright-field (BF) and weak beam dark-field (WBDF) techniques on an FEI Tecnai TEM operating at 200 keV. To reveal the dislocation characters, we performed careful tilting experiments in TEM and used $\mathbf{g} \cdot \mathbf{b} = 0$ invisibility criteria to separately illuminate $< a >$ and $< c >$ components. The **g**-vectors we used to illuminate dislocations are $\mathbf{g} = [0002]$ (all c-component will be visible) and $\mathbf{g} = [01\bar{1}0]$ (two-thirds of a-component will be visible). If a dislocation is visible under both $\mathbf{g} = [0002]$ and $\mathbf{g} = [01\bar{1}0]$ conditions, it is of $< c + a >$ type. We randomly selected 19 grains for ND compression samples and 12 grains for 45° compression samples to study the dislocation activities statistically, from which 5 and 6 representative grains were used to elucidate the general observations separately.

2.3 Experimental Results

The mechanical properties of the hot-rolled AZ31 in this study are consistent with what has been reported in the literature [44, 45]. As shown in Figure 2.1a, the ND compression stress-strain curve does not show a sharp yielding transition. The yield strength, ultimate compressive strength and strain to failure were measured to be 107 ± 4 MPa, 296 ± 18 MPa, and $9.9\% \pm 0.8\%$, respectively. The 45° compression sample curve shows a clear yield transition. The yield strength, ultimate compressive strength, and strain to failure were measured to be 71 ± 1.4 MPa, 355 ± 2.5 MPa, and $16.5\% \pm 0.5\%$, respectively. The global EBSD inverse pole figure (IPF) of the as-hot-rolled sample confirmed the strong c-axis texture along the ND (Figure 2.2a). The average grain size measured is approximately 10 μm. For the ND samples, the c-axis texture did not change significantly after compression (an example see Figure 2.2b). This was expected, as dislocation-mediated plasticity is the predominant deformation mode. Very few $\{10\bar{1}2\}$ twins were noted but they are not a prominent microstructural feature. For 45° compression samples, high-density $\{10\bar{1}2\}$ extension twins (an example see Figure 2.2c) were observed.

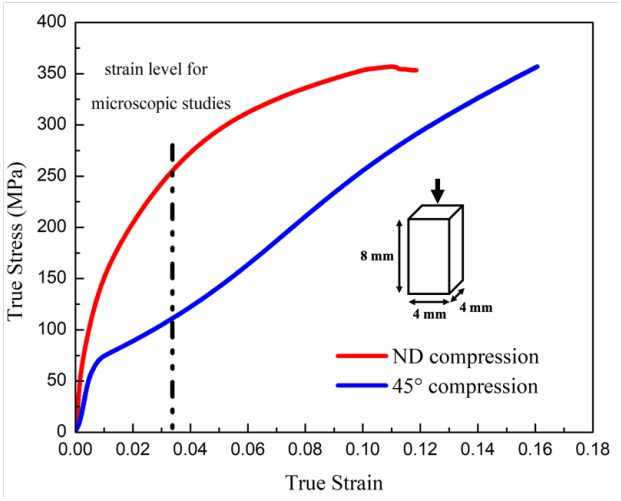

Figure 2.1: Stress-strain curves of polycrystal hot-rolled Mg AZ31 alloy (after heat treatment) under compression along normal direction (ND compression, close to c-axis) and 45° off normal direction (45° compression).

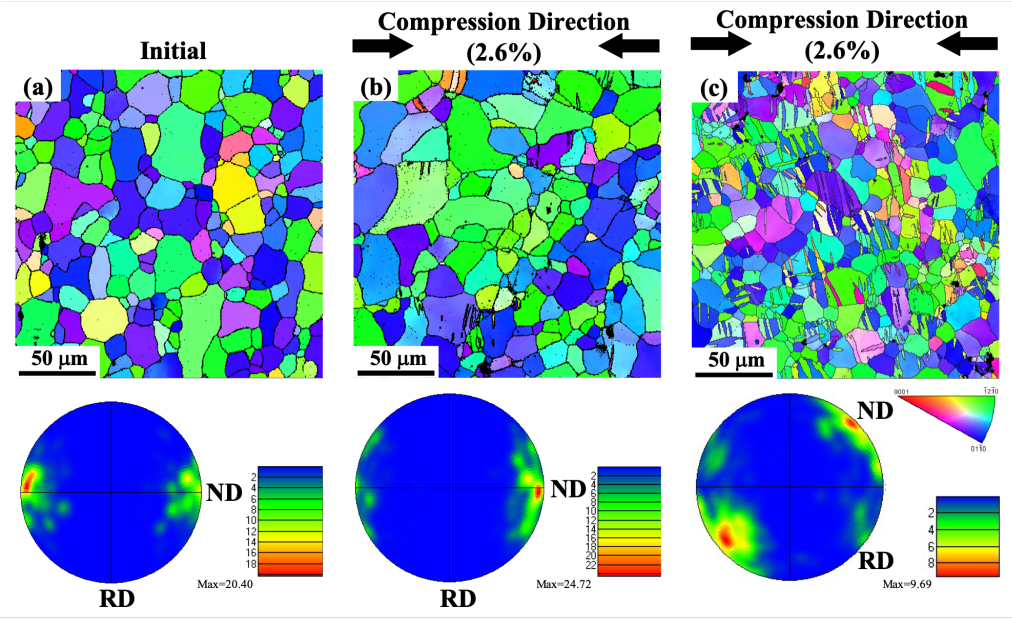

Figure 2.2: EBSD IPF maps (out-of-plane crystal orientation) of AZ31 (a) initial, (b) compression along the normal direction (2.6% plastic strain) and (c) compression along 45° off normal direction (2.6% plastic strain), along with the corresponding (0001) pole figure and their highest mud values.

To uncover the detailed deformation mechanisms of individual grains in the samples, EBSD and TEM were performed on the same set of grains to correlate the crystal orientation with the dislocation activities. The off-angles between the c-axis of each grain and the loading direction were firstly identified by EBSD, and the dislocation activities in the corresponding grains were examined afterward Figure 2.3 shows the observation from the ND-compression sample. The compression direction is marked by the black arrows above each IPF map. The dark feature in the middle of each map is the perforated hole produced by electropolishing. Adjacent to the hole is the electron transparent area for both EBSD mapping and TEM imaging. In the EBSD maps, the grains of interest are in bright colors, with the rest partly greyed out. We note that although most grains have their c-axis off the compression direction. There are a significant number of grains off by larger angles (some even off by more than 20°). The orientations of the inspected grains are indicated by the crystal schematics in Figure 2.3a and 2.3b, which are listed in Table 2.1. Thus, despite the overall strong texture, there exist many individual grains exhibiting non-negligible off-angles.

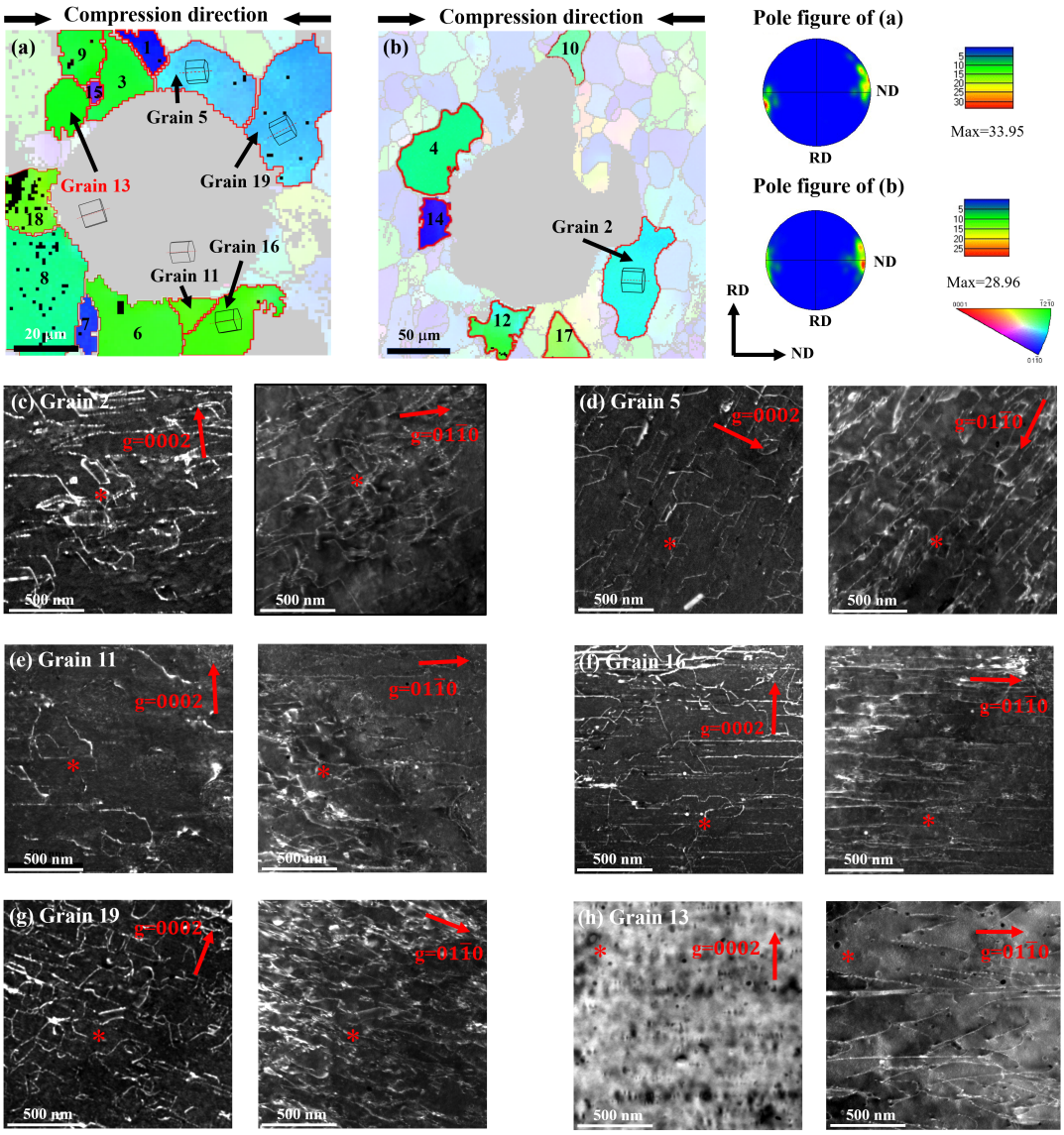

Figure 2.3: (a) and (b) IPF maps of two specially designed TEM foils near the electropolished perforation region from the ND compression 2.6%-deformed AZ31 alloy. The schematic shows the orientations of labeled grains. The black arrows above each figure indicate the compression direction. (c)-(g) Examples of WBDF micrographs in 5 grains reveal their dislocation characters. The grain labels correspond to their locations in the foil in (a) and (b). Red circles are the fiducial markers to mark the identical sites. (h) BF and WBDF micrographs of Grain 13, showing the absence of $< c + a >$ dislocations.

ND compression			**45° compression**		
Grain	**c-axis off angle**	***<c + a>***	**grain**	**c-axis off angle**	***<c + a>***
1	2.16°	yes	1	4.33°	no
2	7.35°	yes	2	6.88°	no
3	9.03°	yes	3	10.1°	no
4	10.16°	yes	4	19.16°	no
5	11.25°	yes	5	20.51°	no
6	12.00°	yes	6	21.65°	no
7	13.83°	yes	7	27.32°	no
8	14.78°	yes	8	30.86°	no
9	15.77°	yes	9	35.67°	no
10	16.90°	yes	10	40.99°	no
11	18.37°	yes	11	41.19°	no
12	18.8°	yes	12	54.34°	no
13	19.04°	no			
14	19.17°	yes			
15	19.82°	yes			
16	22.49°	yes			
17	25.38°	yes			
18	25.71°	yes			
19	28.79°	yes			

Table 2.1: The c-axis off-angle and the corresponding existence of $< c+a >$ dislocations based on TEM observations in 19 and 12 randomly selected grains from ND and 45° compression samples, respectively.

For the ND compression sample, we observed that $< c+a >$ dislocations exist in 18 grains out of 19, regardless of the magnitude of off-angle. For example, profuse $< c+a >$ dislocations were observed in Grain 1, where the off-angle is relatively small (2.16°). This observation is consistent with our expectation based on single-crystal studies [11] that $< c+a >$ dislocations are required to accommodate near-c-axis compression. However, as shown in Figure 2.3, numerous $< c+a >$ dislocations were also observed in other grains with large off-angles. An example of Grain 19 whose off-angle is up to 28.79°. The $< c+a >$ dislocations in this grain appear at least as rich as, if not more than, pure $< a >$ dislocations. This is in stark contrast to the case in single crystal studies, where no or limited $< c+a >$ dislocations should be observed when the off-angle is large [40]. The only grain that is free of $< c+a >$ dislocations in the 19 observed grains is Grain 13 with off-angle 19.04° (Figure 2.3h). The absence of $< c+a >$ dislocation is likely a stochastic outlier. We further compared the $< c+a >$ dislocations and noticed they share the same morphology and slip behavior. For example, many $< c+a >$ dislocations appear to be basal-bound when imaged with $\mathbf{g} = [0002]$, regardless of the off-angles.

For the 45° compression sample, the same methodology was adopted to characterize the crystallographic orientation and dislocation activities using both EBSD (Figure 2.4a) and TEM (Figure 2.4b). In contrast to the ND compression sample, none of those grains shows apparent $< c+a >$ dislocations (Table 2.1) and most dislocations observed only have $< a >$ character. Schmid factors of Pyramidal I, II $< c+a >$, basal $< a >$, and prismatic $< a >$ dislocations for each grain are also summarized in Appendix A Table IV-2. It is even true for the grains with small off-angles (c-axis close to the loading direction), as shown in Figure 2.3b-c. Note, individual grains with similar orientations in the ND samples contain numerous $< c+a >$ dislocations, but only $< a >$ dislocations were observed in the 45° samples. We also noticed that the $< a >$ dislocation morphology differs according to the off-angle value. For those with small off-angles, both basal and non-basal $< a >$ dislocations are activated; for those with large off-angles (c-axis far away from the loading direction), basal $< a >$ prevails.

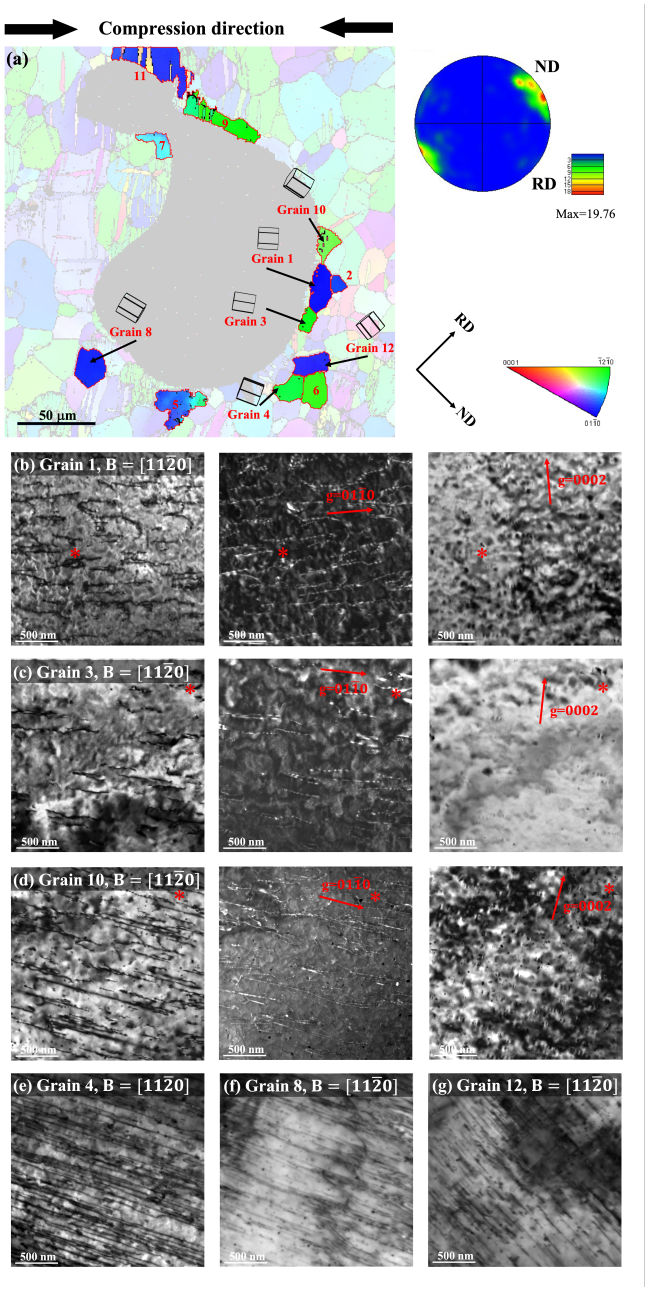

Figure 2.4: (a) IPF maps of TEM foils near the electropolished perforation region from 45° compression 2.6%-deformed AZ31 alloy. The schematic shows the orientations of labeled grains. The black arrows above the figure indicate the compression direction. 12 grains are studied in total. Six representative grains are shown. (b)-(g) Examples of BF and WBDF micrographs in 6 grains reveal their dislocation activities. The grain labels correspond to their locations in the foil in (a). Red circles are the fiducial markers to mark the identical sites.

2.4 Discussion

The activation and suppression of $< c+a >$ dislocations, supported by the statistics from both the ND and 45° samples, offer strong experimental evidence that texture plays a more dominant role than the orientation of individual grains in Mg. Even for grains with the off-angles presumably high or low enough to transit the governing dislocation mechanism, the global texture appears to inhibit such transition. We suggest that three factors contribute to this texture-governed dislocation activity.

First of all, unlike in single crystal, deformation in polycrystals requires five independent slip systems to accommodate the global strain according to von Mises condition [18]. In Mg, basal and prismatic only provide two each. Additional deformation mode, usually extension twinning or $< c+a >$ pyramidal slip, has to come into play. In the case of ND compression, given the strong texture, extension twinning is not geometrically favored for most grains. Therefore, $< c+a >$ pyramidal slip turns out to be the dominant fifth-independent slip system. In the case of 45° compression, part of extension twin variants become geometrically favored in many grains to act as the fifth deformation mode [46]. This is also evidenced by a considerable amount of extension twins in 45° compression sample (Figure 2.2c). As a result, $< c+a >$ pyramidal dislocations are inactive, as they require higher stress to multiply and glide.

Secondly, microstructural features, such as grain boundaries, dislocations, and precipitates, can reduce plastic anisotropy. In polycrystalline samples, a new term "effective CRSS" has been introduced to describe the stress values to activate each deformation mode [47]: $\tau^{eff.} = \tau^{true} + \Delta$, where $\tau^{eff.}$ and τ^{true} are effective and true CRSS; Δ is the internal stress arising from grain boundaries, dislocations and particles. In the case of polycrystalline Mg, Hutchinson and Barnett reported that the ratio of the $\tau^{eff.}_{pris.}$ and $\tau^{eff.}_{basal}$ reduces as the dislocation density increases from deformation. We can apply their equation to pyramidal $< c+a >$ and basal $< a >$ dislocations:

$$\frac{\tau^{eff.}_{py}}{\tau^{eff.}_{basal}} = \frac{\tau^{true}_{py} + \alpha G b^{py} \rho^{\frac{1}{2}}}{\tau^{true}_{basal} + \alpha G b^{basal} \rho^{\frac{1}{2}}}$$

where $\tau_{py}^{eff.}$ and $\tau_{basal}^{eff.}$ are effective CRSS for $< c+a >$ pyramidal slip and basal slip in polycrystals, respectively; τ_{py}^{true} and τ_{basal}^{true} are the true CRSS values in single crystal, respectively; α is a numerical constant; G is shear modulus; b_{py} and b_{basal} are Burgers vectors for $< c+a >$ and basal dislocations, respectively; ρ is dislocation density. Since b_{py} is larger than b_{basal}. The additive dislocation forest hardening term is greater for $< c+a >$ dislocation, reducing the anisotropy effectively. The implication is that the pre-existing or early-emerging dislocations would make $< c+a >$ pyramidal slip relatively easier in polycrystals. Applying this to the case of ND compression, grains with high c-axis off-angles may have basal dislocations at the very early stage, but those basal dislocations soon facilitate the ensuing $< c+a >$ slip in the grain. This in part explains the profuse $< c+a >$ dislocation activity in most grains of the ND samples, even in grains with large off-angle. For 45° compression sample, why $< c+a >$ dislocations were not observed? Such discrepancy could be explained by the profuse $\{10\bar{1}2\}$ deformation twinning, which requires lower stress than $< c+a >$ slip at this strain level.

Thirdly, unlike single crystals, the grain boundary restriction in polycrystals plays an important role during deformation. Under ND and 45° compressions, compatibility stresses will be induced from the grain boundaries to accommodate the uniform deformation of differently orientated grains. Under such condition, the actual stress status for the individual grains can not be simply represented by the global one. For example, in the ND compression experiment, the global stress is uniaxial compression along ND. However, due to the orientation spread and presence of grain boundaries, the exact stress status of individual grains are different and more complex. Thus, the individual grains experience traxial stress and the calculated Schmid factors in this study rather represent a means to help quantify the effect of orientation spread in the polycrystalline sample. Further detailed analysis from crystal plasticity modeling can be performed to calculate the actual complex stresses for individual grains.

Lastly, the strain localization could be induced by $\{10\bar{1}2\}$ deformation twins, which leads to the suppression of $< c+a >$ dislocations in the grains exhibiting small off-angles in the 45°-compression sample. Hazili *et al.* reported that the plastic deformation in polycrystalline Mg could

be largely non-uniform when $\{10\bar{1}2\}$ extension twins are activated. Most plastic strain is mediated by twinning [48]. In our 45°-compression sample, the grains with large off-angles deform by dislocations along twinning and are "soft" grains; the grains with small off-angles deform by only dislocations and are "hard" grains. Up to the global 2.6%, the "hard" grains experience much less strain than the "soft" grains. Thus, the local flow stress is not high enough to activate $< c + a >$ slip in the "hard" grains.

2.5 Conclusions

In conclusion, $< c + a >$ slip activities in grains of a highly textured polycrystalline AZ31 were statistically investigated using correlative microscopy. During ND compression up to 2.6% strain, $< c + a >$ dislocations are active in most grains even for those with c-axis up to 30° off the compression axis. In contrast, in 45° compression, none of the examined grains have $< c + a >$ slip activities even for those with c-axis merely 4° off the compression axis. The effect from the overall texture prevails over the orientation of individual grains in the deformation mode. It is a comprehensive result from the requirement of five independent slip systems and the reduction of anisotropy in polycrystalline Mg alloys. The former contributes to the activation and suppression of $< c+a >$ dislocations in both ND and 45° compression samples. The latter explains the promoted activities of $< c + a >$ slip in the ND sample. Taken together, The Schmid factor calculated for individual grains as single crystals using the global stress status can not represent the real Schmid factor with grain boundary compatibility stresses considering. This direct observations and statistics of $< c + a >$ dislocation activities in polycrystals here could also serve as a benchmark for crystal plasticity modeling.

3. EFFECT OF TWIN SCHMID FACTOR ON THE TENSION TWINNING ACTIVITIES IN A HIGHLY TEXTURED MG-3AL-1ZN ALLOY UNDER DIFFERENT LOADING CONDITIONS

3.1 Introduction

The $\{10\bar{1}2\} < \bar{1}011 >$ tension twinning (also called extension twinning) is an important deformation mode in Mg and its alloys to accommodate plastic strain [12, 49]. For Mg single crystals, the tension twins are activated when the samples are pulled parallel to the c-axis or compressed perpendicular to the c-axis [48, 50]. The tension twin boundaries are highly mobile. As plastic deformation proceeds, the tension twin boundaries could easily advance in the matrix, and eventually, the twins could consume most of the matrix. Similar observations have been made in highly textured polycrystalline Mg samples. For example, profuse tension twinning could be achieved by the rolling-direction (RD) compression and normal-direction (ND) tension in hot-rolled Mg samples, as well as the extrusion-direction compression in hot-extruded Mg samples [51, 13, 52, 53, 54, 55].

It is worth noting that although the hot-rolled and hot-extruded Mg exhibit strong textures, the exact orientation of each grain differs more or less from the global texture. Thus, the twin Schmid factors for tension twinning of individual grains are different even in a highly textured polycrystalline Mg sample. Beyerlein *et al.* [14], Barnett *et al.* [56], and Hong *et al.* [13] pioneered the work on investigating the effect of the twin Schmid factor on the $10\bar{1}2$ twinning activities in textured polycrystalline Mg. The general consensus is that the Schmid factor of individual grain greatly influences the propensity for twinning inside the grain, where a higher value of the Schmid factor leads to a larger area fraction, a larger number, and thicker twins [13, 14, 56]. It is worth noting that the twin Schmid factor is not the only feature that governs twinning. Grain size and grain boundary misorientation could also influence twin nucleation and growth. For example, smaller grains have less propensity to twin [14, 57]. "Twin transmission", where two twins are connected by a grain boundary, is more likely to happen across low angle grain boundaries than

the high angle ones [52, 14, 58].

To our knowledge, most EBSD investigations that correlate the twin Schmid factor and twinning behavior focus on highly textured polycrystalline Mg samples in the loading conditions where twinning is favored [13, 14, 56, 59, 60, 61]. It is important to point out that even when the loading condition does not generally favor twin formation (such as rolling direction tension), some twins could be observed locally [62, 63]. Thus, an interesting scientific question to ask is what is the effect of the twin Schmid factor of individual grains on their twinning behavior when the loading condition does not apparently favor twinning? In this work, we carried out systematic statistical analyses on the twinning activities in highly textured Mg-3Al-1Zn (AZ31, as the model system) under various loading conditions. The rolling direction (RD) compression and normal direction (ND) tension samples, in which tension twins are profuse, will be used as baselines. We further investigate the twinning behavior in the RD tension, ND compression, and 45° off-normal direction (refer to 45° off-ND) compression samples, in which twinning is discouraged in the similarly oriented single-crystal cases.

3.2 Materials and Methods

A hot-rolled AZ31 sheet was purchased from MetalMart International Inc. The bulk sample was annealed at 350 °C for 12h with Ar flow to remove the stored dislocations. Rectangular compression specimens (4 mm × 4 mm × 8mm) were electrical discharge machined (EDM) from the center of the hot-rolled plate along the ND, 45° off-ND, and RD. Dog-bone-shaped tension specimens with the gauge length of 8 mm and the cross section of 3×1.5 mm^2 were cut along the ND and RD. Uniaxial compression and tension tests were then conducted on all the specimens at a strain rate of 5×10^{-4} s^{-1}. The representative stress-strain curves were obtained from the above specimens strained to failure. All presented microscopy studies were performed on the specimens strained to 3%.

Electron backscatter diffraction (EBSD) was carried out on the AZ31 alloy at the initial and 3% strained stages. All microscopy samples were cut from the center region of the specimens. These samples were mechanically polished down to 1200 grit SiC paper and chemically polished

in a 5% nitric acid in methanol, then ion milled at liquid nitrogen temperature (Fischione) to produce mirror-like surfaces. EBSD mapping was performed using a Tescan FERA scanning electron microscope (SEM) equipped with an EBSD detector (Oxford Instrument) using a 20 kV electron beam and a 500 nm step size. Further statistical analyses on EBSD results were carried out using MTEX code [64] and Matlab.

3.3 Results and Discussion

The global EBSD inverse pole figure (IPF), (0001) pole figure (PF) of the as-hot-rolled sample confirmed the strong c-axis texture along the ND (Figure 3.1a). The average grain size measured is approximately 10 μm. The mechanical properties of the hot-rolled AZ31 in this study are consistent with what has been reported in the literature [44, 45, 13]. As shown in Figure 3.1b, the ND compression (ND-C, light blue) and RD tension (RD-T, dark blue) stress-strain curves do not show a sharp yielding transition. The yield strength, ultimate strength, and strain to failure for ND-C were measured to be 107 ± 4 MPa, 296 ± 18 MPa, 9.9% ± 0.8% and for RD-T 173 ± 7 MPa, 277 ± 13 MPa, 12.7% ± 1.2%, respectively. The shape of the curves was expected, as dislocation-mediated plasticity is the predominant deformation mode, which has also been confirmed by our previous studies [65, 62]. In contrast, the RD compression (RD-C, orange) and ND tension (ND-T, red) stress-strain curves both exhibit a clear yield transition followed by a low strain hardening. The yield strength, ultimate strength, and strain to failure for RD-C were measured to be 74 ± 1 MPa, 410 ± 8 MPa, 13.9% ± 0.7%, and for ND-T 63 ± 2 MPa, 295 ± 15 MPa, 14.2% ± 1.3%. The sigmoid shape of the curves indicates twinning as the dominant deformation mode in the early stage of the deformation. This observation is also expected since the RD-C and ND-T are typical twinning-favored loading conditions for highly textured Mg alloy [13]. For the 45° off-ND compression (45°-C, green), the curve shape is similar to the ND-T condition, which also implies twinning plays an important role during the deformation. The yield strength, ultimate compressive strength, and strain to failure were measured to be 71 ± 1 MPa, 355 ± 3 MPa, and 16.5% ± 0.5%, respectively.

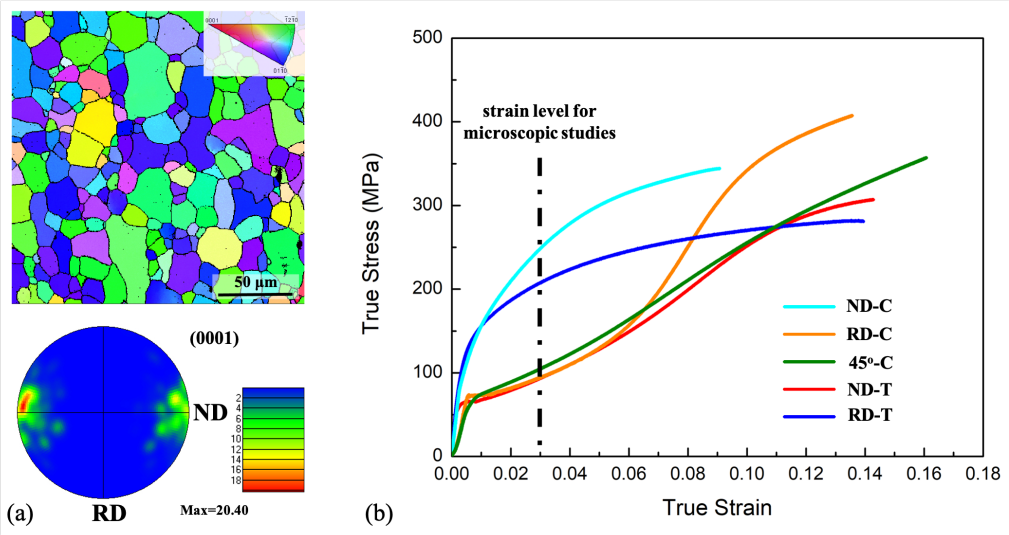

Figure 3.1: (a) EBSD out-of-plane IPF maps with the corresponding (0001) pole figure of the highly textured AZ31 alloy; (b) True stress-strain curves of AZ31 under compression along rolling direction (RD-C, orange), normal direction (ND-C, light blue), 45° off normal direction (45°-C, green) and tension along rolling direction (RD-T, dark blue), normal direction (ND-T, red).

To uncover the effect of twin Schmid factor (SF) on the tension twinning of individual grains, EBSD was carried out on the 3% strained samples deformed at various conditions (twinning-favored and unfavored conditions). For the twinning-favored conditions (RD-C and ND-T), as shown in the IPF maps (Figure 3.2a and 3.2e), numerous twins were activated and confirmed as tension twin (TT) in both cases (Figure A.1). However, one major difference is that multiply parallel twins were activated within individual grains in the RD-C sample, but intersected twins are profuse in the ND-T sample. To explain the difference, one may consider the single-crystal scenarios. For compression perpendicular to the c-axis, mostly one twin variant with the highest SF is activated, leading to a parallel twin structure [52]. In contrast, for tension parallel to the c-axis, all six twin variants could be activated, leading to the intersecting twin structure [13].

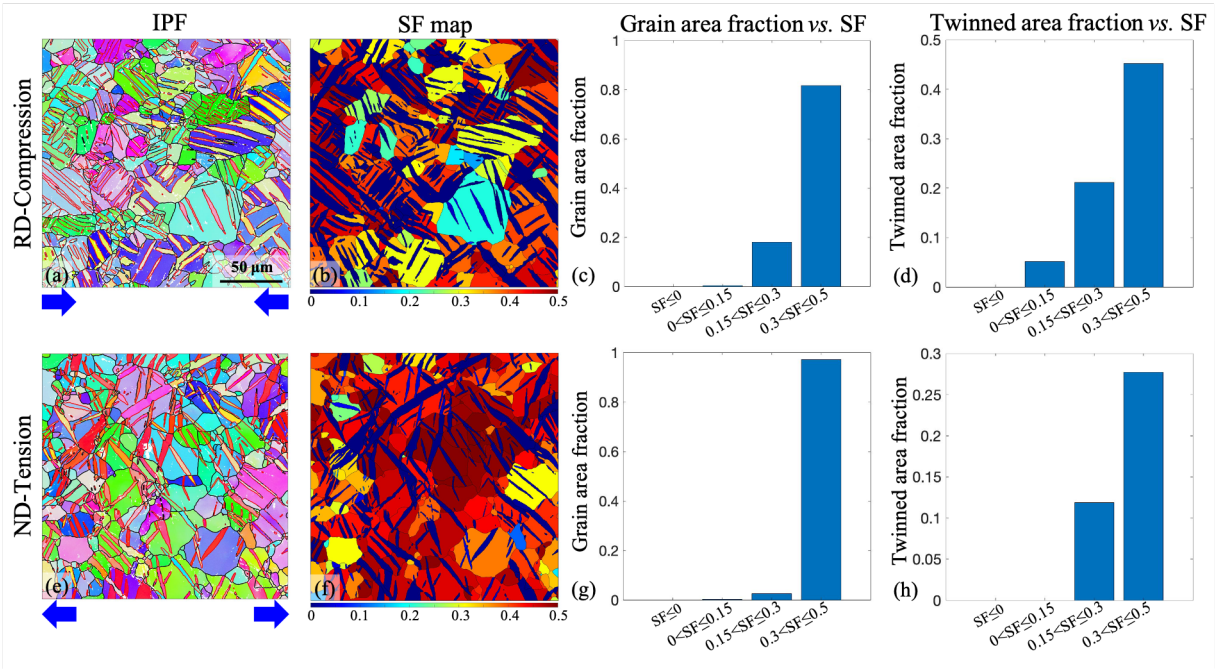

Figure 3.2: (a) (e) EBSD IPF maps (out-of-plane crystal orientation) of the highly textured AZ31 alloy deformed under twinning-favored conditions (rolling direction (RD) compression and normal direction (ND) tension); (b) (f) Tension twin (TT) Schmid factor (SF) maps created based on the IPF maps and loading directions; (c) (g) Grain SF distribution, where the twins were considered to be a part of the parent grains; (d) (h) TT area fraction distribution (only in the grains with twins).

To systemically study the role of SF on TT activities, SF maps (Figure 3.2b and 3.2f) were created based on the IPF maps and loading directions. Note the SF maps used the highest TT variant SF for each grain. The grains with negative SF were colored with a single dark blue color. Most negative and zero SF regions in the SF maps come from the twins, as shown in Figure 3.2b and 3.2f. Histograms depicting the grain SF distribution are shown in Figure 3.2c and 3.2g. In these histograms, the twins were treated to be part of the parent grain. The SF of the parent grain was assigned to the twins when doing the statistics. In both the RD-C and ND-T samples, most grains have high TT SF. For example, RD-C contains $\sim$80% and ND-T contains $\sim$97% grains by area exhibiting TT SF greater than 0.3. No grain with negative TT SF was observed.

Figures 3.2d and 3.2h demonstrate the further statistical analyses on the TT area fraction only in the grains contain twins. Here, we briefly explain how to interpret the results. For example, in

the RD-C sample, ∼80% of grains have SF > 0.3 (Figure 3.2c). Among these grains, ∼48% of areas are twinned (Figure 3.2d). The total twinned area fraction in the entire map is ∼38% (80% × 48%) for grains with SF > 0.3. There is a clear trend that higher TT SF leads to a larger area fraction of twins in both cases (Figure 3.2d and 3.2h), indicating TTs are more likely to be activated in higher SF grains. Moreover, for the grains with SF > 0.3, the twin area fraction is greater in the ND-T sample (∼48%) than the RD-C sample (∼28%). The lower fraction under the ND-T loading condition could be attributed to the twin-twin interactions, retarding the growth of existing twins, even in the grains exhibiting high TT SF. However, under the RD-C loading condition, only one twin variant was primarily active, resulting in more parallel twins. Thus, the parallel-twin structure allows for more twin growth.

For the twinning-unfavored conditions (ND-C and RD-T samples), the same methodology was adopted to study the SF effect on TT activities. In these conditions, dislocations are expected to be the major plastic carrier. As shown in the IPF maps (Figure 3.3a and 3.3e), only a few twins were observed and confirmed as TTs (Figure A.2) [62, 65]. The lack of TT can be explained by the SF maps (Figure 3.3b and 3.3f) and grain area fraction histograms plotted as a function of TT SF, in which most grains (∼98% by area) have TT SF < 0.15 in both samples. Similar to the twin-favored conditions (RD-C and ND-T), the propensity of twinning in the twin-unfavored conditions (ND-C and RD-T) is also positively correlated with TT SF, as shown in Figure 3.3d and 3.3h. Higher TT SF tends to result in a higher area fraction of twins. Thus, the activation of TT generally obeys the SF law, regardless of whether the global loading conditions promote or inhibit TT. However, it is interesting to point out twins were observed in some grains with very small and even negative TT SF. This could arise from local stress concentrations near the grain boundaries and the stochastic nature of the nucleation events to satisfy strain compatibility [66, 67]. In the twin-favored loading conditions, no twins were observed in grains with negative TT SF. This is due to the fact that no grains exhibit negative TT SF in such loading conditions (Figure 3.2c and 3.2g). We speculate if grains with negative TT SF were present, some TTs might be activated, but the area fraction would be very small, and the positive correlation of twin area fraction and TT SF is not altered.

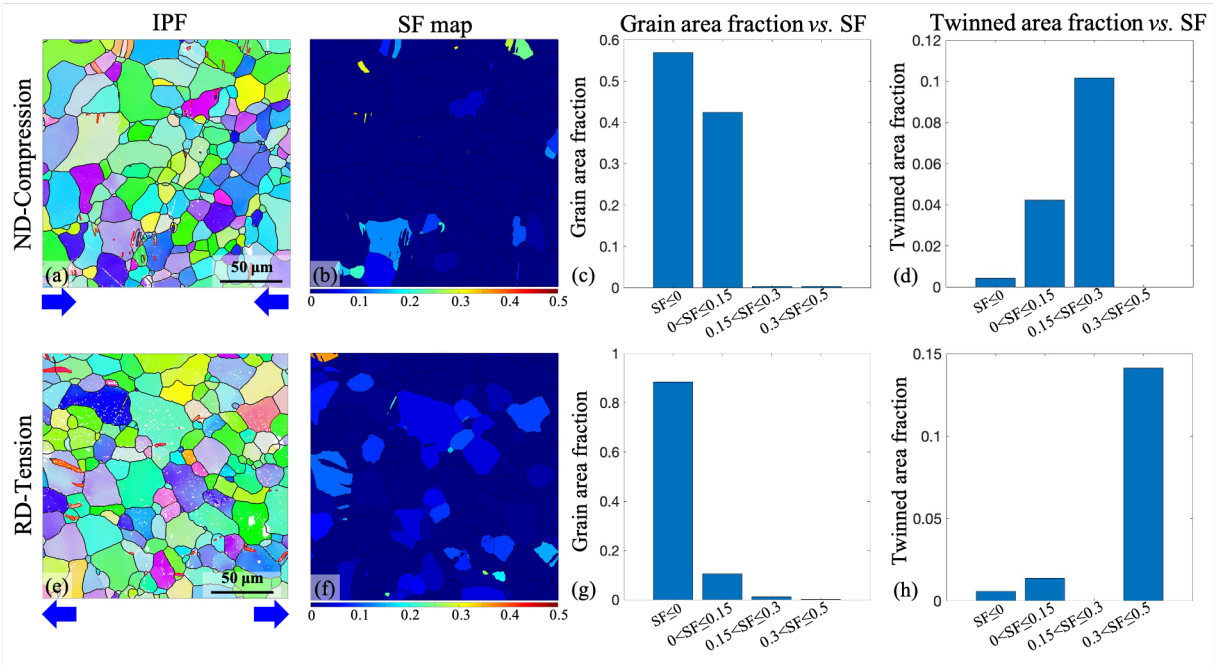

Figure 3.3: (a) (e) EBSD IPF maps (out-of-plane crystal orientation) of the highly textured AZ31 alloy deformed under twinning-unfavored conditions (normal direction (ND) compression and rolling direction (RD) tension); (b) (f) Tension twin (TT) Schmid factor (SF) maps created based on the IPF maps and loading directions; (c) (g) Grain SF distribution (SF of the parent grain assigned to the twins); (d) (h) TT area fraction distribution (only in the grains with twins).

To further verify the SF effect on TT, EBSD was also carried out on the sample under 45° off-ND with most of the grains' c-axis 45° off the loading direction. In a single crystal sample, such loading condition would only activate basal slip without any TTs. Since the material we use is a polycrystalline sample, the presence of grain boundary and the variation of the exact crystal orientation also triggered twin nucleation and growth, as shown in Figure 3.4a. Approximately half of the grains were found to contain parallel TTs (Figure 3.4a and A.3). The SF maps show a wide range of possible TT SF compared with all previous cases, as evidenced by the coexistence of red (high TT SF) and dark blue (negative TT SF) grains in the same map (Figure 3.4b). The wide range of SF distribution offers an excellent opportunity to validate the relationship of twin area fraction and TT SF of individual grains obtained from the above loading conditions. The grain area distribution vs. TT SF is comparatively more uniform, with TT SF of ∼40% grains

by area being negative, of $\sim$20% being positive but < 0.15, and of $\sim$40% being > 0.15. In this sample, the twinned area fraction distribution also displays a strong positive correlation with the TT SF, confirming previous observations. Moreover, there are two interesting observations. First, many twins were observed to be parallel in the same grains, which is similar to the RD-C TT morphology. The similarity could be explained by the compressive loading in both cases, where one twin variant with the highest SF is prone to operate to accommodate plasticity. Second, the twin area fraction for each TT SF range (Figure 3.4d) is comparable to those observed in the RD-C and ND-C conditions (Figure 3.2d and 3.3d). The similarity is especially apparent in the grains with large TT SF (e.g., > 0.3). For example, the twinned area fractions among the grains with SF > 0.3 are $\sim$45% for both 45°-C and the RD-C, suggesting the TT SF is one dominant factor that determines the TT area fraction. The exact loading condition plays a minor role. However, we also noted that the twin area fraction in the low TT SF grains from the 45°-C sample appears to be higher than those measured from the RD-C and ND-C samples. For example, the twin area fraction of the grains with 0 < SF < 0.15 from the 45°-C, RD-C, and ND-C are $\sim$17%, $\sim$5%, and 4%, respectively. The discrepancy may be explained by the poor statistics due to a lack of grains with such TT SF in the RD-C sample and too few twins, thus limited "twin transmission" in the ND-C sample. Nonetheless, such a small disparity does not change the core observation from this study that the twin area fractions of individual grains are strongly correlated with their own TT SFs.

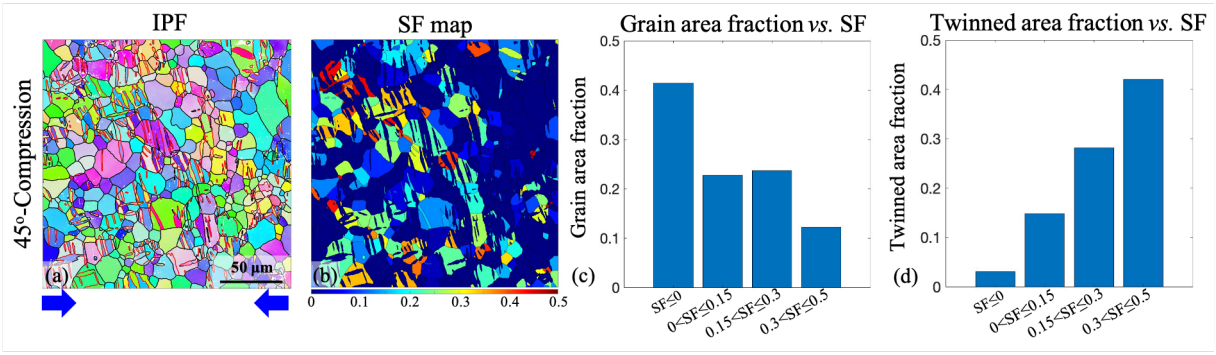

Figure 3.4: (a) EBSD IPF maps (out-of-plane crystal orientation) of the highly textured AZ31 alloy deformed under 45° off normal direction compression (45° Compression); (b) Tension twin (TT) Schmid factor (SF) maps created based on the IPF maps and loading directions; (c) Grain SF distribution (SF of the parent grain assigned to the twins); (d) TT area fraction distribution (only in the grains with twins).

It is worth noting that the strong twin-SF relationship does not hold true for the dislocation-SF relationship ($< c + a >$ dislocations in particular). Our previous study on the $< c + a >$ dislocation activation in the same model material (AZ31) [65] demonstrated a weak correlation with SF. In the ND-C samples, $< c + a >$ dislocations were observed even in grains with large off-c-axis angles. The operation of $< c + a >$ is due to the presence of existing basal $< a >$ dislocations that reduces the effective critical resolved shear stress of $< c + a >$ dislocations [65]. In the 45°-C samples, no $< c + a >$ dislocation was observed even in the grains with high $< c + a >$ slip SF. The absence of $< c + a >$ dislocations is attribute to the "hard" grain vs. "soft" grain deformation sequence, where the deformation localized in the "soft" grains, rendering no $< c + a >$ dislocations in the "hard" high $< c + a >$ SF grains. In contrast, TTs are less affected by the above microstructural features and deformation heterogeneity. For example, pre-existing dislocations were reported to slightly delay twin nucleation but have no apparent effect on twin growth [68], which does significantly modify the resolved shear stress for twining nucleation and growth. Moreover, compared to $< c + a >$ slip, TT is a much easier deformation mode [17]. The high TT SF grains are thus "soft" grains, from which twins are easily observable even in very early stages of plastic deformation. Therefore, the $< c + a >$ dislocation operation is more governed by

the global texture, whereas the twin activation is more determined by the TT SF of each grain.

3.4 Conclusions

In summary, tensile twinning generally obeys the Schmid criterion that the tensile twins are more likely to be activated in the grains with larger Schmid factors. The tension twin area fraction is positively correlated with the grains' Schmid factors. The Schmid law holds true for tension twinning regardless of whether the global stress state favors tension twinning or not. This is in contrast to the reported weak correlation of $< c + a >$ dislocations and Schmid factor [65].

4. SIGNIFICANT DISPARITY OF NON-BASAL DISLOCATION ACTIVITIES IN HOT-ROLLED HIGHLY-TEXTURED MG AND MG-3AL-1ZN ALLOY UNDER TENSION[1]

4.1 Introduction

Magnesium (Mg) and its alloys are promising lightweight (1.7 g/cm^3 density) and high specific strength structural materials, especially in transportation and aerospace industries where high energy consumption is a concern. However, pure Mg and many Mg alloys exhibit low room-temperature ductility and formability, which constrain their wider applications. The poor ductility and formability are due to the low-symmetry hexagonal close-packed (HCP) crystal structure and its high plastic anisotropy [8]. The easiest slip system in Mg is the $< a >$ dislocation ($\mathbf{b} = \frac{1}{3} < 11\bar{2}0 >$) on the (0001) basal plane. The critical resolved shear stress of basal $< a >$ dislocations could be as low as 0.5 MPa [19, 21, 69, 17]. Non-basal slip systems are much more difficult to activate. For example, the CRSS values of prismatic $< a >$ on the $\{10\bar{1}0\}$ planes have been reported in the range of 30-50 MPa [19, 20, 70, 71]. The pyramidal $< c + a >$ dislocations (with $\mathbf{b} = \frac{1}{3} < 11\bar{2}3 >$ on $\{10\bar{1}1\}$ or $\{11\bar{2}2\}$) [69] have even higher CRSS of 30-80 MPa [19, 69, 70, 71]. Since the plasticity of polycrystalline metals requires five independent slip systems [18], where basal $< a >$ could only provide two, non-basal slips (sometimes twins) have to operate. Recently, substantial effort has been devoted to understanding the behavior of $< c + a >$ dislocations [26, 43, 10, 27, 72, 42, 11, 65]. Many believe improved $< c+a >$ dislocation activities could lead to an improved ductility in Mg alloy design.

The activation of $< c + a >$ dislocations is the dominant plastic deformation mechanism for c-axis compression in both single crystals and highly textured polycrystal Mg samples [7, 29]. The mobility of $< c + a >$ dislocations and their ability to cross slip have been associated with the ductility of Mg and Mg alloys. The $< c + a >$ dislocation Burgers vector ($\mathbf{b} = \frac{1}{3} < 11\bar{2}3 >$)

[1]Reprinted with permission from "Significant disparity of non-basal dislocation activities in hot-rolled highly-textured Mg and Mg-3Al-1Zn alloy under tension" by Dexin Zhao, Xiaolong Ma, Abhinav Srivastava, Griffin Turner, Ibrahim Karaman, Kelvin Y Xie. Acta Materialia, vol. 207, p.116691. Copyright (2021).

and slip planes (pyramidal II $\{11\bar{2}2\}$) were first experimentally identified by Obara *et al.* [7] using transmission electron microscopy (TEM) and the slip trace analysis on c-axis compressed Mg single crystals. The authors also noted that $< c+a >$ dislocation lines lie on the basal planes. More recent slip trace analysis demonstrated $< c+a >$ dislocations are also active on the $\{10\bar{1}1\}$ pyramidal I plane [22]. The observation that $< c+a >$ dislocations are "long and straight" and "basal-bound" have been reported in many following studies, not only in pure Mg but also in many Mg alloys (such as Mg-Al, Mg-Al-Zn, Mg-Y, Mg-Li, etc.) [25, 26, 27, 11, 65, 28, 9, 36]. However, by doing careful tilting experiments in TEM, Geng *et al.* [25, 9], Xie *et al.* [11], and Ma *et al.* [3] have revealed the $< c+a >$ dislocations are actually curved and bowing on the basal plane. The "long and straight" misconception is caused by projection when the basal plane was aligned parallel to the incident electron beam direction. Moreover, the $< c+a >$ dislocations could easily dissociate into partials and stacking faults in pure Mg [9, 11], but they have a more compact core in the Mg-3Al-1Zn alloy (AZ31) [3].

The experimental effort to understand the characteristics of $< c+a >$ dislocations is paralleled by a number of computational works [43, 10, 27, 72, 73, 74, 75, 76, 77, 78]. Wu and Curtain [10] used molecular dynamics (MD) simulations and predicted the $< c+a >$ dislocation core in pure Mg is metastable and undergoes a thermal-assisted core transition from pyramidal to the basal plane. The dislocation could either dissociate into sessile partials with a stacking fault in between [10, 79] or decompose into $< a >$ and $< c >$ dislocations. For glissile $< c+a >$ dislocations on the pyramidal planes before the locking, Srivastava and El-Awady [72] pointed out that their motions involve atomic shuffling and kink pair formation of the trailing partial. Wu and Curtin [27] further suggested solid solution elements (such as Ca, Mn and Y) could promote the cross slip and multiplication of $< c+a >$ dislocations, thus leading to the improved ductility of Mg. Among the alloying elements, the authors predicted rare earth (Ce, Gd, and Y) could dramatically enhance the cross slip of $< c+a >$ dislocations, while Al and Zn only moderately improve it. In contrast, many experimental works indicated Mg alloys containing Al and Zn have the significantly improved ductility [8, 29, 3, 76, 30, 80, 81]. The disparity between the theoretical prediction and

the experimental observation implies there are key mechanisms that accounts for the increased ductility but not yet revealed.

In our literature survey, we note that $< c + a >$ dislocations are ubiquitous in compression samples, where the loading direction is parallel to the c-axis of most grains [65]. However, to obtain tensile ductility information, tensile tests (with the loading direction perpendicular to the c-axis of most grains) should be performed. Very recently, a few groups performed tensile experiments on AZ31, Mg-Y, Mg-Gd, Mg-Ca, followed by TEM observations [8, 27, 32, 82, 83, 35, 33, 34]. Surprisingly, no significant roles of $< c + a >$ dislocations were reported in most of them, except for AZ31 near-twin and grain boundary regions [8], one fine-grained ($\sim$3 μm) Mg-Gd sample [34] and Mg-Y samples [27]. Instead, non-basal $< a >$ dislocations are profuse in the deformed samples. The lack of $< c + a >$ dislocations may be attributed to three reasons. First, Mg-RE and Mg-Ca exhibit weaker texture than pure Mg and AZ Mg alloys. The activation and suppression of $< c+a >$ dislocations are dictated by the global texture of the sample rather than the orientation of individual grains [65, 29]. The weakened texture may lead to a lack of $< c+a >$ dislocations in the deformed samples. Second, $< c + a >$ dislocations may not be required at all to accommodate the plastic flow when the tensile loading direction is mostly perpendicular to the c-axis of the grains in Mg and Mg alloy samples. Third, the addition of solute elements could modify the CRSS of $< c+a >$ dislocations, which consequently changes the CRSS differences of the $< c+a >$ slip to the other slip systems (e.g. basal $< a >$ and non-basal $< a >$). A larger CRSS gap may preclude $< c + a >$ dislocations to be activated.

We also note some authors correlated tensile sample failure with shear banding in Mg alloys. Kang *et al.* [84] used digital image correlation (DIC) and showed the inhomogeneous deformation of AZ31 under tension. Numerous contraction twins were observed within the shear bands at a strain level of $\sim$10%, which could lead to failure. Scott *et al.* [85, 86] characterized the shear band microstructure at different strain levels. The shear bands in the 7% strained AZ31 sample contains tension twins, while the ones in the 14% strained samples comprise contraction twins. In both cases, the authors pointed out the prevalent roles of twinning on shear banding, but did not address

how dislocation activities (e.g., $< c + a >$ v.s. non-basal $< a >$) would affect shear banding.

To answer these questions, we performed tensile tests along the rolling directions of a hot-rolled pure Mg and an AZ31 Mg alloy with strong basal textures. In this condition, the loading direction is perpendicular to the c-axis (also parallel to the basal planes) of most grains in both samples. Optical microscopy and electron backscatter diffraction (EBSD) were firstly preformed to understand the failure mechanisms. We noticed profuse shear bands presented in pure Mg during deformation but not in the AZ31. Then the TEM observations were carried out to identify the dislocation characteristics at various strain levels. We observed high density of $< c + a >$ dislocations in pure Mg. In contrast, $< c+a >$ dislocations were only observed in very few grains in the AZ31 alloy. These observations highlight the effect of alloying elements on the deformation mechanisms of Mg when the samples are stretched away from the c-axis. A correlation among dislocation activities, shear banding, and ductility could be established. We suggest the disparity of dislocation activities leads to the different propensity of shear banding, and consequently the different ductility observed in pure Mg and AZ31. The insight gained from this work also sheds light on the ductility engineering of Mg by manipulating the activation and suppression of certain types of dislocations via suppressing shear banding.

4.2 Materials and Methods

Hot-rolled pure Mg and AZ31 sheets purchased from MetalMart International Inc. were selected for this study. The bulk samples were annealed at 350 °C for 12 hours under Argon flow atmosphere to homogenize the microstructure. The microstructures of the pure Mg and AZ31 after homogenization are similar, as evidenced by the global inverse pole figure (IPF) maps, (0001) pole figures (PFs), grain size distribution plot, and the misorientation angle distribution histograms shown in Figure 4.1. The undeformed pure Mg demonstrates a strong c-axis texture along the normal direction (ND), with a minor amount of remnant extension twins ($\sim$1%). The average grain size was measured to be approximately 25 μm from the grain size distribution plot. For the undeformed AZ31, basal texture along ND was also confirmed from the IPF map and PF (Figure 4.1b). The average grain size is $\sim$14 μm. Note the grain size in both pure Mg and AZ31 are greater

than 10 μm (with the coarse grain microstructure). In this scale, the deformation mechanisms are less sensitive to size effect. Thus the alloying effect on deformation mechanisms could be directly studied. After confirming initial microstructure, dog-bone-shaped specimens from both pure Mg and AZ31 were cut using an electrical discharge machine (EDM) into the gauge length of 8 mm and the cross section of 3 × 1.5 mm^2 from the plate center regions along the rolling direction (RD) (schematic is shown in the inset of Figure 4.2). Uniaxial tensile tests were conducted on an MTS machine at a strain rate of 5×10^{-4} s^{-1}. The tensile tests were purposely stopped at various strain levels for microscopy analysis. For each strain level, at least two specimens were tested.

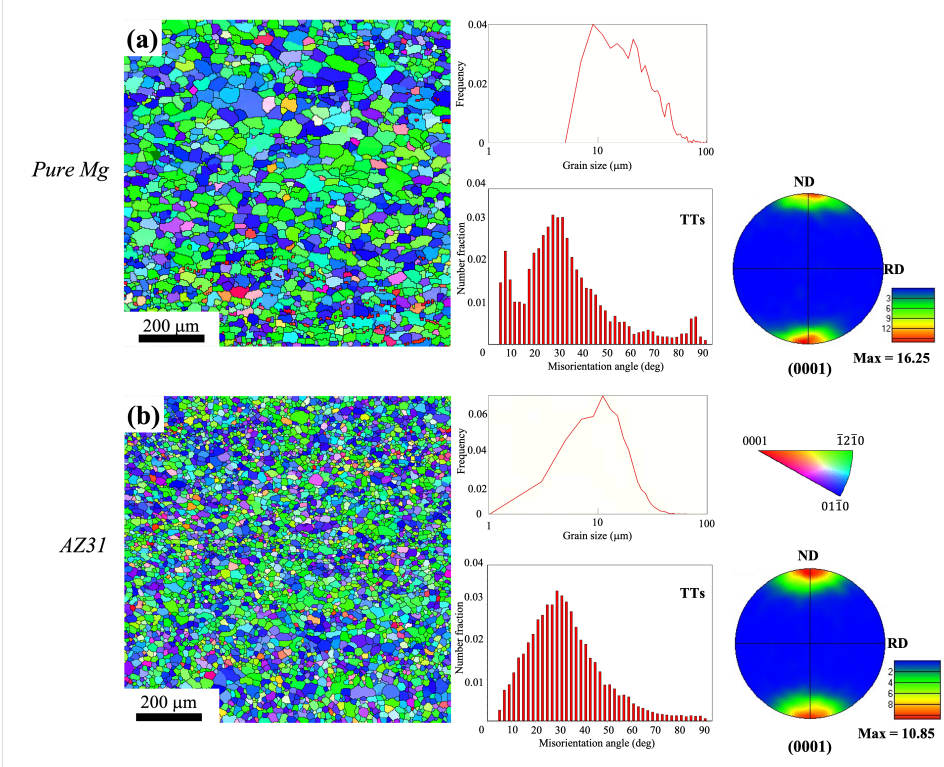

Figure 4.1: Out-of-plane IPF maps, grain size distribution plots, misorientation angle distribution histograms, and (0001) pole figures of the hot-rolled pure Mg and AZ31 after homogenization, revealing similar microstructure.

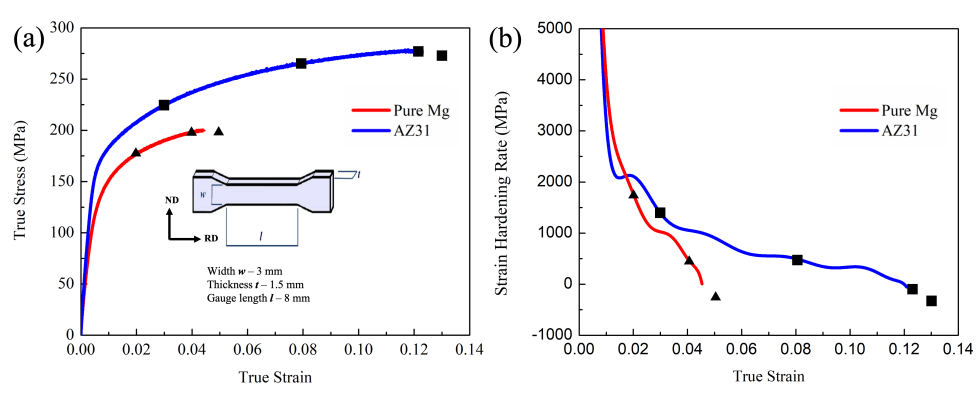

Figure 4.2: (a) True stress-strain curves of the hot-rolled pure Mg and AZ31 under RD tension, and (b) corresponding strain hardening curves. Dog-bone-shaped tensile specimen dimensions are shown in the inset. Squares and triangles indicate the selected strain levels for microscopic studies.

To reveal the microstructure, optical microscopy, EBSD and TEM were performed on the pure Mg and AZ31 strained at different levels (including the initial specimens, as labeled in Figure 4.2a and b). Optical microscopy, EBSD, and TEM were selected to reveal the overall, granular, and dislocation information, respectively. Pure Mg and AZ31 tensile bars were polished down to 1200 grit SiC paper then strained after load drop before fracture for optical microscopy. For EBSD analysis, all specimens were mechanically polished to 1200 grit SiC abrasive paper, and chemically polished in a 5% nitric acid in methanol, then ion milled at liquid nitrogen temperature (Fischione) to produce mirror-like surfaces. EBSD mapping was carried out using a Tescan FERA scanning electron microscope (SEM) equipped with an EBSD detector from the Oxford Instrument with a 20 kV acceleration voltage and a 500 nm step size. To obtain TEM specimens, samples were first mechanically polished to $\sim$100 μm (down to 1200 grit abrasive paper on both sides), then punched into 3 mm discs. When doing the TEM on the fractured samples, we selected the part with uniform deformation and being away from the necked regions. These discs were twin-jet electropolished using a Tenupol-5 polishing system with a solution of 15.9 g lithium chloride, 33.5 g magnesium perchlorate, 1500 ml methanol, and 300 ml 2-butoxy-ethanol at -40 °C.

Dislocations were imaged using the 2-beam bright-field (BF) and weak beam dark-field (WBDF) techniques on an FEI Tecnai TEM operating at 200 kV. To reveal the dislocation characters, we

performed careful tilting experiments near the $[2\bar{1}\bar{1}0]$ (or $[01\bar{1}0]$]) zone of the examined grains and used $\mathbf{g} \cdot \mathbf{b} = 0$ invisibility criterion to illuminate $< a >$ and $< c >$ components separately. The **g**-vectors we used to illuminate dislocations are $\mathbf{g} = [0002]$ (all c-component) and $\mathbf{g} = [01\bar{1}0]$ (two-thirds of a-component). If a dislocation is visible under both $\mathbf{g} = [0002]$ and $\mathbf{g} = [01\bar{1}0]$ conditions, it is of the $< c + a >$ type. For each strain level, roughly 10 grains were selected to statistically study the dislocation activities. We also imaged dislocations at the $[0001]$ zone of some crystals using precession electron diffraction (PED) with a 0.3° precession angle and a 3 nm step size [87, 88, 89]. The advantage of PED over conventional dislocation imaging is the elimination of most dynamical effects, leading to a crisper dislocation contrast. Moreover, we performed correlative microscopy [65], where EBSD was carried out on the foils along with their TEM observations to correlate the dislocation activities of individual grains to their own Schmid factors so that the deformation mechanisms could be clearly elucidated.

4.3 Experimental Results

4.3.1 Mechanical properties of pure Mg and AZ31

Two representative true stress-strain curves from the pure Mg (red) and AZ31 (blue) are shown in Figure 4.2a. The mechanical properties of the hot-rolled pure Mg and AZ31 in this study are consistent with what has been reported in the literature [8, 29, 38, 90, 91]. The pure Mg samples exhibit 144 ± 4 MPa yield strength, 199 ± 8 MPa ultimate tensile strength and 5% ± 0.8% strain to failure. The AZ31 sample show much higher strength and better ductility, with 173± 7 MPa yield strength, 277 ± 13 MPa ultimate tensile strength and 12.7% ± 1.2% strain to failure. Three different strain levels (2%, 4%, and fracture) for pure Mg and four strain levels (3%, 8%, 12%, and fracture) for AZ31 were chosen for microstructure characterization. The strain hardening rates of pure Mg and AZ31 are comparable in the first 2% of deformation. Beyond 2% strain, the strain hardening rate of AZ31 decreases much slower than that of the pure Mg, which is necessary for a decent ductility by delaying instability and necking (Figure 4.2b).

4.3.2 Fracture characteristic of pure Mg and AZ31

Optical micrographs (OMs) of deformed pure Mg and AZ31 tensile bars strained to load drop before fracture were shown in Figure 4.3a and b, where AZ31 exhibits much larger elongation. At the microstructure level, one striking difference is that apparent band-like structures are only present in the deformed pure Mg (highlighted by the blue dashed lines in Figure 4.3a). These bands appear 30°-40° inclined from the loading direction. It is also interesting that a crack appears to travel along one of the band-like structures (indicated by the red dashed line), which may further propagate and lead to fracture. In contrast, no such band-like structures were noted in the deformed AZ31 tensile bars (Figure 4.3b), although multiple cracks have started to form (see red dashed lines) during load drop. To have a closer inspection of the band-like structure in pure Mg, we also performed EBSD. The IPF map shows good indexing of the grains outside the band but poor indexing within the band. Poor indexing in EBSD is usually caused by large strain stored in the region. Combining the optical and EBSD observations, we could conclude the band-like features are shear bands [89].

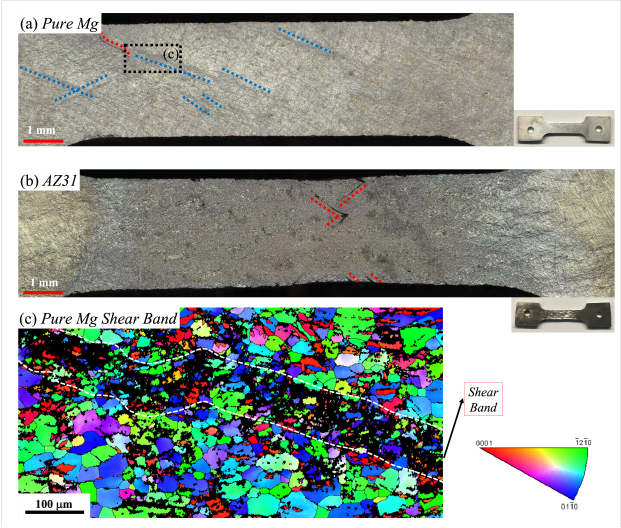

Figure 4.3: Optical micrographs of (a) pure Mg and (b) AZ31 tensile bars strained after load drop before fracture. Shear bands can be seen in pure Mg from both (a) the optical micrograph (blue dashed lines) and (c) the IPF map (white dashed lines). Red dashed lines refer the early stage cracks.

The photographs of the fracture pure Mg and AZ31 tensile samples are shown in Figure 4.4a and d, respectively. Note apparent shear bands are visible in the photograph of the fractured pure Mg samples (indicated by the blue arrows in Figure 4.4a). The fracture surfaces of pure Mg exhibit 30° -40° to the loading direction, while the fracture surfaces in AZ31 samples appear much flatter. The corresponding SEM micrographs of the fracture surfaces of Mg (Figure 4.4b-c) and AZ31 (Figure 4.4e-f) also showed they fractured via different mechanisms. For pure Mg, relatively flat facets (Figure 4.4b red dashed circle, corresponding to cleavage-like fracture) with fewer dimples (Figure 4.4c green circle) were observed, indicating a mixture of brittle and ductile failure. In contrast, profuse dimples and no apparent evidence of cleavage-like fracture were noted from the fracture surface SEM micrographs of the AZ31 samples (Figure 4.4e-f), indicating dominantly ductile failure. The differences in the fracture mechanisms corroborate the much better ductility observed in AZ31 compared to pure Mg.

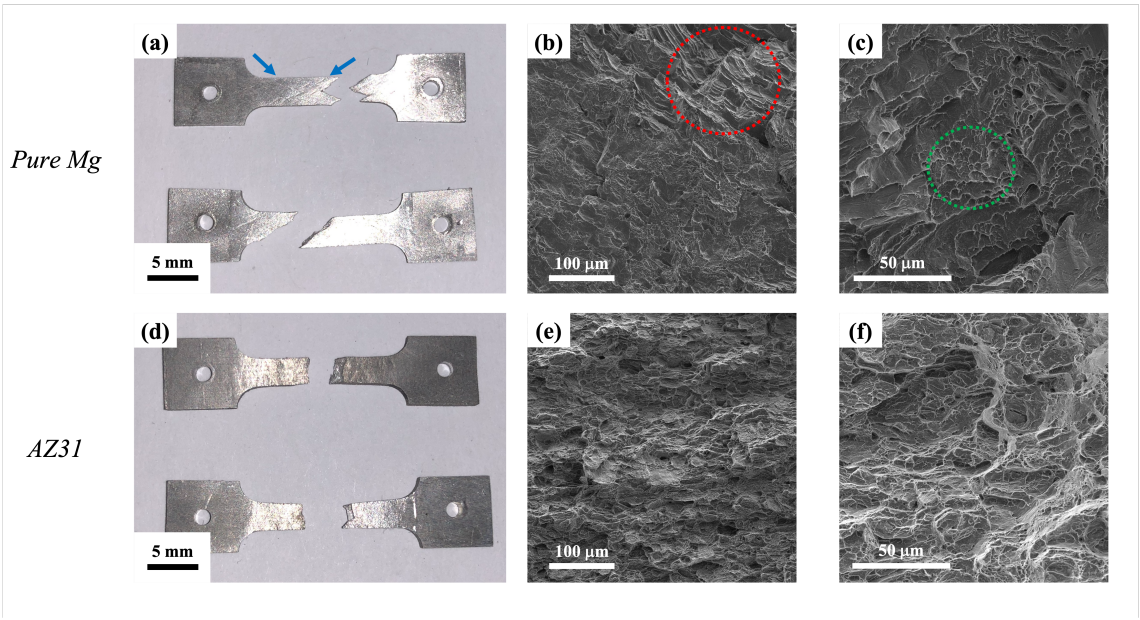

Figure 4.4: The photographs of the fractured pure Mg and AZ31 tensile samples and the corresponding fracture surface SEM images. Red and green dashed circles refer to the cleavage-like fracture and dimple regions, respectively, on the pure Mg fracture surface. Bule arrows indicate shear bands.

4.3.3 Granular-level microstructural evolution of pure Mg and AZ31

As described previously, the initial microstructure for both pure Mg and AZ31 is largely twin-free. For pure Mg, with increasing strain levels from 2% to fracture (Figure 4.5b-d), the dominant texture remained. However, some tension twins (TTs) were activated. These TTs are nucleated at the local stress concentration regions and operated to accommodate strain incompatibility. For AZ31, with an increasing strain from 3% to fracture (Figure 4.6b-e), the resultant microstructural evolution is similar to that in pure Mg, where the strong basal texture persisted and TTs presented. It is worth noting that the TTs are more prominent in pure Mg than AZ31. For example, 6% (area fraction) TTs were observed in the fractured ($\sim$5% strain) pure Mg samples, while only 2% TTs in AZ31 even at a much larger strain of $\sim$8%. The role of TTs on ductility and fracture behavior will be discussed later. We also noticed a very small amount of compression twins (CTs) in the deformed AZ31, but not in pure Mg. Since the area fraction is very small ($\sim$0.02% in the 8% strained sample), their roles are expected to be minute in contributing to the overall plasticity. Regardless, the dislocation slip is expected to be the primary plasticity carrier in AZ31 under this loading condition.

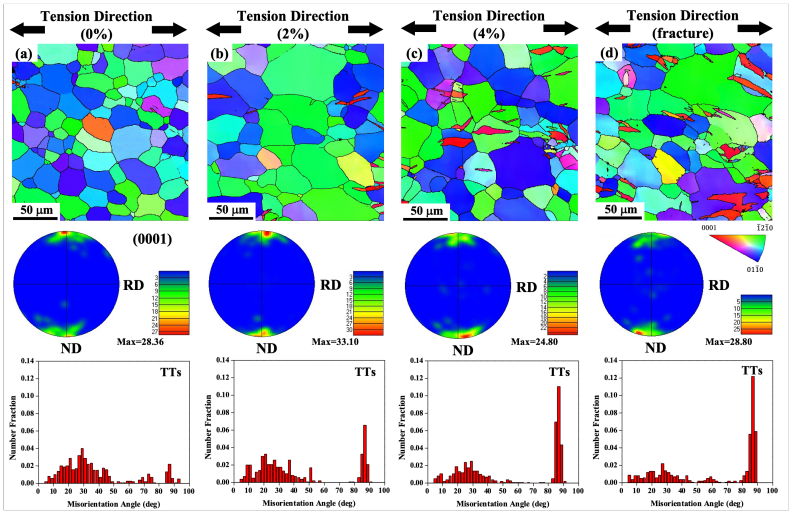

Figure 4.5: Out-of-plane IPF maps, the corresponding (0001) pole figures, highest mud values, and misorientation angle distribution histograms of pure Mg at (a) undeformed stage, (b) 2% strain, (c) 4% strain, and (d) fracture under RD tension. Some tension twins (TTs) were noted.

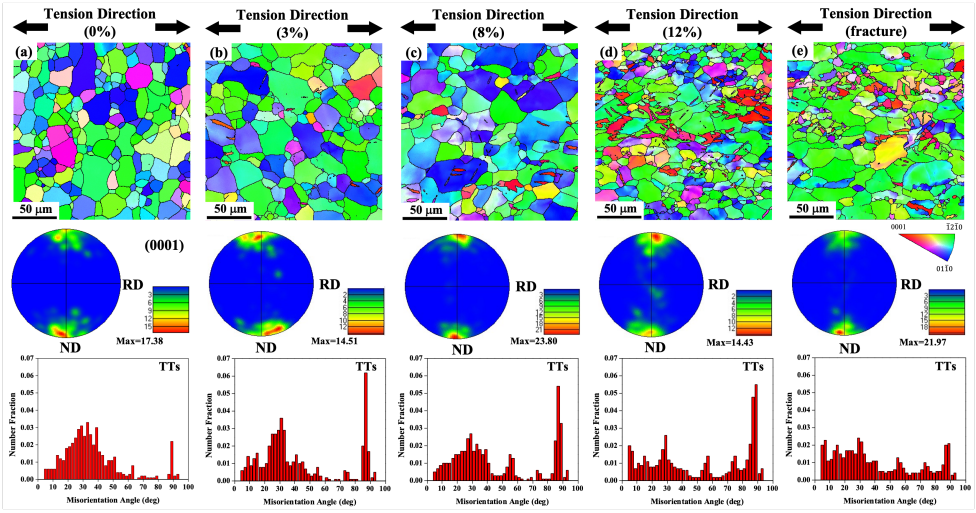

Figure 4.6: Out-of-plane IPF maps, the corresponding (0001) pole figures, highest mud values, and misorientation angle distribution histograms of AZ31 at (a) undeformed stage, (b) 3% strain, (c) 8% strain, (d) 12% strain and (e) fracture under RD tension. Some tension twins (TTs) were noted.

To assess which slip system is more likely to be activated in the rolling direction tension, Schmid fators of four major slip systems (basal $< a >$, prismatic $< a >$, and pyramidal I and II $< c + a >$) were calculated for individual grains based on the loading direction and the IPF maps in Figures 4.5a and 4.6a. As provided in Figure 4.7, the prismatic $< a >$ and pyramidal $< c + a >$ slip systems statistically have much higher Schmid factors compared to basal $< a >$ (Figure 4.7). Thus, despite their relatively higher CRSS values, we can expect the activation of prismatic $< a >$ and pyramidal $< c + a >$ dislocations in addition to basal $< a >$ dislocations, as revealed in other observations [92].

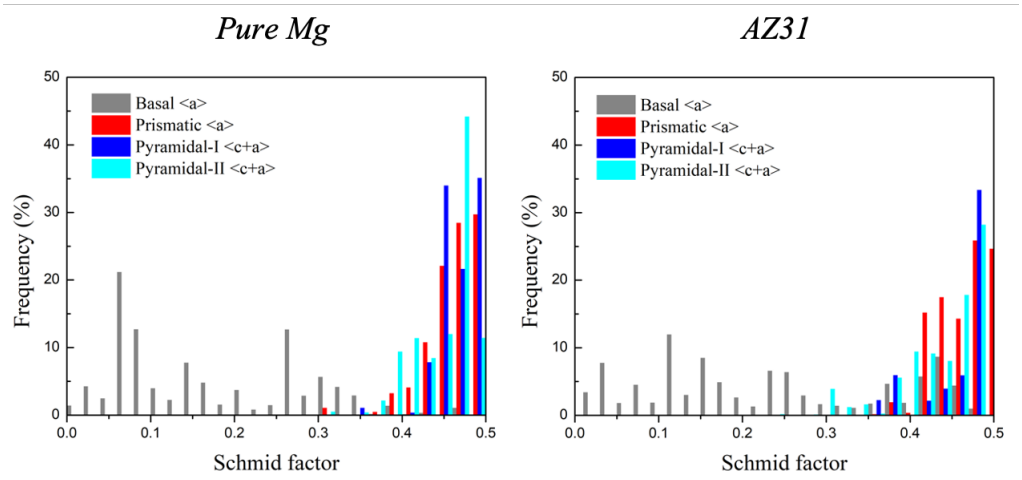

Figure 4.7: Schmid factor frequency distributions of four major slip modes (basal $< a >$, prismatic $< a >$, and pyramidal I and II $< c + a >$) calculated from the loading direction and the IPF maps in Figure 4.5a and Figure 4.6a.

4.3.4 Dislocation characteristics in pure Mg

At all strain levels, we observed the presence of non-basal $< a >$ and $< c + a >$ dislocations in almost all grains in the deformed pure Mg samples (Figure 4.8). Here we employed correlative microscopy (EBSD and TEM) to ensure the examined grains are representative of the global texture. Selected grains' 3D crystal orientations are indicated by the black arrows in the IPF maps. Considering first the $< c + a >$ dislocations, they appear under both the $[0002]$ and $[10\bar{1}0]$ weak-beam conditions, and a few examples of them are highlighted using green lines in Figures 4.8a-c. We noticed that the $< c + a >$ dislocations became active even at a low total strain of 2% (Figure 4.8a), i.e., a relatively low flow stress of ~175 MPa. The $< c + a >$ dislocation lines appear long and straight, bounded on the basal planes. In the background, numerous dim/bright dots (only a few nm in size) were also noticed, and they were reported to be small dislocation loops by Geng *et al.* [23]. The observations of $< c + a >$ dislocations and the small dislocation loops are consistent with previous studies [11, 23]. At higher strain levels (4% and fracture), significant $< c + a >$ dislocations and dislocation loops were also observed (Figure 4.8b and c). The detailed statistics of the number of grains investigated and the number of grains containing $< c + a >$ disloca-

tions at each strain level are summarized in Table 4.1, confirming the operation of the $< c + a >$ dislocations is a general observation.

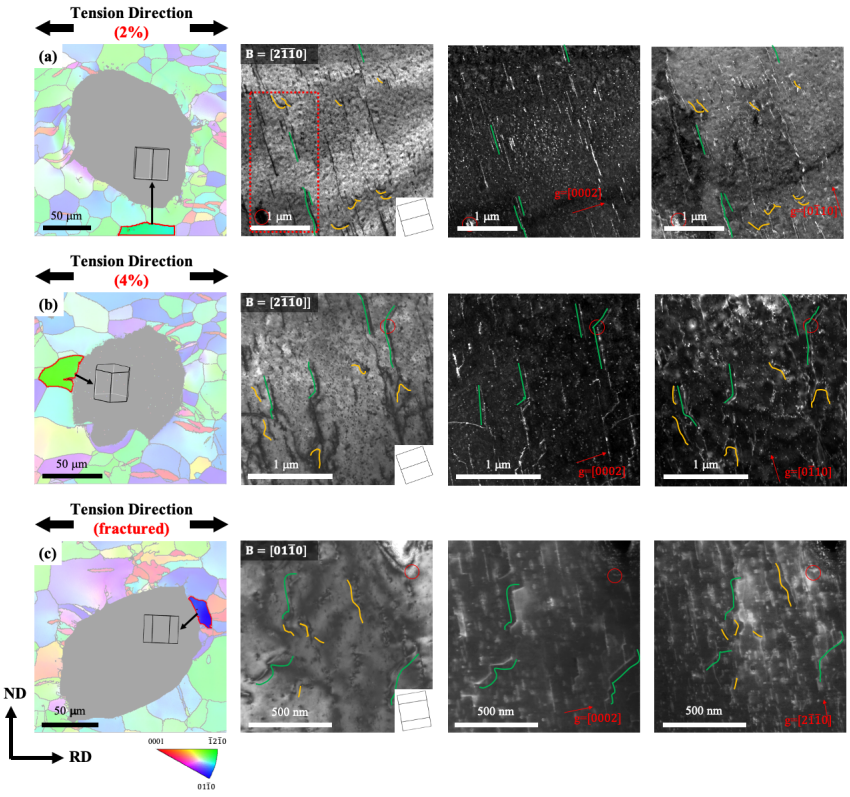

Figure 4.8: Zone axis BF and WBDF micrographs (using $\mathbf{g} = [0002]$ and $\mathbf{g} = [01\bar{1}2]$ or $[2\bar{1}\bar{1}0]$) revealing the $< c >$, $< a >$, and $< c + a >$ dislocations in pure Mg at (a) 2% strain, (b) 4% strain and (c) fracture under RD tension. The IPF maps, where the grains were taken from the electropolished TEM foil, are shown in the first column. TEM micrographs were taken from the unshaded grains. A few examples of non-basal $< a >$ dislocations (orange lines) and $< c + a >$ dislocations (green lines) are highlighted. Red circles are the fiducial markers, indicating the identical sites. The 3D models show the orientations of the imaged grains.

Grain statistics	Strain						
	Pure Mg			AZ31			
	2%	4%	Fracture	3%	8%	12%	Fracture
No. of grains examined	15	20	11	18	8	9	19
No. of grains with <c + a>dislocations	13	15	10	1	0	1	0

Table 4.1: Statistics of $< c + a >$ dislocation activation in pure Mg and AZ31.

With regards to the non-basal $< a >$ dislocations, they are only visible under $\mathbf{g} = [01\bar{1}0]$ or $[2\bar{1}10]$] conditions along with their basal counterparts. To discern them from those basal $< a >$ dislocations, we tilted the crystals to the $[21\bar{1}0]$ zone axis, where basal planes are parallel to the beam direction (second column in Figure 4.8) [7]. In this imaging condition, basal $< a >$ dislocations would appear straight as basal planes are edge on; curved dislocations could be identified as non-basal $< a >$ dislocations without ambiguity (orange lines as a few examples). In addition, we also observed a number of out-of-basal dislocation lines with only $< c >$ component. Interestingly, they were absent in the 2% strain sample but appeared only in the high-strain samples.

To further study the $< c + a >$ dislocation dissociation behavior on the basal plane [11, 9, 3], careful tilting experiments were performed while maintaining the $\mathbf{g} = [10\bar{1}0]$ WBDF condition (an example see Figure 4.9, taken from the red dashed box region in Figure 4.8a). We first took the zone axis BF micrograph ($\mathbf{B} = [2\bar{1}\bar{1}0]$) as the benchmark. Many dislocations appear long, straight, and basal bound in this projection. They have been confirmed to be $< c + a >$ dislocations via the $\mathbf{g} \cdot \mathbf{b}$ analysis (two examples are indicated by the yellow arrows in Figure 4.8a). As the basal plane is tilted towards the viewing direction, as shown by the HCP crystal schematics, the apparent $< c + a >$ dislocation dissociation was revealed, where the green lines trace the partial dislocations; the white dashed lines mark the intersection of the stacking faults with the TEM foil

surfaces. Comparing with the ND compression activated $< c + a >$ dislocation dissociation in hot-rolled and c-axis single crystal pure Mg [11, 9, 3], we noticed the $< c + a >$ dislocation cores are less spread out in the RD tension samples. The effect of different stress states on the $< c + a >$ dislocation core spreading will be discussed later.

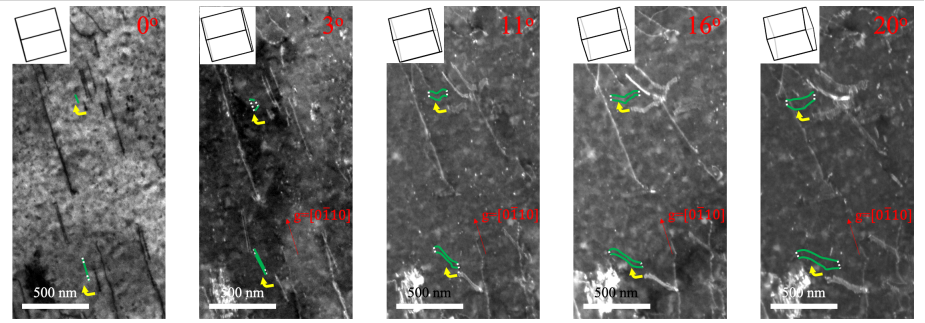

Figure 4.9: WBDF produced a series of TEM micrographs (imaged in the red boxed region in Figure 8a) in which the foil was tilted away from the $[2\bar{1}\bar{1}0]$ zone axis while maintaining the $\mathbf{g} = [01\bar{1}0]$. The zone axis BF image (0°) serves as a reference. The angles and inset schematics illustrate how far the crystal was tilted away from the zone axis. Two examples are highlighted by the yellow arrows with green lines marking the partial dislocations and white dashed lines marking the intersection of stacking fault and foil surfaces.

4.3.5 Dislocation characteristics in AZ31

For the deformed AZ31 samples, the dislocation characters were identified by the same imaging technique (Figure 4.10). Since AZ31 exhibits much better ductility than pure Mg, a different set of strain values were selected. In response to the plastic deformation, high-density dislocations were observed in all grains. We noticed, in contrast to the $< c + a >$ dislocations in pure Mg, most dislocations here display a less well-defined morphology. They were illuminated in the $\mathbf{g} = [10\bar{1}0]$ condition, but invisible in the $\mathbf{g} = [0002]$ condition, indicating they are pure $< a >$ dislocations. The absence of $< c + a >$ dislocations is not limited to the small strain samples. Rather, this observation is consistent throughout all deformation stages (Figure 4.10c-d). Again, edge-on imaging of the $[2\bar{1}\bar{1}0]$ zone axis enables the unambiguous determination of non-basal $< a >$ dislocations

(second column in Figure 4.10) We noticed at least half $< a >$ dislocations are curved at all strain levels in this projection, indicating they glide on non-basal planes. The detailed statistics of the number of grains investigated and the number of grains containing $< c + a >$ dislocations at each strain level are summarized in Table 4.1, confirming the prevalence of non-basal $< a >$ and the lack of $< c + a >$ dislocations is a general observation.

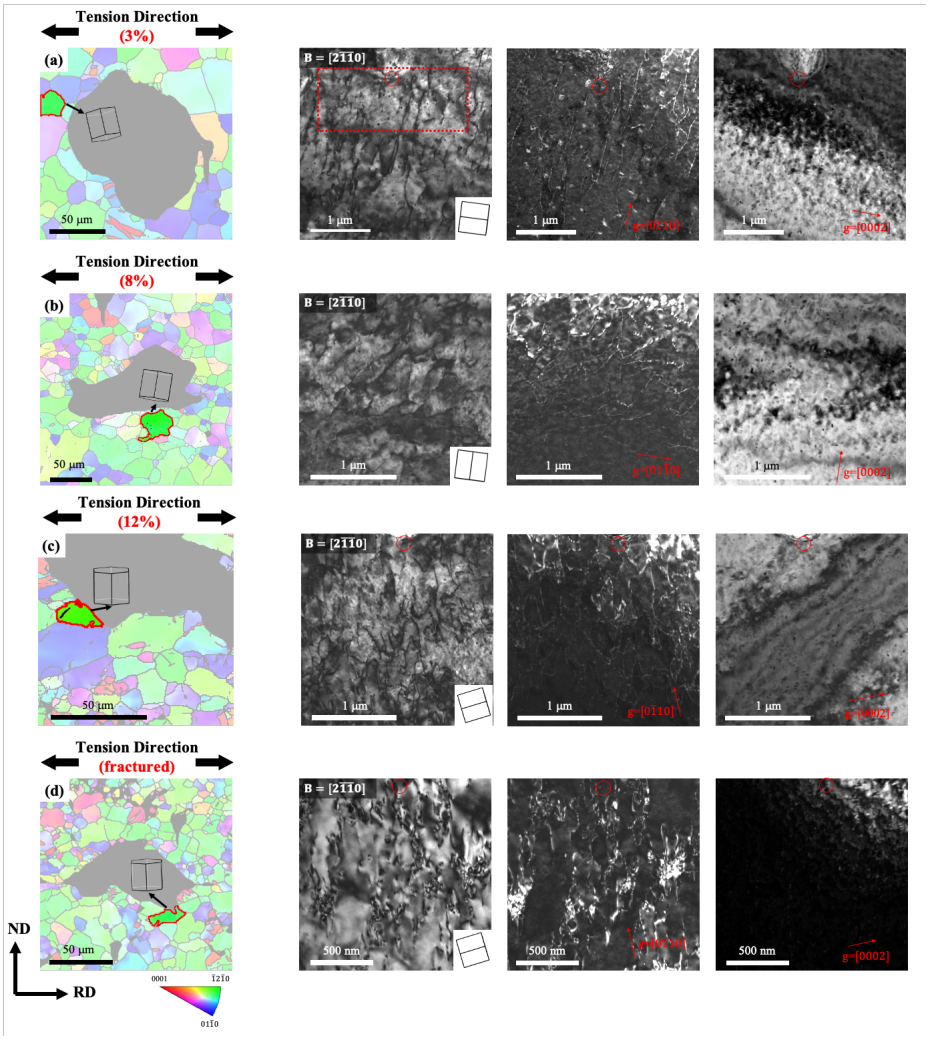

Figure 4.10: Zone axis BF and WBDF micrographs (using $\mathbf{g} = [0002]$ and $\mathbf{g} = [10\bar{1}0]$) revealing the $< c >$, $< a >$, and $< c + a >$ dislocations in AZ31 (a) 3% strain, (b) 8% strain, (c) 12% strain and (d) fracture under RD tension. The IPF maps, where the grains were taken from the electropolished TEM foil, are shown in the first column. TEM micrographs were taken from the unshaded grains. Red circles are the fiducial markers, indicating the identical sites. The 3D models show the orientations of the imaged grains.

To assess the slip planes of the non-basal $< a >$ dislocations, we prepared the AZ31 TEM foils (strained to 3%) normal to the ND direction (Figure 4.11a). In this orientation, most grains exhibit the basal texture, and slight tilting would bring grains to the $[0001]$ zone axis. The highlighted grain in Figure 4.11a was imaged using PED along the $[0001]$ zone axis to remove the dynamical effects (Figure 4.11b) [88]. PED dislocation imaging in such orientation renders the prismatic planes parallel to the incident electron beam direction. Thus, prismatic dislocations will project as straight lines in the micrograph. As shown in Figure 4.11b, numerous dislocations are presented, and they should be $< a >$ type dislocations based on the previous $\mathbf{g} \cdot \mathbf{b}$ analysis (Figure 4.10). We noticed many dislocations have straight segments parallel to multiple intersections of basal and prismatic planes (see the hexagonal insets). These dislocations are likely to be confined in prismatic planes, suggesting they are prismatic $< a >$ dislocations.

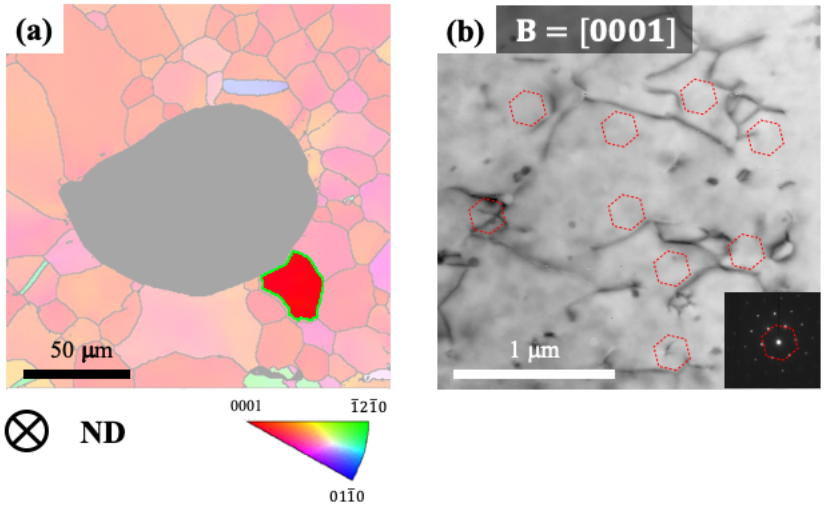

Figure 4.11: (a) IPF map of a TEM foil prepared from the ND plane in the 3% strained AZ31. (b) $[0001]$ zone axis PED micrograph of the unshaded grain reveals the dislocation morphology on the basal plane. The crystal models (highlighted by the dashed hexagons from the diffraction pattern inset) were drawn to identify dislocation slip planes.

4.4 Discussion

Based on our results, there is a significant disparity of shear banding, twinning, and non-basal dislocation activities in pure Mg and AZ31 under RD tension. Visual inspections and the OMs (Figure 4.3) revealed apparent shear banding in pure Mg but not in AZ31. Since shear bands are associated with plastic instability and local softening, they would provide an easy path for crack propagation. The presence of apparent shear bands in pure Mg could be directly linked to the low ductility and cleavage-like fracture in the pure Mg. In contrast, no apparent shear banding was noted in the deformed AZ31 at the early stage of deformation (e.g., up to $\sim$5% strain). The profuse dimples on the fracture surface also indicated ductile fracture in AZ31. Moreover, more TTs were observed in pure Mg than in AZ31. Twin-twin interactions and twin-grain boundary interactions could lead to stress concentration, triggering crack opening and harming ductility. More frequent twinning in pure Mg (although not the dominant deformation mechanism) could also be responsible for the lower ductility.

We realize the differences in shear banding, twinning, and ductility in pure Mg and AZ31 could be explained by the disparity in the non-basal dislocation activities. In the following sections, we will detail the activation of specific non-basal dislocations in pure Mg and AZ31 by discussing the following questions. (1) Why $< c + a >$ dislocations were activated only in pure Mg but not in AZ31? (2) Why non-basal $< a >$ dislocations were activated in both pure Mg and AZ31? (3) How to use the dislocation information to explain the disparities in shear banding, twinning, and tensile ductility?

4.4.1 The behavior of $< c + a >$ dislocations

From TEM investigation, we observed pyramidal $< c + a >$ dislocations were only prevalent in pure Mg but not in AZ31 (Figures 4.8 and 4.10 and Table 4.1). Here, we constructed a simple model (Figure 4.12) and used the Schmid factor analysis to explain the experimental observations. In the model, the prismatic, pyramidal I, and pyramidal II planes are shaded in red, blue, and green, respectively. To calculate Schmid factors, we considered three separate loading scenarios

	Prismatic <a>	*Pyramidal <a>*	*Pyramidal I <c + a>*	*Pyramidal II <c + a>*
SF(F1)	0.43	0.38	0.38	0.44
SF(F2)	0.50	0.44	0.44	0.42
SF(F3)	0.43	0.38	0.38	0.33
Average	0.45	0.40	0.40	0.40

Table 4.2: Schmid factors (SFs) of non-basal dislocations (prismatic $< a >$, pyramidal $< a >$, and pyramidal I and II $< c + a >$ dislocations) under three loading directions (Figure 4.12). The average values of the SFs from three loading directions are also provided.

with loading directions along the $[11\bar{2}0]$ (F_1), $[21\bar{3}0]$ (F_2), or $[10\bar{1}0]$ (F_3) directions (schematics see Figure 4.12). The $[21\bar{3}0]$ direction bisects the angle between $[11\bar{2}0]$ and $[10\bar{1}0]$. The calculated Schmid factors are summarized in Table 4.2. To estimate the CRSS from each slip system, the Schmid factors were averaged from these three loading directions.

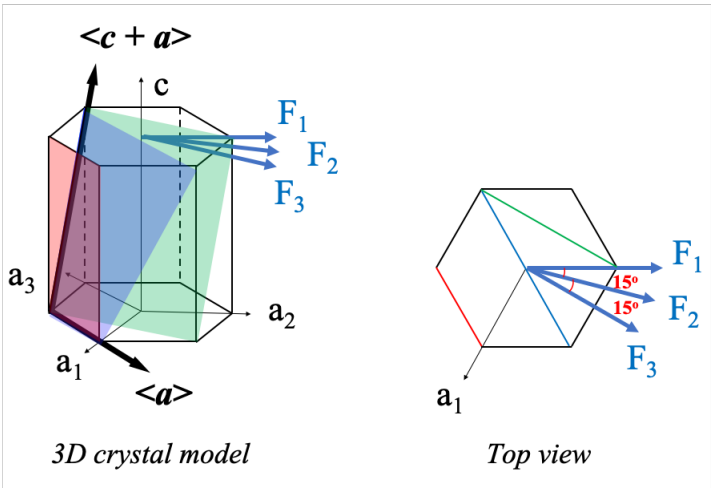

Figure 4.12: 3D and top-view projection of the HCP crystal model showing a prismatic (red), a pyramidal I (blue), and a pyramidal II (green) planes. The applied loading directions (blue arrows) are along the $[11\bar{2}0]$ (F_1), $[21\bar{3}0]$ (F_2), and $[10\bar{1}0]$ (F_3) directions.

Applying this method, we investigated the pyramidal $< c + a >$ activities in Mg and AZ31. The average Schmid factors for both pyramidal planes are 0.4, indicating a high propensity for $< c + a >$ slip. From the TEM micrographs in Figure 4.8, profuse $< c + a >$ dislocations were

observed in pure Mg. The CRSS of pyramidal $< c + a >$ slip measures ∼30-54 MPa in pure bulk Mg single crystals [17, 7, 93, 25, 22]. Combined with the average Schmid factor of 0.4, the critical applied stress to activate $< c + a >$ dislocations should be in the range of 75-135MPa. As the stress values are ∼75-200 MPa in the plastic regime, it is not surprising to observe $< c + a >$ dislocations in pure Mg. Even at a relatively small strain of 2%, the stress has already reached 175 MPa - large enough to activate $< c + a >$ slip. For AZ31, the CRSS of pyramidal $< c + a >$ is in the range of 90-120 MPa [94, 44, 95, 96]. With the average Schmid factor of 0.4, at least 230-300 MPa is required to activate $< c + a >$ dislocations. However, the measured stress level is in the range of 175-270 MPa in the plastic regime from the stress and strain curves. Most values are below the required stress level to operate $< c + a >$ slip. Even the ultimate tensile strength (270 MPa) is at the borderline of $< c+a >$ dislocation activation, which may not reach the critical values to trigger prevalent $< c + a >$ activities. This elucidates why $< c + a >$ dislocations were observed in pure Mg but not in AZ31 samples stretched along the RD.

One peculiar observation is that $< c + a >$ dislocation dissociation distance seems to be much smaller than it has been reported in the literature [11, 3]. $< c + a >$ dislocations undergo an immobile transition with a basal bound morphology [10]. The $< c + a >$ dislocations then could dissociate on the basal plane, resulting in stacking faults bounded by partials [26, 11, 9, 3]. In this study, the dissociation distance (the width of the stacking faults) was measured to only ∼35 nm. This is much shorter than the ones obtained from the ND compression samples (∼500 nm), as shown in Figure 4.13 [11, 3]. The smaller dissociation distance in the tension samples (Figure 4.9) could be explained by the normal stress acting on the dislocation core. In both ND compression and RD tension, the c-axis of Mg crystals are subjected to normal compressive stress. For the ND compression samples, the crystals experience all the imposed compressive stress along the c-axis. In contrast, the compressive stress along the c-axis from RD tension is due to the Poisson effect. Only a fraction of the tensile stress is converted to compressive stress (Poisson's ratio of Mg is ∼0.3). It is thus reasonable to attribute the $< c + a >$ dislocation dissociation distance to the elastic component of the normal stresses. Larger compressive normal stress leads to larger

dissociation. This conjecture is supported by the prediction of Wu and Curtin [10]. The authors demonstrated a small compressive stress (such as RD tension in this study) raises the energy barrier for $< c + a >$ dislocation dissociation, thus leads to narrower stacking faults.

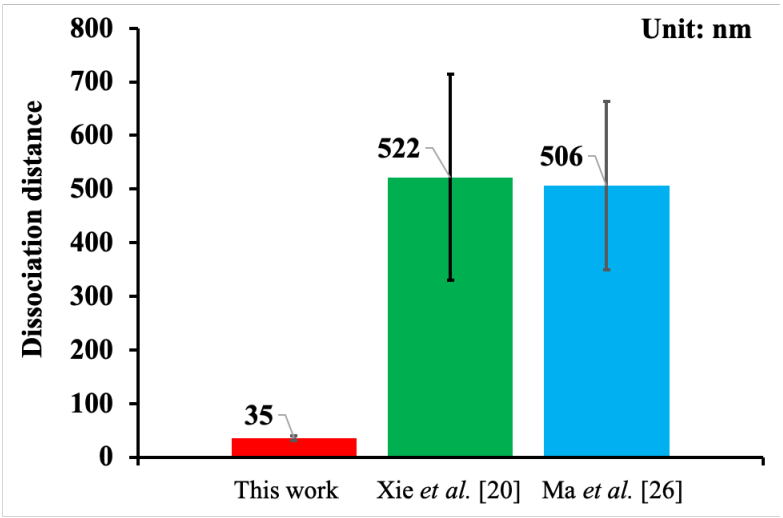

Figure 4.13: Histogram showing the $< c + a >$ dislocations dissociation distance (the width of the stacking faults) for this work under RD tension ($\sim$35 nm) and previous work under the ND compression ($\sim$500 nm).

We also notice a number of pure $< c >$ dislocations are present in pure Mg at a relatively large strain (e.g. 4%). They may be remnants of dislocation decomposition from $< c+a >$ dislocations [26, 11] that have undergone cross-slip [42]. Note that the $< c >$ dislocations were not widely observed in samples with a lower strain (see Figure 4.14a). At 2% strain, the c-components (from $< c+a >$ dislocations, illuminated by the $[0002]$ **g**-vector) are largely basal bound, indicating very limited cross slip of $< c + a >$ dislocations. At a high strain value of 4%, many c-components that are not basal-bound were observed (Figure 4.14b-c). Using the in situ nanopillar compression technique, Liu *et al.* observed the "basal-bound" $< c + a >$ dislocations (possibly undissociated edge or near-edge component) could glide via cross slip of the screw component if the stress is sufficiently high [42]. Combining this knowledge with our experimental observations, we propose a model that depicts the $< c + a >$ dislocation motion in pure Mg (Figure 4.15). Assuming

the $< c + a >$ dislocation (green line in Figure 4.15a) initially glide on the pyramidal II plane. The $< c + a >$ dislocation could cross slip on to the pyramidal I plane along the intersection of pyramidal II and pyramidal I planes (Figure 4.15b). The edge (or near-edge) components are susceptible to pyramidal-to-basal core transformation, which may further hinder them cross slip [10, 39]. The $< c + a >$ screw component could decompose in to $< c >$ and $< a >$ dislocations, where the $< a >$ dislocation easily glides away and $< c >$ component becomes a remnant. A similar behavior could also happen in the double-slip case, where the $< c + a >$ dislocation cross slips from pyramidal II to pyramidal I, then back to pyramidal II plane (Figure 4.15c). Both the dislocation core transformation and the dislocation decomposition consume the glissile $< c + a >$ dislocations, rendering $< c + a >$ dislocation poor carriers to accommodate plastic deformation.

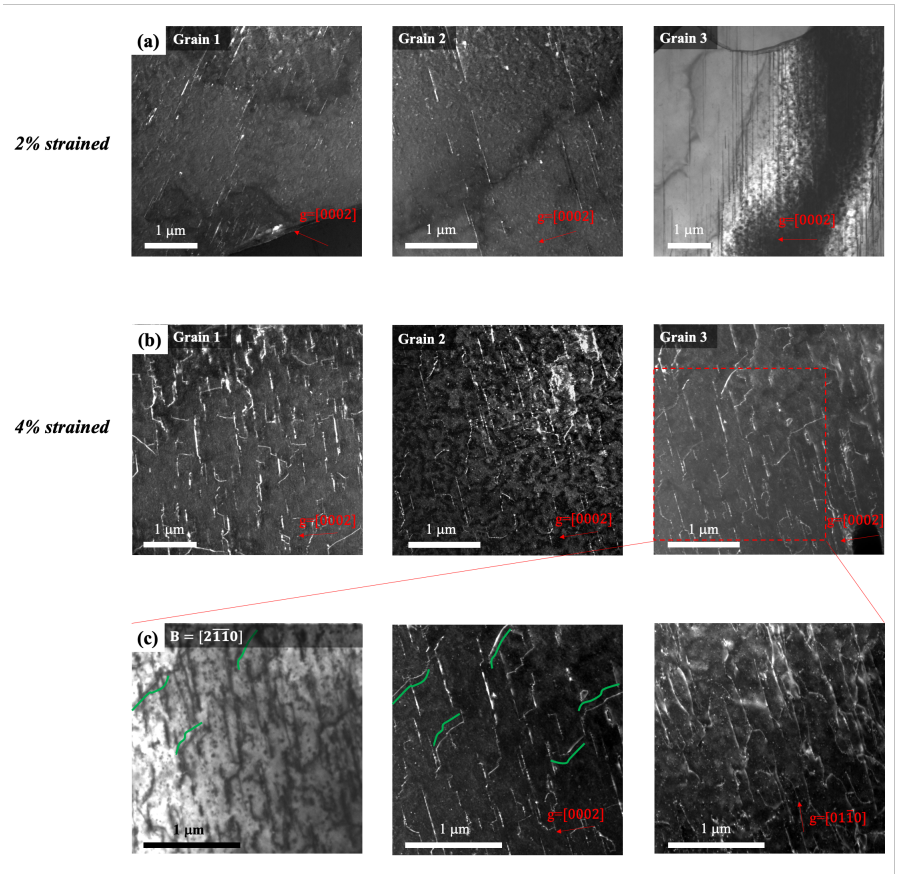

Figure 4.14: WBDF and two-beam BF images showing the $< c >$ components using $\mathbf{g} = [0002]$ at (a) 2% and (b) 4% strains in various grains. (c) The detailed $\mathbf{g} \cdot \mathbf{b}$ analysis confirms most curved c-components (green lines) are pure $< c >$ dislocations.

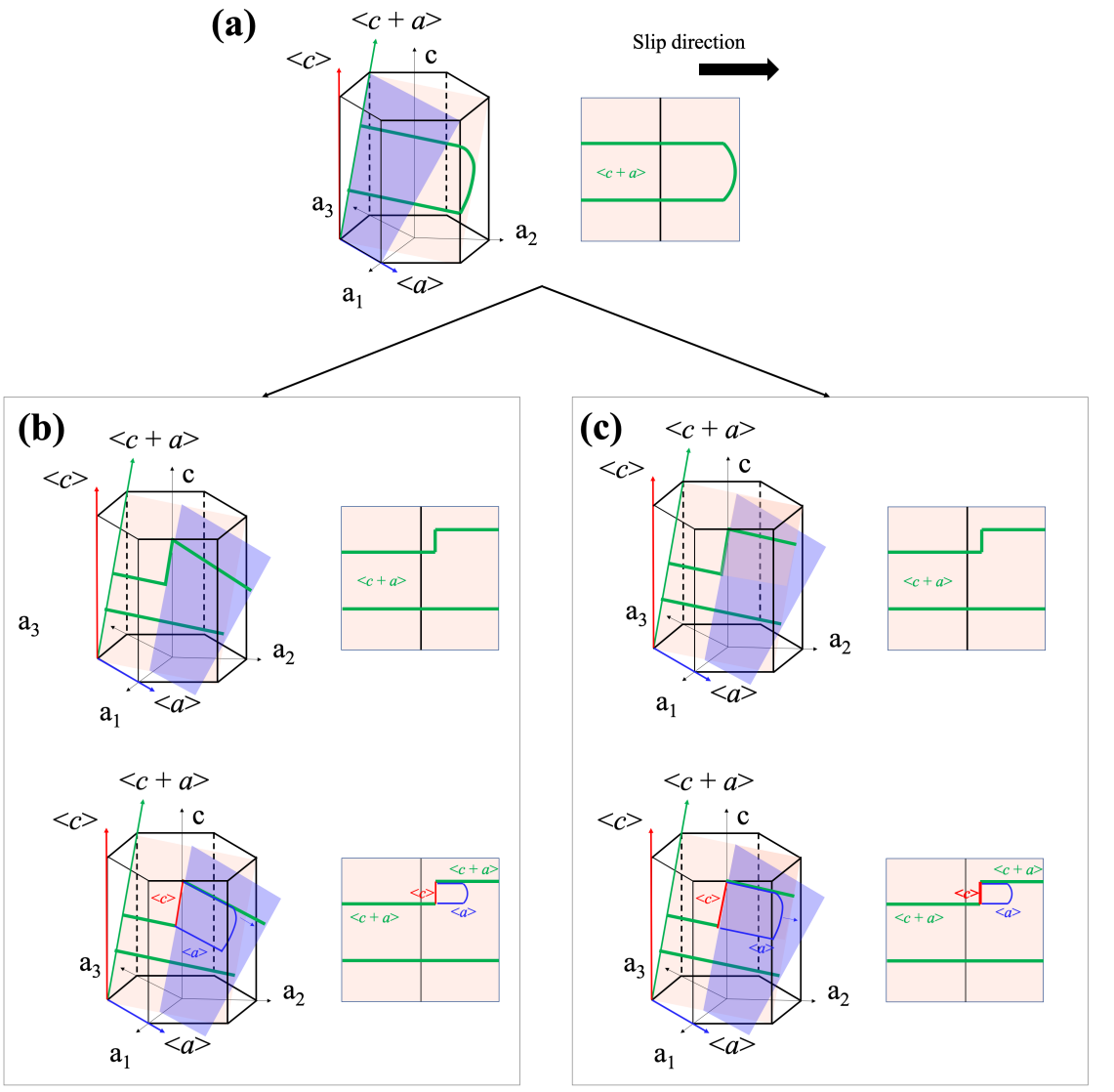

The screw component cross slips from pyramidal II to pyramidal I.

The screw component cross slips from pyramidal II to pyramidal I then back to pyramidal II.

Figure 4.15: 3D HCP crystal models and projected views (along a1) depicting $< c+a >$ dislocation movement in pure Mg at (a) low and (b-c) high stress levels. The $< a >$, $< c >$, and $< c + a >$ dislocation lines and burger vectors are labeled by red, blue and green lines and arrows, respectively. The pyramidal I and II planes are shaded in orange and light blue.

4.4.2 The behavior of non-basal $< a >$ dislocations

The Schmid factor analysis was also applied to understand the non-basal $< a >$ dislocation activities in pure Mg and AZ31. For prismatic $< a >$ slip, the CRSS in pure Mg ranges from 30 to

50 MPa [19, 20, 70, 71]; the average Schmid factor is 0.45. The applied stress to activate prismatic $< a >$ dislocation is estimated to be 70 to 110 MPa. This value is less than the post-yielding stress in pure Mg (75-200 MPa). Thus, prismatic $< a >$ dislocation activation is expected and also observed. In the case of AZ31, The CRSS for prismatic $< a >$ dislocation is reported to be 50-100 MPa [44, 47]. Combing the CRSS with the average Schmid factor of 0.45, the prismatic $< a >$ activation stress should be 110-220 MPa. This falls in the range of the yield strength (173 MPa) to the ultimate tensile strength (277 MPa) of AZ31. Thus, the activation of prismatic $< a >$ is also expected and observed (example, see Figure 4.11).

We were not able to predict the pyramidal $< a >$ dislocation activities for pure Mg and AZ31 using the Schmid factor analysis because of the lack of their CRSS values in literature. Nonetheless, we did observe the pyramidal $< a >$ dislocations based on the TEM results in AZ31. There are some suggestive evidence of pyramidal $< a >$ dislocations reported back in the 1960s [21, 97, 98]. To confirm their presence, we imaged pyramidal $< a >$ dislocations along the $[2\overline{1}\overline{1}0]$ zone axis. In this orientation, one-third of pyramidal $< a >$ dislocations would lie on the intersection of the pyramidal I plane (blue) and the prismatic II plane (green), as shown in the crystal models (Figure 4.16a-b). The BF TEM image (Figure 4.16c) was taken from the boxed region in Figure 4.10a, which confirms all the dislocations in this area are of $< a >$ type. In this area, two straight segments are noted. Overlaying the model from Figure 4.16a-b to the TEM image, we observed the dislocations parallel to the intersection of pyramidal I and prismatic planes. These dislocations are likely to be pyramidal $< a >$ dislocations in the deformed AZ31 samples. Their presence suggests they were activated during deformation. In contrast, pyramidal $< a >$ dislocations in pure Mg seem to be less frequent compared to that AZ31, probably suggesting a lesser role in accommodating plasticity.

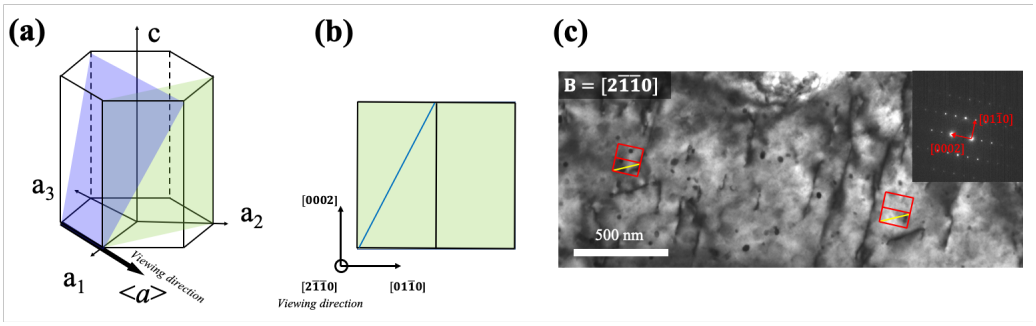

Figure 4.16: (a) 3D HCP crystal model and (b) projected view (along a_1) models showing the pyramidal I $< a >$ slip plane (blue) and burger vector. (c) BF TEM micrograph imaged from the boxed region in Figure 4.10a. Two possible examples of pyramidal $< a >$ dislocations are suggested by the projected crystal (red boxes) and pyramidal I plane (yellow lines) from the (b) and the diffraction pattern (inset).

Here we address the three possible mechanisms we proposed in Introduction to elucidate the roles of $< c + a >$ dislocations in RD tension. Since both pure Mg and AZ31 used in this study exhibit strong texture (also similar grain size), the effect of the global texture could be precluded. In RD tension, where the loading direction is largely parallel to the basal planes of the crystals, $< c + a >$ dislocations could contribute to the plasticity, but their participation is not necessary. In the case of AZ31, the alloying elements modified the CRSS. The CRSS gap widens between $< c + a >$ and non-basal $< a >$ systems, so that non-basal $< a >$ plays a more dominant role as the plasticity carrier.

4.4.3 Explaining the differences in shear banding, twinning, and ductility using disparity in dislocation activities in pure Mg and AZ31

It is known the ductility of AZ31 is much better than that of pure Mg. Moreover, shear banding and twinning are more prevalent in pure Mg than in AZ31. The underlying mechanisms that could elucidate these differences have been unclear. Based on our TEM observations and analyses, there is a significant disparity in non-basal dislocation activities between pure Mg and AZ31. Both pyramidal $< c + a >$ and non-basal $< a >$ dislocations were active in the pure Mg. In contrast, there lacks $< c+a >$ slip in AZ31 samples, while the non-basal $< a >$ dislocations were prevalent.

The reason for the absence of $< c + a >$ in AZ31 could be attributed to the CRSS change from the Al and Zn alloying. A recent review paper by Nie *et al.* [99] showed that the 1% Al in Mg single crystal could dramatically widen the CRSS gap between pyramidal $< c+a >$ and prismatic $< a >$ dislocations (roughly from 20 MPa in pure Mg to 100 MPa in Mg-1Al). The alloying effect therefore makes it more difficult to activate the $< c + a >$ slip in AZ31.

Although $< c + a >$ dislocations can provide extra slip systems, their absence seems to be beneficial to sustain plasticity in RD tension. The $< c + a >$ dislocations could readily undergo glissile-to-sessile core transformation or decomposition [10]. Both processes result in quick exhaustion of glissile $< c + a >$ dislocations and a lack of continuous hardening mechanism to combat plastic instability. A direct result is the formation of shear bands triggered by plastic instability. Therefore, $< c + a >$ dislocations were activated in pure Mg but did not lead to a decent ductility. For the AZ31, the prismatic and pyramidal $< a >$ dislocations do not undergo core transition or dislocation decomposition. They could multiply and glide more freely to provide sustainable work hardening. The addition of Al and Zn have been reported to reduce the propensity of prismatic-to-basal cross slip [69, 81], which better retains dislocation glide on the prismatic plane. The continuous prismatic slip allows for sustainable plastic flow, which suppresses the formation of shear bands. Since crack could easily initiate from and propagate along shear bands, the suppression of shear bands in AZ31 is considered to be the primary cause for improved ductility.

We can further apply this argument to twinning. More TTs were observed in pure Mg than in AZ31. Less TTs in AZ31 could again be explained by the profuse prismatic $< a >$ dislocation activities. As suggested by Mayama *et al.* [69, 100], prismatic $< a >$ dislocation would rotate grains' a-axes to preferred orientations for further deformation. This activates less TTs. Since twin-grain boundary and twin-twin interactions could create local stress concentrations, they could act as the failure initiation sites [101, 102, 45]. Thus, suppressed TTs and consequently less stress concentration could be the secondary cause for improved ductility and delayed fracture in AZ31.

Moreover, the lack of $< c + a >$ dislocation contribution to the plasticity in AZ31 urges us to reconsider what dictates the tensile ductility when pulling Mg samples parallel to the basal plane.

In pure Mg, the tensile ductility is controlled by the interplay of $< c + a >$ and non-basal $< a >$ dislocations. The $< c + a >$ dislocations exhibit a strong self-locking behavior, resulting in quick exhaustion of strain hardening capacity, leading to shear banding, more TTs, and limited ductility. In contrast, in AZ31, the ductility is largely governed by the non-basal $< a >$ slip. The promoted non-basal $< a >$ slip and the suppressed $< c + a >$ dislocations give rise to the suppressed shear banding, less TTs, and much-improved ductility.

We can further extend this alloy design concept to other Mg alloys. To achieve improved tensile ductility, deformation mechanisms that suppress shear banding and TT should be activated. In this study, we demonstrated the promoted non-basal $< a >$, suppressed $< c + a >$ activities in AZ31 could be one of the strategies to suppress early-stage shear banding and further improved ductility. The improved ductility in Mg-Ca, Mg-Y [103, 35], and Mg-Gd may also be explained by the promoted prismatic slip compared to $< c + a >$. Indeed, X-ray and TEM observations on the tensile strained samples showed extensive non-basal $< a >$ slip and very limited $< c + a >$ activities [8, 27, 32, 103, 35, 33, 34]. This again emphasizes the roles of non-basal $< a >$ slip on the improved ductility of Mg alloys. We noticed most previous dislocation work in Mg has focused on $< c + a >$ dislocations, while the non-basal ones remain less explored [20, 70, 104]. In this work, we offer new insight into the effect of alloying elements on the non-basal $< a >$ dislocation activities. Further studies in this area (e.g., CRSS, Peierls stress, mobility, core structure of non-basal $< a >$) could generate plenty of new opportunities to advance the understanding of the deformation behavior of Mg and guide the design of Mg alloys with excellent ductility.

4.5 Conclusions

In this work, we performed detailed TEM characterization and analyzed the deformation behavior of pure Mg and AZ31 subjected to RD tension. The improved ductility in AZ31 could be attributed to the suppressed shear banding and less TTs as a result of the promoted non-basal $< a >$ dislocation slip. The key findings of this study can be summarized as follows:

1. AZ31 displays much better ductility than pure Mg (13% and 5%, respectively) when the tensile loading direction is mostly parallel to the basal planes of the grains (along RD). Apparent

shear banding and more TTs were observed pure Mg. No apparent shear banding and less TTs were observed AZ31.

2. Both $< c + a >$ and non-basal $< a >$ slip systems were activated in pure Mg under tension along RD. The $< c + a >$ dislocations were activated since the early stage of plastic deformation. The $< c + a >$ dislocations display less spread-out cores than those from c-axis compression, indicating the normal elastic stress plays a significant role in core spreading. Moreover, increasing strain level appears to promote the cross slip of $< c + a >$ dislocations.

3. Non-basal $< a >$ slip system, rather than $< c + a >$ slip, was predominant in the AZ31 under tension along RD. No significant $< c + a >$ activities were observed even in the fractured samples. For the non-basal $< a >$ dislocations, we noticed both prismatic $< a >$ and pyramidal $< a >$ are activated.

4. The improved ductility in AZ31 could be explained by the suppression of shear bands (primary) and less TTs (secondary) as a result of the promoted non-basal $< a >$ slip. Unlike $< c + a >$ dislocations, non-basal $< a >$ dislocations do not exhibit the self-locking behavior. Thus, they could offer sustainable hardening during deformation and delay failure.

5. ON THE EXCEPTIONALLY HIGH DUCTILITY OF MG-2ZN-0.3CA-0.2CE-0.1MN ALLOY[1]

5.1 Introduction

Magnesium (Mg), as the lightest practical structural metal, has attracted extensive interest in automotive and aerospace applications [105, 99, 106, 107, 108, 109]. However, pure Mg and most Mg alloys exhibit low room temperature (RT) formability and ductility, which restrict their wider usage in wrought applications [110, 111]. This is mainly due to the ease of basal slip, difficulty to activate other slip systems and the strong texture after wrought processing. Thus, promoting non-basal slip modes (e.g., $< c + a >$ slip) and weakening the texture are important to overcome the low RT formability and ductility challenge.

Alloying, including Al, Zn, Ca, and rare earth (RE) elements, is one key method to achieve more ductile and formable Mg at RT [76, 112]. For non-RE-bearing Mg alloys, the Mg-Al family has the largest commercial applications [99], with Mg-3Al-1Zn (AZ31) alloy [8, 113, 114] being the most prominent example. Many experimental works indicated that Al and Zn alloying could significantly improve ductility [111, 76, 8, 37, 30, 81, 3]. Our recent study [62] revealed the improved ductility of the AZ31 alloy could be attributed to the promotion of non-basal $< a >$ dislocation activities and the suppression of early-stage shear banding. The addition of Ca has been shown to weaken the rolling texture after annealing, which was proposed to be related to recrystallization [115, 116, 117]. With a weak texture, more deformation modes can be activated, leading to more uniform deformation and improved ductility. For RE alloying, such as Ce, Gd and Y, weaker texture Mg alloys can also be achieved after processing to display the 'RE texture' [118, 38, 119, 120]. In addition to the weakened texture, Sandlobe *et al.* [38, 28, 32] pointed out the increased ductility of Mg-Y is also a result of the increased $< c + a >$ dislocation activities from their transmission electron microscopy (TEM) observations. Using molecular dynamics sim-

[1]Reprinted with permission from "On the exceptionally high ductility of Mg–2Zn-0.3Ca-0.2Ce-0.1Mn alloy" by Dexin Zhao, Renhai Shi, Peter Evans, Alan A Luo, Kelvin Y Xie. Materials Science and Engineering: A, p.141484. Copyright (2021).

ulations, Wu *et al.* [27] also showed the RE alloying could suppress $< c + a >$ dislocation from dissociating on the basal plane and promoted the cross slip.

Recently, a new Mg alloy was designed with the composition of Mg-2Zn-0.3Ca-0.2Ce-0.1Mn (ZXEM2000) by Shi *et al.* [6]. The ZXEM2000 alloy exhibits an excellent combination of strength and ductility (154 MPa yield strength, 29% strain to failure). However, the fundamental mechanisms that elucidate the exceptionally high ductility are still not clear. In this work, we performed tensile tests on the ZXEM2000 alloy along the rolling direction at different strain levels. Scanning electron microscopy (SEM) and TEM were then carried out to understand the improved ductility at the granular and dislocation levels.

5.2 Materials and Methods

ZXEM2000 alloy was prepared in a steel crucible under a protective gas, using pure Mg, pure Zn, Mg-25%Ca, Mg-28.4%Ce, Mg-10%Mn and cast into a steel mold at 750 °C to produce 110 × 114 × 18 nm plates. The 20 × 28 × 7 mm samples cut from the plates were then homogenized with multi-stage heat treatment to dissolve all the intermetallic phase. The homogenized samples were then rolled at room temperature initially to ∼3 mm with about 0.25 mm-0.5 mm per pass and subsequently ∼1 mm with 25%-30% thickness reduction per pass. After the rolling, the alloy sheet was annealed at 350 °C for 20 min to remove most of the pre-existed dislocations. For details, please refer to Figure A.7 and Shi *et al.* [6]. As-cast 99.9% pure Mg purchase from US Magnesium was rolled into 10 mm sheet at 160 °C (1 pass 20%, 8 passes 10% with 64% total reduction) to produce highly texture. Hot-rolled AZ31 sheets purchased from MetalMart International Inc. were also selected for this study. The pure Mg and AZ31 bulk samples were annealed at 350 °C for 12 hours under Argon flow atmosphere to homogenize the microstructure. Dog-bone tensile specimens with 8 mm gauge length, 3 mm gauge width and 1.5 mm gauge thickness were then cut from above ZXEM2000 alloy, AZ31 alloy and pure Mg, using an electrical discharge machine (EDM) along the rolling direction. Uniaxial tensile tests were then conducted on an MTS test machine at a strain rate of 5×10^{-4} s^{-1}. For ZXEM2000 alloy, the tensile tests were stopped at 5% strain and at failure, respectively, for microscopy analyses.

SEM and TEM analyses were carried out on the ZXEM2000 alloy at the initial and deformed (5% and fractured) stages. The tensile bars were mechanically polished down to the 1200 grit SiC paper then punched into 3 mm TEM discs. For the fractured samples, we performed the SEM fractography and fabricated TEM discs away from the fracture surfaces to avoid the complex stress states. These discs were then twin-jet electropolished using a Tenupol-5 polishing system with a solution of 15.9 g lithium chloride, 33.5 g magnesium perchlorate, 1500 ml methanol and 300 ml 2-butoxy-ethanol at -40 °C. Before the TEM observations, electron backscattered diffraction (EBSD) was carried out on these foils after ion milling at the liquid nitrogen temperature using a Tescan FERA SEM equipped with an EBSD detector (Oxford Instrument). TEM was carried out on an FEI Tecnai operating at 200 keV. Considering the electropolished TEM foils are in the normal plane (close to the basal plane after processing), we also performed focused ion beam (FIB, FEI Helios Nanolab 460F1) lift-out to prepare TEM lamellae close to the prismatic planes. Such specimen orientation allows for the identification of $< c + a >$ dislocations. To reveal the dislocation characters, we did the two-beam bright-field (BF) and weak beam dark-field (WBDF) imaging. For the disc TEM samples (viewing along the normal direction), the $[0001]$ zone axis was selected to image the dislocation on the basal plane. For the FIB lift-out lamellae, we used the $\mathbf{g} \cdot \mathbf{b} = 0$ invisibility criterion to illuminate $< a >$ and $< c >$ components separately, $\mathbf{g} = [0002]$ (all c-component will be visible) and $\mathbf{g} = [01\bar{1}0]$ (two-thirds of a-component will be visible). If one dislocation is visible under both $\mathbf{g} = [0002]$ and $\mathbf{g} = [01\bar{1}0]$ diffraction conditions, it is of $< c + a >$ type. For each strain level, roughly 10 grains were examined to statistically study the dislocation activities.

5.3 Experimental Results

A representative engineering stress-strain curve from the ZXEM2000 alloy pulled along the rolling direction is shown in Figure 5.1a (red), which is compared to the pure Mg (blue) and AZ31 (black) strained under the same condition [62]. The ZXEM2000 alloy (154 ± 1.4 MPa yield strength) is also stronger than pure Mg (144 ± 4 MPa yield strength) but weaker than the AZ31 alloy (173 ± 7 MPa yield strength). However, the ZXEM200 alloy exhibits a significantly better

ductility (29% ± 1.4% elongation) than pure Mg (5% ± 0.8% elongation) and AZ31 alloy (12.7% ± 1.2% elongation). Fracture surface analysis on the ZXEM2000 alloy, along with the pure Mg and AZ31 alloy [62], also indicates the improved ductility of the ZXEM2000 alloy. For the pure Mg, relatively flat facets (see the green circle for example) with fewer dimples (examples in the red circle) were observed, indicating a mixture of brittle and ductile fracture modes. In contrast, more dimples and no apparent flat facets were noted in both fractured AZ31 and ZXEM2000 alloys, indicating dominantly ductile fracture. Moreover, the fracture surface of the ZXEM2000 alloy shows a much bigger and deeper dimple than that of AZ31, which may explain the further improved ductility in the new alloy.

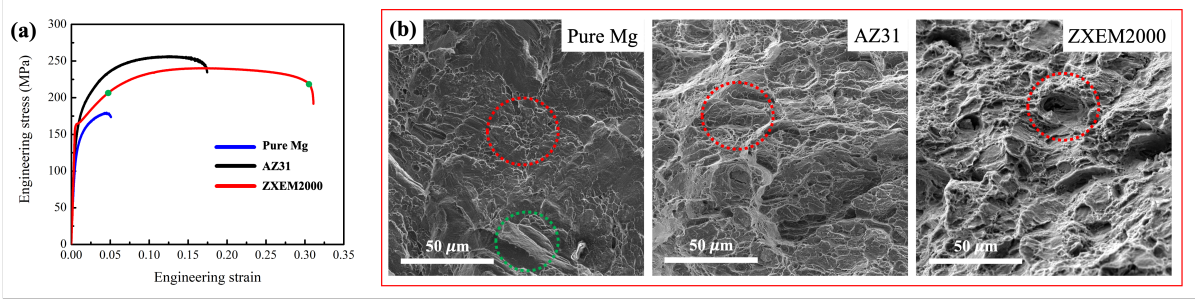

Figure 5.1: (a) Stress-strain curves of ZXEM2000 (Mg-2Zn-0.3Ca-0.2Ce-0.1Mn, red line), pure Mg (blue line) and AZ31 (Mg-3Al-Zn alloy, black line) under tension along the rolling direction. Two strain levels (5%, fractured, as shown by green dots) were selected for the microstructural characterization. (b) The SEM fractography of pure Mg, AZ31 and ZXEM2000 tensile samples. Red and green dashed circles refer to the flat facets and dimpled regions, respectively.

To uncover the detailed deformation mechanisms of ZXEM2000, EBSD and TEM examinations were performed on the TEM foils (normal plane) at the selected strain levels (initial, 5% and fractured). For the undeformed sample, the results from the global EBSD inverse pole figure (IPF) and pole figure (PF) appear to suggest the basal texture along the normal direction (Figure 5.2a) with an average grain size of 5.47 μm. However, the texture is much weaker (max intensity, 5.9) compared with pure Mg (max intensity, 16.25) and AZ31 (max intensity, 10.85) from our previous report (Figure A.5) [62]. The (0001) pole spreading from ND toward TD indicates

extensive non-basal $< a >$ slip (prismatic $< a >$). We also noted no apparent tension twins (TTs) from the misorientation angle distribution. The TEM BF image near the $[0001]$ zone axis also confirms low initial dislocation density. Thus, the initial microstructure of low TTs and dislocation density serves as a benchmark for the deformed samples. Meanwhile, we noticed the presence of precipitates, which was later confirmed as Mn concentration precipitates and Ca, Zn concentration precipitates by scanning transmission microscopy (STEM) energy dispersive spectroscopy (EDS) (Figure A.6). For the 5% strained sample (Figure 5.2b), the overall texture remained, and the microstructure is largely twin-free. Moreover, the $[0001]$ zone axis BF micrograph shows an extremely high density of dislocations. For the fractured samples (Figure 5.2c), again, no apparent TT was observed from the IPF map and misorientation angle distribution histogram. The lack of extension twins in the deformed microstructure of Mg alloys is unexpected, as noticeable TTs were observed in pure Mg and AZ31 deformed under the same loading conditions (Figure A.7) [62]. The roles of TT on the ductility in Mg will be addressed later. From the TEM image, we noticed the high-density dislocations self-organized to form a dislocation network and dislocation cells, a result of the excellent ductility. All above observations indicate dislocation slip is the primary plasticity carrier in the ZXEM2000 alloy when pulled along the rolling direction.

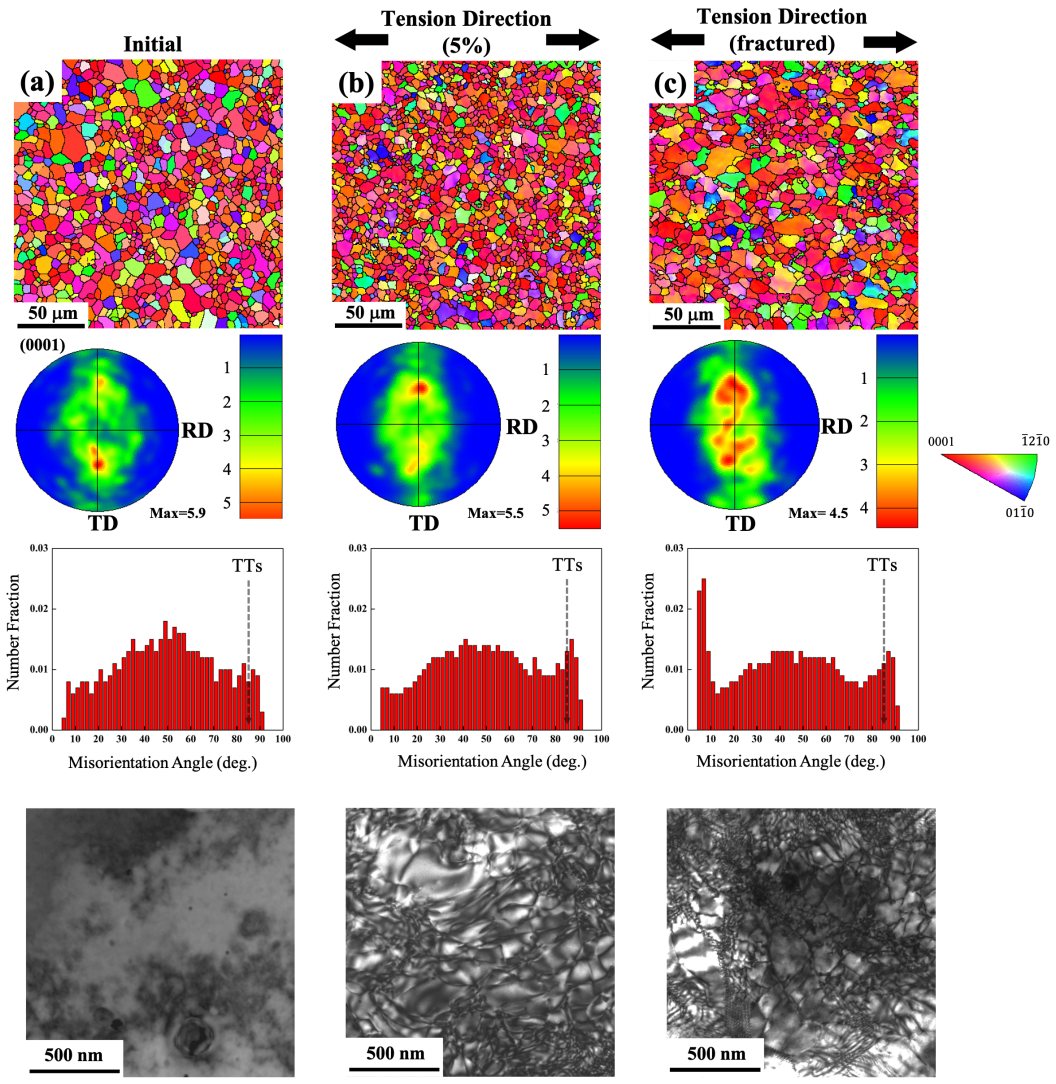

Figure 5.2: EBSD IPF maps (out-of-plane crystal orientation) of ZXEM2000 revealing the (a) initial, (b) 5% strained and (c) fractured microstructures, along with the corresponding (0001) pole figures, misorientation angle distributions, and the TEM BF micrographs close to the $[0001]$ zone axis.

To reveal the active slip modes to accommodate deformation in ZXEM2000, two-beam BF TEM was performed on the FIB lift-out lamellae (initial, 5% strained and fractured), as shown in Figure 5.3. No apparent dislocation ($< a >$ nor $< c >$ component) was observed in the initial lamella (Figure 5.3a). Hence, the dislocations observed in the strained samples (5% and

fractured) are mostly a result of the deformation. For the 5% strained sample (Figure 5.3b), high-density dislocations were illuminated under the $[01\bar{1}0]$ condition, indicating profuse basal $< a >$ and non-basal $< a >$ dislocations. Under the $[0002]$ diffraction condition, $< c >$ components were illuminated and many were confirmed as $< c + a >$ dislocations. Noted the basal planes are perpendicular to the $[0002]$**g** vector (yellow dashed line as the basal plane projection). Surprisingly, we found most of the $< c + a >$ dislocation segments are not basal-bound, which is very different from those in the pure Mg and AZ31 [3, 9, 22, 65]. Meanwhile, out of 9 grains we overserved in the FIB lamella, 5 were confirmed with $< c + a >$ dislocations (56% of the grains). The $< c + a >$ in the other grains also exhibit a similar morphology. For the fractured lift-out sample (Figure 5.3c), we found a similar dislocation behavior. Numerous dislocations with the $< a >$ components show up under $[01\bar{1}0]$ **g** vector, which makes the individual dislocation difficult to resolve. For the $< c + a >$ dislocations (under $[0002]$ **g** vector), we also observed the similar non-basal bounded morphology. Out of 10 grains we interrogated, 5 contain the $< c + a >$ dislocations (50% of the grains). The non-basal bounded morphology of $< c+a >$ dislocation in the deformed ZXEM2000 and its role on ductility will be discussed later.

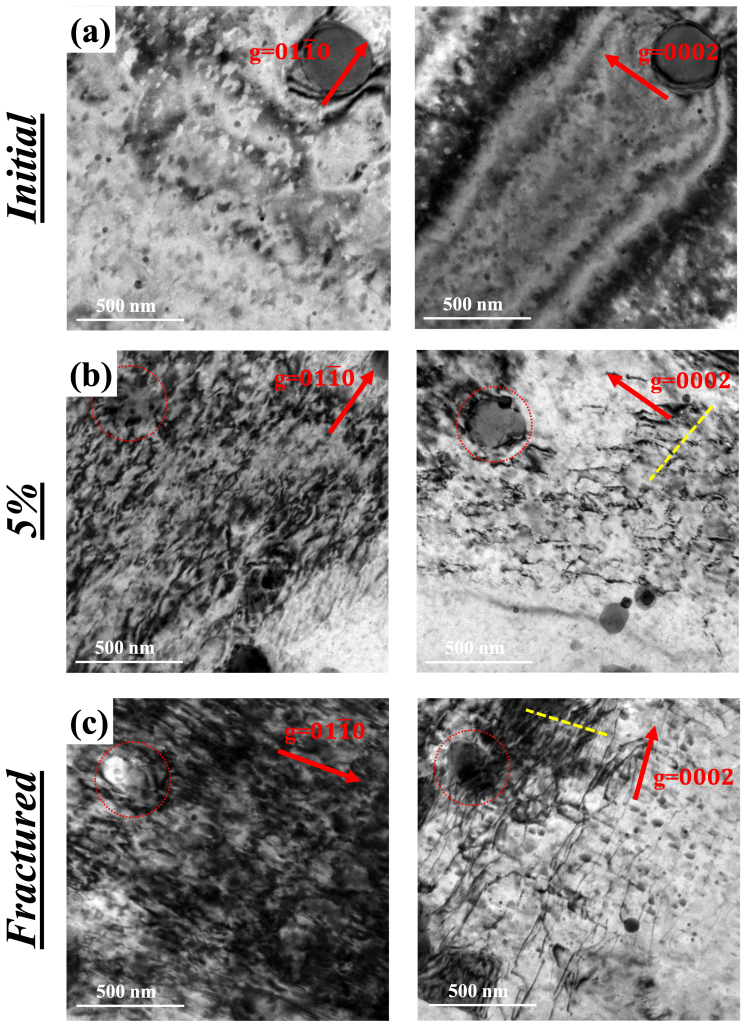

Figure 5.3: TEM BF micrographs (using $\mathbf{g} = [0002]$ and $\mathbf{g} = [01\bar{1}0]$) revealing $< c >$, $< a >$, and $< c + a >$ dislocations in the ZXEM2000 FIB lamellae at the (a) initial, (b) 5% strained, and (c) fractured conditions. Red circles are the fiducial markers, indicating the identical sites. Yellow dashed line perpendicular to the $[0002]$ **g** vector corresponds to the projection of basal planes.

5.4 Discussion

Here, we attempt to uncover the fundamental mechanisms that result in the much-improved ductility (29%) in the newly developed ZXEM2000 alloy compared to pure Mg and AZ31. Based on the above SEM and TEM observations, we suggest four key factors contribute to the more sustainable plastic deformation.

First, the weaker texture could lead to the improved ductility. As shown in Figure 5.2, the

initial texture of ZXEM2000 is much weaker compared with those of the hot-rolled pure Mg and AZ31 (Figure A.5) [62], which leads to a more homogeneous deformation and consequently better ductility. The weakened texture of this alloy is a result of the alloying (i.e., Ca and Ce) and the well-designed thermomechanical processing [6]. Similarly, Sandlobe *et al.* [38] observed less intense basal texture in the hot-rolled Mg-Y alloy, which also leads to more homogeneous deformation and much-improved ductility compared with pure Mg. Moreover, we noticed that the RD tension led to a further texture weakening, as evidenced by comparing the PFs at various deformation stages (Figure 5.2). For example, the basal pole spreading is much more apparent in the fractured sample compared to the non-deformed counterpart. The further weakened texture also indicates the strong dislocation activities during RD tension, which results in the dislocation-assisted grain rotation [100, 121].

Second, the fine grain size could improve ductility. As shown in Figure 5.2 and Figure A.5, the grain size in the ZXEM2000 alloy (5.47 μm) is much smaller than the baseline materials (25.35 μm in pure Mg and 14.24 μm in AZ31 alloy) [62]. The finer grain size is resulted from the multi-stage rolling process. Moreover, the high density of uniformly dispersed precipitates could hinder grain boundary motion (Zener pinning), hence reduce grain growth during annealing [6]. Fine grain-sized Mg has been reported to exhibit improved ductility because the high volume fraction grain boundaries can reduce the critical resolve shear stress gaps among different slip systems (e.g., basal $< a >$ v.s. pyramidal $< c + a >$). This in turn leads to reduced plastic anisotropy and consequently improved ductility [122, 47, 123]. We note that the presence of fine precipitates has duo roles on ductility in our alloy. Dispersion of precipitates are known to have strengthening effect, but accompanied with the decreased ductility. On the other hand, the precipitates resulted in finer grains, which is beneficial to improved ductility. Since the ZXEM2000 alloys is much more ductile than pure Mg and AZ31, we infer that the precipitates do not significantly deteriorate the ductility and its effect to retain small grain size prevails.

Third, the reduced twinning can also contribute to the exceptional ductility. In contrast to the pure Mg and AZ31 (Figure A.7) [62], less apparent twins were observed even at the fracture

stage in this new alloy (Figure 5.2c). Since the twin-grain boundary and twin-twin interactions could create local stress concentration, they can act as crack nucleation sites [101, 102, 45]. The reduced twinning can delay fracture by avoiding twin-related local stress concentration. The lack of TTs in the post-deformed ZXEM2000 alloy is rather unexpected. This is because this alloy exhibits a weaker texture, which should encourage TT formation in the off-basal grains as they have higher twin Schmid factors. There are two possible reasons for the suppression of TT: i) Alloying elements (e.g., Ce) could reduce the CRSS of prismatic $< a >$ and pyramidal $< c + a >$ slips [38], rendering them competing with TT; ii) Smaller grain size in the ZXEM2000 could suppress the TT [62]. It is well known twinning is more difficult to activate in smaller grains [80, 57, 14]. Hence, the new alloy with smaller grain size has less propensity to twin.

Fourth, the increased cross-slip frequency of $< c + a >$ dislocation could lead to the improved ductility. As shown in Figure 5.4a, two representative TEM WBDF micrographs reveal different $< c >$ component morphologies by exciting the $[0002]$ reflection in the ZXEM2000 alloy and pure Mg. Noted the $< c >$ components are largely from the $< c + a >$ dislocations or decomposed from $< c + a >$ dislocations [11]. The $< c + a >$ dislocations are less inclined to bound on the basal planes in the ZXEM2000 alloy than pure Mg. Three micrographs from each sample were selected to statistically quantify such differences. As shown in the histogram (Figure 5.4b), the $< c + a >$ dislocations cross-slip frequency (the total non-basal-bound segment length divided by the basal-bounded segment length) in ZXEM2000 is approximately 7 times of that in pure Mg. In the pure Mg, Wu and Curtain [10] used molecular dynamics (MD) simulations and predicted the $< c + a >$ dislocation core is metastable and undergoes a thermal-assisted core transition from pyramidal to the basal plane. In this case, the alloying elements may modify the stacking fault energy and $< c + a >$ dislocation core stability, which may increase the energy barrier for such unfavored glissle-to-sessile transformation. Therefore, the $< c + a >$ dislocations in the new alloy are more mobile and could cross slip more frequently in the ZXEM2000 alloy, resulting in a more sustainable deformation.

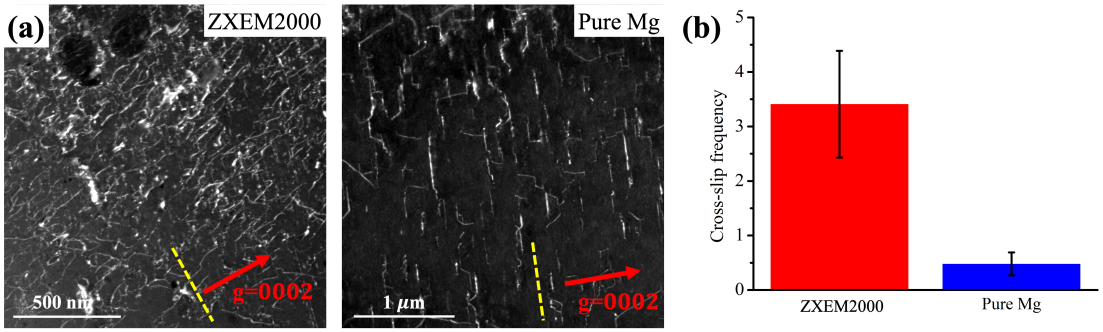

Figure 5.4: (a) Representative TEM WBDF micrographs (using $\mathbf{g} = [0002]$) revealing the $< c >$ component in ZXEM2000 and pure Mg. (b) Histogram showing the $< c + a >$ dislocations cross slip frequency (total non-basal-bound segment length divided by basal-bound segment length) for ZXEM2000 and pure Mg. Yellow dashed line perpendicular to the $[0002]$ **g** vector corresponds to the projection of basal planes.

5.5 Conclusions

The ZXEM2000 alloy exhibits excellent ductility compared to pure Mg and AZ31 under the rolling direction tension. Its microstructural evolution was systemically characterized at the granular and dislocation levels to understand the fundamental mechanisms that can contribute to the improved ductility. Based on the above observations, the four key factors are: (1) the weaker texture, (2) the finer grain size, (3) the reduced twinning, and (4) the increased cross-slip frequency of $< c + a >$ dislocation. This study provides new opportunities to advance the understanding of the deformation behavior of this class of ZXEM series alloys and guide the future Mg alloy design to achieve even better room-temperature ductility.

6. SUMMARY AND FUTURE WORK

In this defense, advanced characterization techniques (SEM, TEM, etc.) were used to study the activation and suppression of non-basal slips (non-basal $< a >$ and $< c + a >$) and extension twinning in deformed pure Mg and Mg alloys. Our observations revealed global Schmid factor prevails on $< c + a >$ slip, whereas the Schmid factors of individual grains govern the extension twinning. Meanwhile, alloying could modify the non-basal slip activities (either suppress or increase the cross-slip frequency) and reduce extension twinning. The fundamental mechanisms uncovered in this work are anticipated to help guide the future Mg alloy design, especially in the area of simultaneously achieving high strengthen, high ductility, and improved formability.

6.1 Review of Key Findings

The effect of Schmid factor on the activation and suppression of non-basal slip and extension twinning (highly-textured AZ31 alloy): 1. For $< c + a >$ dislocation, after normal-direction (close-to-c-axis) compression, $< c + a >$ dislocations are extensively activated even for those geometrically unfavored grains; However, the $< c + a >$ dislocations are suppressed even for those geometrically favored grains in the 45° off the normal-direction compression samples. These observations indicate the dislocation activation in polycrystalline materials behaves very differently from the single crystal. The activation and suppression of $< c + a >$ dislocations in individual grains are primarily dictated by the overall texture, rather than the crystallographic orientation of individual grains. 2. For extension twinning, after the deformation under various conditions (normal-direction compression and tension, rolling-direction compression and tension, and 45° compression), statistical analyses revealed extension twinning generally obeys the Schmid law for individual grains, regardless the global stress state favors extension twinning or not. The strong dependence of extension twinning on the Schmid factor is in contrast to the above weak correlation of $< c + a >$ dislocations and Schmid factor in the same material system.

The effect of non-RE alloying on the activation and suppression of non-basal slip and extension

twinning and their influence on the sample ductility (pure Mg and AZ31): Systematic tilting experiments and statistical analyses of multiple grains at different strain levels revealed a significant disparity of non-basal dislocation activities between pure Mg and AZ31. For pure Mg, $< c + a >$ dislocations were activated since the early stage of plastic deformation. The $< c + a >$ dislocations display a much shorter dissociation distance under tension as compared to the ones reported from c-axis compression. Increasing strain level appears to promote the cross slip of $< c + a >$ dislocations. For AZ31, $< c + a >$ dislocations were largely absent at all strain levels, even in the strain-to-failure samples. Non-basal $< a >$ dislocations, including prismatic and pyramidal $< a >$ dislocations, were observed. The promotion of the non-basal $< a >$ dislocation activities and the suppression of $< c + a >$ dislocations in AZ31 are expected to offer more sustainable hardening, which could elucidate the absence of apparent shear banding and much-improved ductility in AZ31 compared to pure Mg.

The effect of RE alloying on the activation and suppression of $< c + a >$ dislocation and extension twinning, and their influence on sample ductility (Mg–2Zn-0.3Ca-0.2Ce-0.1Mn): SEM and TEM were carried out at selected strain levels to characterize the microstructural evolution. Compared with the deformed microstructures from the hot-rolled pure Mg and AZ31 alloy at similar conditions, our results revealed that the high ductility of ZXEM2000 could be attributed to four key factors: weaker texture, fine grain size, reduced twinning, and increased cross-slip frequency of $< c + a >$ dislocation.

Here, we would like to compare the role of $< c + a >$ dislocations in AZ31 and ZXEM2000 alloys. In AZ31, the absence of the sessile $< c + a >$ dislocations could suppress shear banding and delay the early-stage fracture. In ZXEM2000, the promotion of glissile $< c+a >$ dislocations (higher cross-slip frequency) could provide sustainable and uniform deformation. Thus, we can conclude the suppression of sessile $< c + a >$ dislocations or the promotion of glissile $< c + a >$ dislocations are the two general strategies to improve the ductility in Mg alloys.

Taken together, this dissertation explores the roles of Schmid factor and alloying on the operation of non-basal slip and extension twinning in Mg and Mg alloy. Both above deformation

mechanisms have a significant impact on the ductility and formability of Mg and Mg alloys. The fundamental mechanisms uncovered in this work are anticipated to help guide the future Mg alloy design, especially in the area of simultaneously achieving high strengthen, high ductility, and improved formability.

6.2 Future Work

Equipped with the knowledge on the effect of Schmid factor and alloy elements on the non-basal $< a >$ and extension twinning activities, the future work should expand the investigation of deformation mechanisms in Mg to the mesoscale (e.g., shear banding) and in samples with chemical non-homogeneity (e.g., solute clustering).

6.2.1 Understanding shear banding in Mg and Mg alloys at dislocation level

Although $< c + a >$ dislocations in pure Mg can easily become immobile and quickly lose the ability to accommodate the c-axis compressive strain, Mg does not fail by direct crack opening like the brittle ceramic fracture. Instead, we noticed shear bands first develop in Mg from the pure Mg and AZ31 rolling-direction tensile testing (Figure 6.1). Cracks then nucleate and propagate along with the localized shear bands and lead to failure. Shear banding is a form of plastic instability, representing considerable plastic strain in thin microscopic bands even when the imposed macroscopic deformation is homogeneous. Shear banding occurs when the material cannot strain to harden in response to the external load. For Mg, several mechanisms have been proposed, suggesting the initiation and formation of shear bands (both localized and delocalized) could be associated with basal slip, contraction twinning, extension twinning, double twinning, or rotational/dynamic recrystallization. At room temperature, shear banding in Mg can develop under relatively high strain rates, as well as under quasi-static rates. The shear bands mostly go through multiple grains and are 50-100 μm thick. Most strain is stored in the shear bands, from which cracks can nucleate and grow and result in failure. There are some unique features about the shear bands in pure Mg. First, they are much thicker than the shear bands reported in nanocrystalline, nanotwinned, and nanolayered metals (in the range of tens or hundreds of nanometers). Second, shear bands

in pure Mg can form at low strain rates, suggesting they may not be adiabatic shear bands, and thermal softening may not be the predominant mechanism for strain localization. These peculiar characteristics render the shear bands in pure Mg scientifically interesting, and new deformation mechanisms may be discovered.

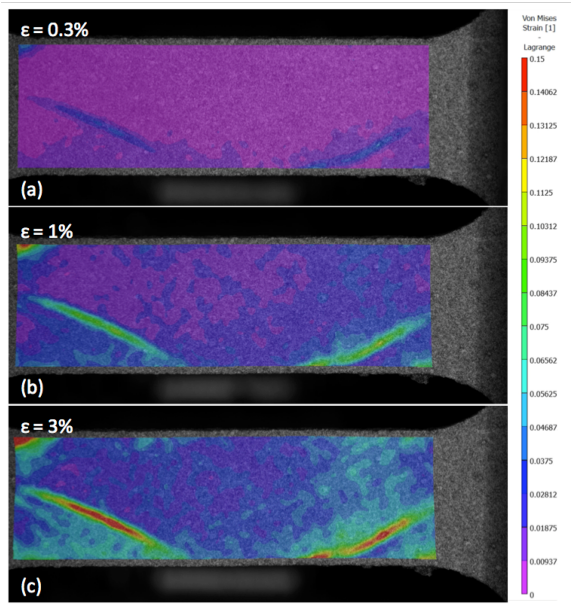

Figure 6.1: DIC results from a tensile test of a pure Mg sample at different stages deformed along the rolling direction. The color bar shows the Von Mises strain range, from 0 to 15%.

6.2.2 Investigating the atomic scale solute cluster interaction with dislocation in Mg alloy

Introducing precipitates is an effective method to engineer the mechanical properties of alloys. The profuse distribution of precipitates can impede dislocations and twins via the Orowan effect. A similar idea can be adapted to solute clusters, which can form by aging the solution-treated Mg alloys. Solute clusters do not have a well-defined crystallographic structure. Hence they cannot be categorized as precipitates. The solute segregates in the Mg matrix are expected to hinder the movement of dislocations. To date, limited work has focused on the solute clustering in Mg (in contrast to a large amount of literature on the solute cluster strengthening in Al alloys). Some recent work has demonstrated the high potency of cluster strengthening in Mg alloys. How dislocations

(e.g., basal $< a >$ and $< c + a >$) interact with the solute clusters is unknown. Recently, we chose Mg-Zn-Zr (ZK40) alloy as a model material to study the solute cluster strengthening effect. ZK40 alloys were first solution treated then aged at 200 °C for different durations. The atomic-level HAADF-STEM observation indicates the solute clusters segregate near the precipitate, but no solute clusters were observed in the matrix. We plan to move on to the Mg-Zn-Ca system, which has demonstrated the presence of Zn-Ca-rich clusters. Due to the high number density and, consequently, the small inter-cluster distance, cluster strengthening is anticipated to further increase the strength to a level that cannot be achieved through the classical solid solution and precipitate strengthening.

REFERENCES

[1] "Renault's eolab shines at 2015 seoul motor show," Apr 2015.

[2] M. Crider, "Next-gen laptop materials: Aluminum alloy vs. magnesium alloy vs. carbon fiber," Jun 2017.

[3] L. Ma, K. Xie, J. Cai, and K. J. Hemker, "Non-dissociated dislocations in an AZ31 alloy revealed by transmission electron microscopy," *Materials Research Letters*, vol. 8, pp. 145–150, Apr. 2020.

[4] H. F. Alharbi, M. Luqman, E. El-Danaf, and N. H. Alharthi, "Experimental and numerical study of texture evolution and anisotropic plastic deformation of pure magnesium under various strain paths," *Advances in Materials Science and Engineering*, vol. 2018, 2018.

[5] S. Sandlöbes, M. Friák, S. Korte-Kerzel, Z. Pei, J. Neugebauer, and D. Raabe, "A rare-earth free magnesium alloy with improved intrinsic ductility," *Scientific Reports*, vol. 7, p. 10458, Dec. 2017.

[6] R. Shi, J. Miao, and A. A. Luo, "A new magnesium sheet alloy and its multi-stage homogenization for simultaneously improved ductility and strength at room temperature," *Scripta Materialia*, vol. 171, pp. 92–97, Oct. 2019.

[7] T. Obara, H. Yoshinga, and S. Morozumi, "11-22<-1-123> slip system in magnesium," *Acta Metallurgica*, vol. 21, no. 7, pp. 845–853, 1973.

[8] S. R. Agnew and Ö. Duygulu, "Plastic anisotropy and the role of non-basal slip in magnesium alloy az31b," *International Journal of plasticity*, vol. 21, no. 6, pp. 1161–1193, 2005.

[9] J. Geng, M. Chisholm, R. Mishra, and K. Kumar, "An electron microscopy study of dislocation structures in Mg single crystals compressed along [0 0 0 1] at room temperature," *Philosophical Magazine*, vol. 95, pp. 3910–3932, Dec. 2015.

[10] Z. Wu and W. A. Curtin, "The origins of high hardening and low ductility in magnesium," *Nature*, vol. 526, pp. 62–67, Oct. 2015.

[11] K. Y. Xie, K. M. Reddy, L. Ma, A. Caffee, M. Chen, and K. J. Hemker, "Experimental observations of the mechanisms associated with the high hardening and low strain to failure of magnesium," *Materialia*, p. 100504, Oct. 2019.

[12] M. Barnett, "Twinning and the ductility of magnesium alloys," *Materials Science and Engineering: A*, vol. 464, pp. 1–7, Aug. 2007.

[13] S.-G. Hong, S. H. Park, and C. S. Lee, "Role of {10–12} twinning characteristics in the deformation behavior of a polycrystalline magnesium alloy," *Acta Materialia*, vol. 58, pp. 5873–5885, Oct. 2010.

[14] I. Beyerlein, L. Capolungo, P. Marshall, R. McCabe, and C. Tomé, "Statistical analyses of deformation twinning in magnesium," *Philosophical Magazine*, vol. 90, pp. 2161–2190, May 2010.

[15] "Fuel consumption of cars and vans – analysis," Jun 2020.

[16] "Cold rolling the aluminum sheet."

[17] J. Zhang and S. P. Joshi, "Phenomenological crystal plasticity modeling and detailed micromechanical investigations of pure magnesium," *Journal of the Mechanics and Physics of Solids*, vol. 60, pp. 945–972, May 2012.

[18] D. Hull and D. J. Bacon, *Introduction to dislocations*. Amsterdam: Elsevier/Butterworth-Heinemann, 5. ed ed., 2011. OCLC: 704891549.

[19] H. Yoshinaga and R. Horiuchi, "Deformation Mechanisms in Magnesium Single Crystals Compressed in the Direction Parallel to Hexagonal Axis," *Transactions of the Japan Institute of Metals*, vol. 4, no. 1, pp. 1–8, 1963.

[20] A. Akhtar and E. Teghtsoonian, "Solid solution strengthening of magnesium single crystals—ii the effect of solute on the ease of prismatic slip," *Acta Metallurgica*, vol. 17, pp. 1351–1356, Nov. 1969.

[21] H. Yoshinaga and R. Horiuchi, "On the Nonbasal Slip in Magnesium Crystals," *Transactions of the Japan Institute of Metals*, vol. 5, no. 1, pp. 14–21, 1964.

[22] K. Y. Xie, Z. Alam, A. Caffee, and K. J. Hemker, "Pyramidal I slip in c-axis compressed Mg single crystals," *Scripta Materialia*, vol. 112, pp. 75–78, Feb. 2016.

[23] J. Geng, M. Chisholm, R. Mishra, and K. Kumar, "The structure of <c+a> type dislocation loops in magnesium," *Philosophical Magazine Letters*, vol. 94, pp. 377–386, June 2014.

[24] J. F. Stohr and J. P. Poirier, "Etude en microscopie electronique du glissement pyramidal {1122} <1123> dans le magnesium," *Philosophical Magazine*, vol. 25, pp. 1313–1329, June 1972.

[25] B. Syed, J. Geng, R. Mishra, and K. Kumar, "[0001] Compression response at room temperature of single-crystal magnesium," *Scripta Materialia*, vol. 67, pp. 700–703, Oct. 2012.

[26] S. R. Agnew, J. A. Horton, and M. H. Yoo, "Transmission electron microscopy investigation of <c+a> dislocations in Mg and α-solid solution Mg-Li alloys," *Metallurgical and Materials Transactions A*, vol. 33, pp. 851–858, Mar. 2002.

[27] Z. Wu, R. Ahmad, B. Yin, S. Sandlöbes, and W. A. Curtin, "Mechanistic origin and prediction of enhanced ductility in magnesium alloys," *Science*, vol. 359, pp. 447–452, Jan. 2018.

[28] S. Sandlöbes, M. Friák, S. Zaefferer, A. Dick, S. Yi, D. Letzig, Z. Pei, L.-F. Zhu, J. Neugebauer, and D. Raabe, "The relation between ductility and stacking fault energies in Mg and Mg–Y alloys," *Acta Materialia*, vol. 60, pp. 3011–3021, Apr. 2012.

[29] J. Koike, T. Kobayashi, T. Mukai, H. Watanabe, M. Suzuki, K. Maruyama, and K. Higashi, "The activity of non-basal slip systems and dynamic recovery at room temperature in fine-grained AZ31B magnesium alloys," *Acta Materialia*, vol. 51, pp. 2055–2065, Apr. 2003.

[30] T. Mukai, M. Yamanoi, H. Watanabe, and K. Higashi, "Ductility enhancement in AZ31 magnesium alloy by controlling its grain structure," *Scripta Materialia*, vol. 45, pp. 89–94, July 2001.

[31] A. A. Luo, "Recent Magnesium Alloy Development for Automotive Powertrain Applications," *Materials Science Forum*, vol. 419-422, pp. 57–66, Mar. 2003.

[32] S. Sandlöbes, M. Friák, J. Neugebauer, and D. Raabe, "Basal and non-basal dislocation slip in Mg–Y," *Materials Science and Engineering: A*, vol. 576, pp. 61–68, Aug. 2013.

[33] G. Zhu, L. Wang, H. Zhou, J. Wang, Y. Shen, P. Tu, H. Zhu, W. Liu, P. Jin, and X. Zeng, "Improving ductility of a Mg alloy via non-basal slip induced by Ca addition," *International Journal of Plasticity*, vol. 120, pp. 164–179, Sept. 2019.

[34] X. Luo, Z. Feng, T. Yu, J. Luo, T. Huang, G. Wu, N. Hansen, and X. Huang, "Transitions in mechanical behavior and in deformation mechanisms enhance the strength and ductility of Mg-3Gd," *Acta Materialia*, vol. 183, pp. 398–407, Jan. 2020.

[35] Z. Huang, L. Wang, B. Zhou, T. Fischer, S. Yi, and X. Zeng, "Observation of non-basal slip in Mg-Y by in situ three-dimensional X-ray diffraction," *Scripta Materialia*, vol. 143, pp. 44–48, Jan. 2018.

[36] X. Ma, Q. Jiao, L. J. Kecskes, J. A. El-Awady, and T. P. Weihs, "Effect of basal precipitates on extension twinning and pyramidal slip: A micro-mechanical and electron microscopy study of a Mg–Al binary alloy," *Acta Materialia*, vol. 189, pp. 35–46, May 2020.

[37] J. Koike, "Enhanced deformation mechanisms by anisotropic plasticity in polycrystalline Mg alloys at room temperature," *Metallurgical and Materials Transactions A*, vol. 36, pp. 1689–1696, July 2005.

[38] S. Sandlöbes, S. Zaefferer, I. Schestakow, S. Yi, and R. Gonzalez-Martinez, "On the role of non-basal deformation mechanisms for the ductility of Mg and Mg–Y alloys," *Acta Materialia*, vol. 59, pp. 429–439, Jan. 2011.

[39] Z. Wu and W. Curtin, "Intrinsic structural transitions of the pyramidal I < c + a > dislocation in magnesium," *Scripta Materialia*, vol. 116, pp. 104–107, Apr. 2016.

[40] W. H. E.W. Kelley, "Plane-strain compression of magnesium and magnesium alloy crystals," *Trans. Metall. Soc.*, vol. 242, pp. 5–13, 1968.

[41] W. H. E.W. Kelley, "The deformation characteristics of textured magnesium," *Trans. Metall. Soc.*, vol. 242, pp. 654–661, 1968.

[42] B.-Y. Liu, F. Liu, N. Yang, X.-B. Zhai, L. Zhang, Y. Yang, B. Li, J. Li, E. Ma, J.-F. Nie, and Z.-W. Shan, "Large plasticity in magnesium mediated by pyramidal dislocations," *Science*, vol. 365, pp. 73–75, July 2019.

[43] Y. Tang and J. A. El-Awady, "Formation and slip of pyramidal dislocations in hexagonal close-packed magnesium single crystals," *Acta Materialia*, vol. 71, pp. 319–332, June 2014.

[44] V. Herrera-Solaz, J. LLorca, E. Dogan, I. Karaman, and J. Segurado, "An inverse optimization strategy to determine single crystal mechanical behavior from polycrystal tests: Application to AZ31 Mg alloy," *International Journal of Plasticity*, vol. 57, pp. 1–15, June 2014.

[45] M. Vaughan, W. Nasim, E. Dogan, J. Herrington, G. Proust, A. Benzerga, and I. Karaman, "Interplay between the effects of deformation mechanisms and dynamic recrystallization on the failure of Mg-3Al-1Zn," *Acta Materialia*, vol. 168, pp. 448–472, Apr. 2019.

[46] X.-L. Nan, H.-Y. Wang, L. Zhang, J.-B. Li, and Q.-C. Jiang, "Calculation of Schmid factors in magnesium: Analysis of deformation behaviors," *Scripta Materialia*, vol. 67, pp. 443–446, Sept. 2012.

[47] W. Hutchinson and M. Barnett, "Effective values of critical resolved shear stress for slip in polycrystalline magnesium and other hcp metals," *Scripta Materialia*, vol. 63, pp. 737–740, Oct. 2010.

[48] K. Hazeli, J. Cuadra, P. Vanniamparambil, and A. Kontsos, "In situ identification of twin-related bands near yielding in a magnesium alloy," *Scripta Materialia*, vol. 68, pp. 83–86, Jan. 2013.

[49] H. El Kadiri, C. D. Barrett, J. Wang, and C. N. Tomé, "Why are { 10 1 $^{-}$ 2 } twins profuse in magnesium?," *Acta Materialia*, vol. 85, pp. 354–361, Feb. 2015.

[50] K. D. Molodov, T. Al-Samman, D. A. Molodov, and S. Korte-Kerzel, "On the twinning shear of { 10 1 $^{-}$ 2 } twins in magnesium – Experimental determination and formal description," *Acta Materialia*, vol. 134, pp. 267–273, Aug. 2017.

[51] N. Dixit, K. Y. Xie, K. J. Hemker, and K. Ramesh, "Microstructural evolution of pure magnesium under high strain rate loading," *Acta Materialia*, vol. 87, pp. 56–67, Apr. 2015.

[52] A. Khosravani, D. Fullwood, B. Adams, T. Rampton, M. Miles, and R. Mishra, "Nucleation and propagation of { 1 0 1 $^{-}$ 2 } twins in AZ31 magnesium alloy," *Acta Materialia*, vol. 100, pp. 202–214, Nov. 2015.

[53] J. Jiang, A. Godfrey, W. Liu, and Q. Liu, "Microtexture evolution via deformation twinning and slip during compression of magnesium alloy AZ31," *Materials Science and Engineering: A*, vol. 483-484, pp. 576–579, June 2008.

[54] Y. Xin, M. Wang, Z. Zeng, M. Nie, and Q. Liu, "Strengthening and toughening of magnesium alloy by {10-12} extension twins," *Scripta Materialia*, vol. 66, pp. 25–28, Jan. 2012.

[55] D. Zhao, R. Shi, P. Evans, A. A. Luo, and K. Y. Xie, "On the exceptionally high ductility of mg–2zn-0.3 ca-0.2 ce-0.1 mn alloy," *Materials Science and Engineering: A*, p. 141484, 2021.

[56] M. Barnett, A. Ghaderi, J. Quinta da Fonseca, and J. Robson, "Influence of orientation on twin nucleation and growth at low strains in a magnesium alloy," *Acta Materialia*, vol. 80, pp. 380–391, Nov. 2014.

[57] M. Barnett, "A rationale for the strong dependence of mechanical twinning on grain size," *Scripta Materialia*, vol. 59, pp. 696–698, Oct. 2008.

[58] M. Arul Kumar, I. J. Beyerlein, R. J. McCabe, and C. N. Tomé, "Grain neighbour effects on twin transmission in hexagonal close-packed materials," *Nature Communications*, vol. 7, p. 13826, Dec. 2016.

[59] Y. Pei, A. Godfrey, J. Jiang, Y. Zhang, W. Liu, and Q. Liu, "Extension twin variant selection during uniaxial compression of a magnesium alloy," *Materials Science and Engineering: A*, vol. 550, pp. 138–145, July 2012.

[60] S. Godet, L. Jiang, A. Luo, and J. Jonas, "Use of Schmid factors to select extension twin variants in extruded magnesium alloy tubes," *Scripta Materialia*, vol. 55, pp. 1055–1058, Dec. 2006.

[61] B. Lee, W. Chu, and W. Li, "Effects of process parameters on graphene growth via low-pressure chemical vapor deposition," *Journal of Micro-and Nano-Manufacturing*, vol. 8, no. 3, p. 031005, 2020.

[62] D. Zhao, X. Ma, A. Srivastava, G. Turner, I. Karaman, and K. Y. Xie, "Significant disparity of non-basal dislocation activities in hot-rolled highly-textured Mg and Mg-3Al-1Zn alloy under tension," *Acta Materialia*, p. 116691, Jan. 2021.

[63] J. Čapek, K. Máthis, B. Clausen, and M. Barnett, "Dependence of twinned volume fraction on loading mode and Schmid factor in randomly textured magnesium," *Acta Materialia*, vol. 130, pp. 319–328, May 2017.

[64] F. Bachmann, R. Hielscher, and H. Schaeben, "Texture Analysis with MTEX – Free and Open Source Software Toolbox," *Solid State Phenomena*, vol. 160, pp. 63–68, Feb. 2010.

[65] D. Zhao, X. Ma, S. Picak, I. Karaman, and K. Xie, "Activation and suppression of <c+a> dislocations in a textured Mg–3Al–1Zn alloy," *Scripta Materialia*, vol. 179, pp. 49–54, Apr. 2020.

[66] X. Wang, P. Mao, Z. Liu, Z. Wang, F. Wang, L. Zhou, and Z. Wei, "Nucleation and growth analysis of {10-12} extension twins in AZ31 magnesium alloy during in-situ tension," *Journal of Alloys and Compounds*, vol. 817, p. 152967, Mar. 2020.

[67] J. J. Jonas, S. Mu, T. Al-Samman, G. Gottstein, L. Jiang, and Ė. Martin, "The role of strain accommodation during the variant selection of primary twins in magnesium," *Acta Materialia*, vol. 59, no. 5, pp. 2046–2056, 2011.

[68] P. Chen, B. Li, D. Culbertson, and Y. Jiang, "Negligible effect of twin-slip interaction on hardening in deformation of a Mg-3Al-1Zn alloy," *Materials Science and Engineering: A*, vol. 729, pp. 285–293, June 2018.

[69] A. Akhtar and E. Teghtsoonian, "Solid solution strengthening of magnesium single crystals—I alloying behaviour in basal slip," *Acta Metallurgica*, vol. 17, pp. 1339–1349, Nov. 1969.

[70] A. Couret and D. Caillard, "An in situ study of prismatic glide in magnesium—I. The rate controlling mechanism," *Acta Metallurgica*, vol. 33, pp. 1447–1454, Aug. 1985.

[71] A. Couret and D. Caillard, "An in situ study of prismatic glide in magnesium—II. Microscopic activation parameters," *Acta Metallurgica*, vol. 33, pp. 1455–1462, Aug. 1985.

[72] K. Srivastava, S. I. Rao, and J. A. El-Awady, "Unveiling the role of super-jogs and dislocation induced atomic-shuffling on controlling plasticity in magnesium," *Acta Materialia*, vol. 161, pp. 182–193, Dec. 2018.

[73] D. Buey, L. Hector, and M. Ghazisaeidi, "Core structure and solute strengthening of second-order pyramidal < c + a > dislocations in Mg-Y alloys," *Acta Materialia*, vol. 147, pp. 1–9, Apr. 2018.

[74] T. Nogaret, W. Curtin, J. Yasi, L. Hector, and D. Trinkle, "Atomistic study of edge and screw <c+a> dislocations in magnesium," *Acta Materialia*, vol. 58, pp. 4332–4343, Aug. 2010.

[75] D. R. Trinkle, "The Chemistry of Deformation: How Solutes Soften Pure Metals," *Science*, vol. 310, pp. 1665–1667, Dec. 2005.

[76] R. Ahmad, B. Yin, Z. Wu, and W. Curtin, "Designing high ductility in magnesium alloys," *Acta Materialia*, vol. 172, pp. 161–184, June 2019.

[77] H. Fan, Q. Wang, X. Tian, and J. A. El-Awady, "Temperature effects on the mobility of pyramidal < c + a > dislocations in magnesium," *Scripta Materialia*, vol. 127, pp. 68–71, Jan. 2017.

[78] K. Srivastava and J. A. El-Awady, "Deformation of magnesium during c-axis compression at low temperatures," *Acta Materialia*, vol. 133, pp. 282–292, July 2017.

[79] R. Ahmad, Z. Wu, S. Groh, and W. Curtin, "Pyramidal II to basal transformation of $\langle + \rangle$ edge dislocations in Mg-Y alloys," *Scripta Materialia*, vol. 155, pp. 114–118, Oct. 2018.

[80] M. Barnett, Z. Keshavarz, A. Beer, and D. Atwell, "Influence of grain size on the compressive deformation of wrought Mg–3Al–1Zn," *Acta Materialia*, vol. 52, pp. 5093–5103, Oct. 2004.

[81] H.-S. Jang and B.-J. Lee, "Effects of Zn on <c+a> slip and grain boundary segregation of Mg alloys," *Scripta Materialia*, vol. 160, pp. 39–43, Feb. 2019.

[82] D. Zhang, H. Wen, M. A. Kumar, F. Chen, L. Zhang, I. J. Beyerlein, J. M. Schoenung, S. Mahajan, and E. J. Lavernia, "Yield symmetry and reduced strength differential in Mg-2.5Y alloy," *Acta Materialia*, vol. 120, pp. 75–85, Nov. 2016.

[83] F. Wang, K. Hazeli, K. Molodov, C. Barrett, T. Al-Samman, D. Molodov, A. Kontsos, K. Ramesh, H. El Kadiri, and S. Agnew, "Characteristic dislocation substructure in 10 1 $^{-}$ 2 twins in hexagonal metals," *Scripta Materialia*, vol. 143, pp. 81–85, Jan. 2018.

[84] J. Kang, D. S. Wilkinson, and R. K. Mishra, "Inhomogeneous deformation of az31 magnesium sheet in uniaxial tension," in *Magnesium Technology 2011*, pp. 307–311, Springer, 2011.

[85] J. Scott, M. Miles, D. Fullwood, B. Adams, A. Khosravani, and R. K. Mishra, "Room Temperature Shear Band Development in Highly Twinned Wrought Magnesium AZ31B Sheet," *Metallurgical and Materials Transactions A*, vol. 44, pp. 512–516, Jan. 2013.

[86] J. M. Scott, "Failure mechanisms and texture evolution of wrought az31b magnesium at temperatures ranging from 25 c to 125 c," 2012.

[87] P. F. Rottmann and K. J. Hemker, "Nanoscale elastic strain mapping of polycrystalline materials," *Materials Research Letters*, vol. 6, pp. 249–254, Apr. 2018.

[88] E. F. Rauch and M. Véron, "Virtual dark-field images reconstructed from electron diffraction patterns," *The European Physical Journal Applied Physics*, vol. 66, p. 10701, Apr. 2014.

[89] X. Ma, D. Zhao, S. Yadav, D. Sagapuram, and K. Y. Xie, "Grain-subdivision-dominated microstructure evolution in shear bands at high rates," *Materials Research Letters*, vol. 8, pp. 328–334, Sept. 2020.

[90] E. Dogan, I. Karaman, G. Ayoub, and G. Kridli, "Reduction in tension–compression asymmetry via grain refinement and texture design in Mg–3Al–1Zn sheets," *Materials Science and Engineering: A*, vol. 610, pp. 220–227, July 2014.

[91] S. Razavi, D. Foley, I. Karaman, K. Hartwig, O. Duygulu, L. Kecskes, S. Mathaudhu, and V. Hammond, "Effect of grain size on prismatic slip in Mg–3Al–1Zn alloy," *Scripta Materialia*, vol. 67, pp. 439–442, Sept. 2012.

[92] Y. Chen, L. Hu, L. Shi, T. Zhou, J. Tu, Q. Chen, and M. Yang, "Effect of texture types on microstructure evolution and mechanical properties of AZ31 magnesium alloy undergoing uniaxial tension deformation at room temperature," *Materials Science and Engineering: A*, vol. 769, p. 138497, Jan. 2020.

[93] C. M. Byer, B. Li, B. Cao, and K. Ramesh, "Microcompression of single-crystal magnesium," *Scripta Materialia*, vol. 62, pp. 536–539, Apr. 2010.

[94] S. Agnew, M. Yoo, and C. Tomé, "Application of texture simulation to understanding mechanical behavior of Mg and solid solution alloys containing Li or Y," *Acta Materialia*, vol. 49, pp. 4277–4289, Dec. 2001.

[95] A. Fernández, M. T. Pérez Prado, Y. Wei, and A. Jérusalem, "Continuum modeling of the response of a Mg alloy AZ31 rolled sheet during uniaxial deformation," *International Journal of Plasticity*, vol. 27, pp. 1739–1757, Nov. 2011.

[96] H. Wang, B. Raeisinia, P. Wu, S. Agnew, and C. Tomé, "Evaluation of self-consistent polycrystal plasticity models for magnesium alloy AZ31B sheet," *International Journal of Solids and Structures*, vol. 47, pp. 2905–2917, Oct. 2010.

[97] R. E. Reed-Hill and W. D. Robertson, "Deformation of magnesium single crystals by nonbasal slip," *JOM*, vol. 9, pp. 496–502, Apr. 1957.

[98] P. G. Partridge, "The crystallography and deformation modes of hexagonal close-packed metals," *Metallurgical Reviews*, vol. 12, pp. 169–194, Jan. 1967.

[99] J. F. Nie, K. S. Shin, and Z. R. Zeng, "Microstructure, Deformation, and Property of Wrought Magnesium Alloys," *Metallurgical and Materials Transactions A*, Oct. 2020.

[100] T. Mayama, M. Noda, R. Chiba, and M. Kuroda, "Crystal plasticity analysis of texture development in magnesium alloy during extrusion," *International Journal of Plasticity*, vol. 27, pp. 1916–1935, Dec. 2011.

[101] D. Ando, J. Koike, and Y. Sutou, "The role of deformation twinning in the fracture behavior and mechanism of basal textured magnesium alloys," *Materials Science and Engineering: A*, vol. 600, pp. 145–152, Apr. 2014.

[102] H. Somekawa, K. Nakajima, A. Singh, and T. Mukai, "Ductile fracture mechanism in fine-grained magnesium alloy," *Philosophical Magazine Letters*, vol. 90, pp. 831–839, Nov. 2010.

[103] L. Wang, Z. Huang, H. Wang, A. Maldar, S. Yi, J.-S. Park, P. Kenesei, E. Lilleodden, and X. Zeng, "Study of slip activity in a Mg-Y alloy by in situ high energy X-ray diffraction microscopy and elastic viscoplastic self-consistent modeling," *Acta Materialia*, vol. 155, pp. 138–152, Aug. 2018.

[104] J. Koike and R. Ohyama, "Geometrical criterion for the activation of prismatic slip in AZ61 Mg alloy sheets deformed at room temperature," *Acta Materialia*, vol. 53, pp. 1963–1972, Apr. 2005.

[105] A. Luo, "Recent magnesium alloy development for elevated temperature applications," *International Materials Reviews*, vol. 49, pp. 13–30, Feb. 2004.

[106] T. M. Pollock, "Weight Loss with Magnesium Alloys," *Science*, vol. 328, pp. 986–987, May 2010.

[107] S. Agnew and J. Nie, "Preface to the viewpoint set on: The current state of magnesium alloy science and technology," *Scripta Materialia*, vol. 63, pp. 671–673, Oct. 2010.

[108] A. A. Luo, "Magnesium: Current and potential automotive applications," *JOM*, vol. 54, pp. 42–48, Feb. 2002.

[109] A. A. Luo, B. R. Powell, and A. K. Sachdev, "Computational phase equilibria and experimental investigation of magnesium–aluminum–calcium alloys," *Intermetallics*, vol. 24, pp. 22–29, May 2012.

[110] G. Proust, "Processing magnesium at room temperature," *Science*, vol. 365, pp. 30–31, July 2019.

[111] M. Barnett, M. Nave, and C. Bettles, "Deformation microstructures and textures of some cold rolled Mg alloys," *Materials Science and Engineering A*, vol. 386, pp. 205–211, Nov. 2004.

[112] T. T. T. Trang, J. H. Zhang, J. H. Kim, A. Zargaran, J. H. Hwang, B.-C. Suh, and N. J. Kim, "Designing a magnesium alloy with high strength and high formability," *Nature Communications*, vol. 9, p. 2522, Dec. 2018.

[113] J. Barnard, A. Eggeman, J. Sharp, T. White, and P. Midgley, "Dislocation electron tomography and precession electron diffraction – minimising the effects of dynamical interactions in real and reciprocal space," *Philosophical Magazine*, vol. 90, pp. 4711–4730, Dec. 2010.

[114] Z. Zhang, A. Couture, and A. Luo, "An investigation of the properties of Mg-Zn-Al alloys," *Scripta Materialia*, vol. 39, pp. 45–53, June 1998.

[115] N. Stanford and M. Barnett, "Effect of composition on the texture and deformation behaviour of wrought Mg alloys," *Scripta Materialia*, vol. 58, pp. 179–182, Feb. 2008.

[116] I. Basu, T. Al-Samman, and G. Gottstein, "Shear band-related recrystallization and grain growth in two rolled magnesium-rare earth alloys," *Materials Science and Engineering: A*, vol. 579, pp. 50–56, Sept. 2013.

[117] J.-Y. Lee, Y.-S. Yun, W.-T. Kim, and D.-H. Kim, "Twinning and texture evolution in binary Mg-Ca and Mg-Zn alloys," *Metals and Materials International*, vol. 20, pp. 885–891, Sept. 2014.

[118] N. Stanford and M. Barnett, "The origin of "rare earth" texture development in extruded Mg-based alloys and its effect on tensile ductility," *Materials Science and Engineering: A*, vol. 496, pp. 399–408, Nov. 2008.

[119] S. Tekumalla, S. Seetharaman, A. Almajid, and M. Gupta, "Mechanical Properties of Magnesium-Rare Earth Alloy Systems: A Review," *Metals*, vol. 5, pp. 1–39, Dec. 2014.

[120] B. Pourbahari, H. Mirzadeh, M. Emamy, and R. Roumina, "Enhanced Ductility of a Fine-Grained Mg-Gd-Al-Zn Magnesium Alloy by Hot Extrusion," *Advanced Engineering Materials*, vol. 20, p. 1701171, Aug. 2018.

[121] T. Mayama, K. Aizawa, Y. Tadano, and M. Kuroda, "Influence of twinning deformation and lattice rotation on strength differential effect in polycrystalline pure magnesium with rolling texture," *Computational Materials Science*, vol. 47, pp. 448–455, Dec. 2009.

[122] K. Wei, R. Hu, D. Yin, L. Xiao, S. Pang, Y. Cao, H. Zhou, Y. Zhao, and Y. Zhu, "Grain size effect on tensile properties and slip systems of pure magnesium," *Acta Materialia*, vol. 206, p. 116604, Mar. 2021.

[123] Q. Yu, L. Qi, R. K. Mishra, J. Li, and A. M. Minor, "Reducing deformation anisotropy to achieve ultrahigh strength and ductility in Mg at the nanoscale," *Proceedings of the National Academy of Sciences*, vol. 110, pp. 13289–13293, Aug. 2013.

APPENDIX A

SUPPLEMENTARY DATA

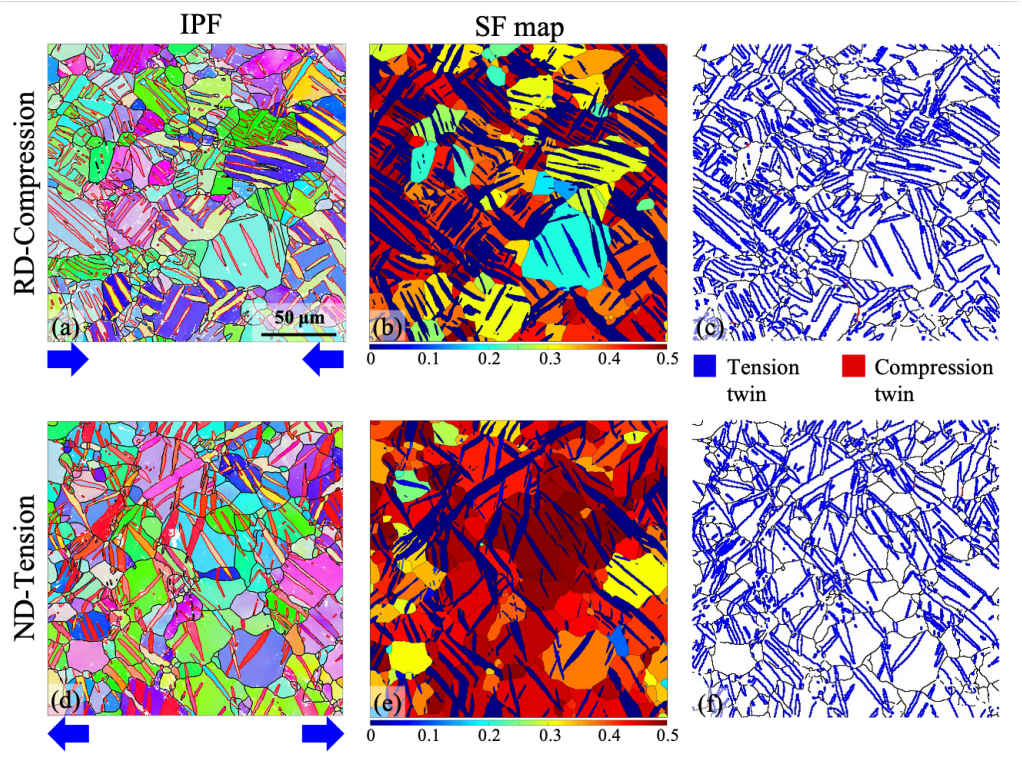

Figure A.1: (a) (d) EBSD IPF maps (out-of-plane crystal orientation) of the highly textured AZ31 alloy deformed under twinning-favored conditions (rolling direction (RD) compression and normal direction (ND) tension); (b) (e) Tension twin (TT) Schmid factor (SF) maps created based on the IPF maps and loading directions; (c) (f) Tension twin (blue) and compression twin (red) distribution.

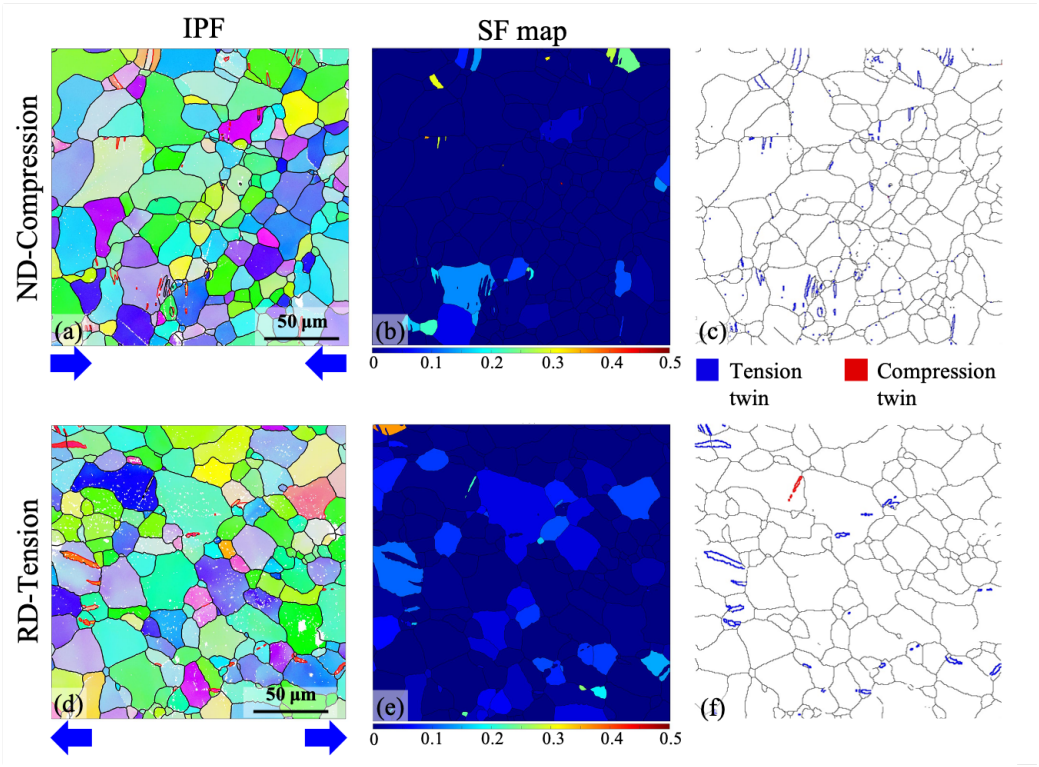

Figure A.2: (a) (d) EBSD IPF maps (out-of-plane crystal orientation) of the highly textured AZ31 alloy deformed under twinning-unfavored conditions (normal direction (ND) compression and rolling direction (RD) tension); (b) (e) Tension twin (TT) Schmid factor (SF) maps created based on the IPF maps and loading directions; (c) (f) Tension twin (blue) and compression twin (red) distribution.

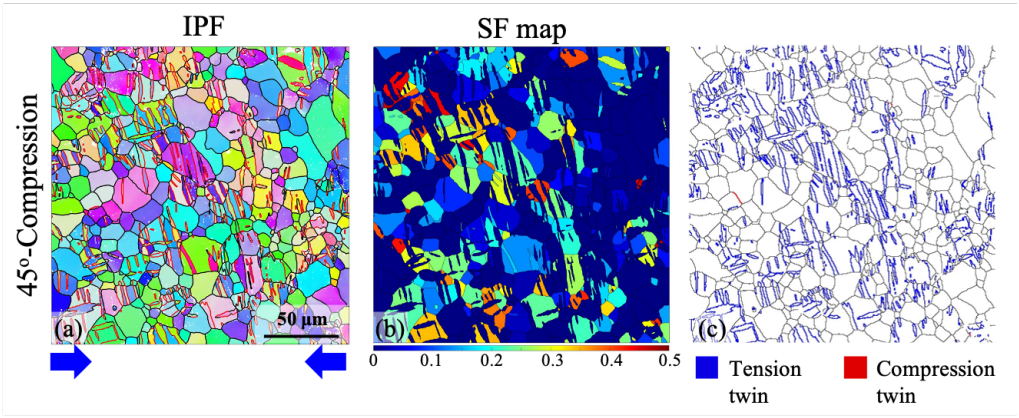

Figure A.3: (a) EBSD IPF maps (out-of-plane crystal orientation) of the highly textured AZ31 alloy deformed under 45° off normal direction compression (45° Compression); (b) Tension twin (TT) Schmid factor (SF) maps created based on the IPF maps and loading directions; (c) Tension twin (blue) and compression twin (red) distribution.

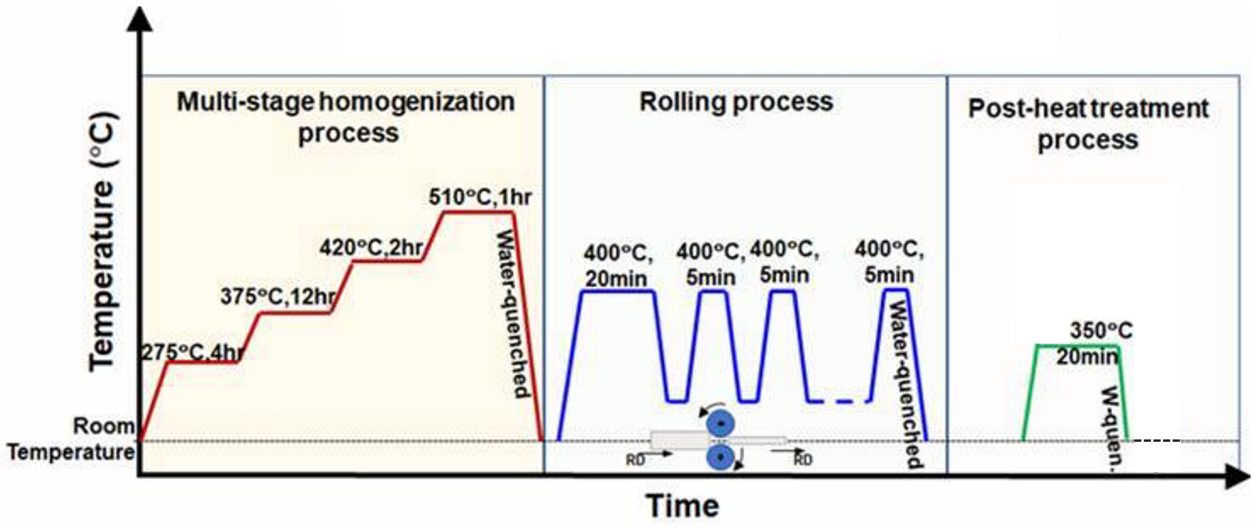

Figure A.4: The thermal process window for ZXEM2000 alloy.

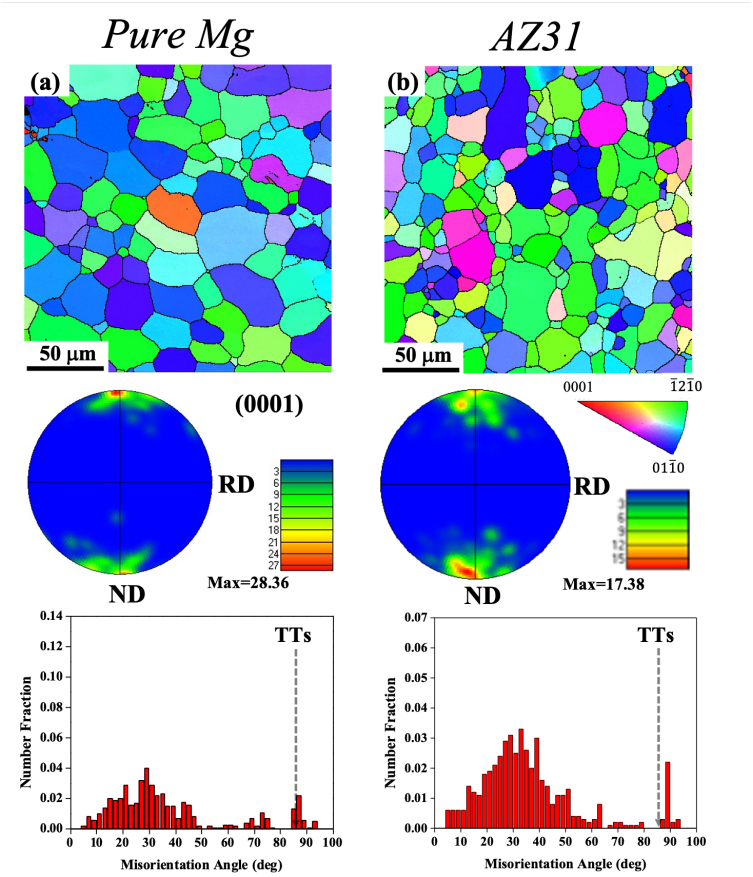

Figure A.5: EBSD IPF maps (out-of-plane crystal orientation) of initial (a) pure Mg and (b) AZ31 microstructures, along with the corresponding (0001) pole figures and misorientation angle distributions.

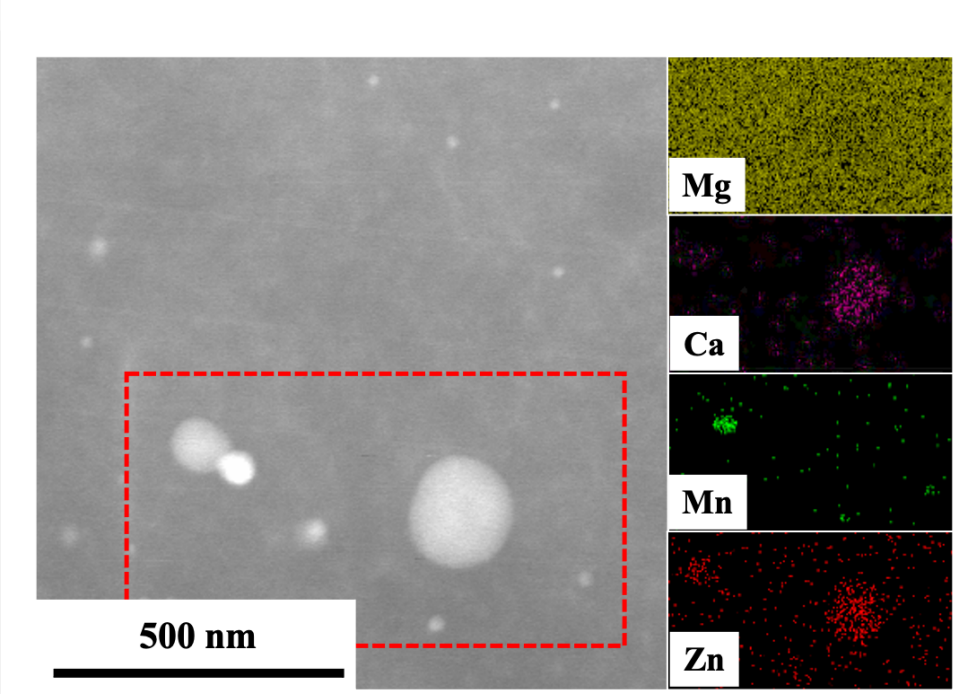

Figure A.6: HADDF-STEM image of precipitates and the corresponding STEM-EDS map.

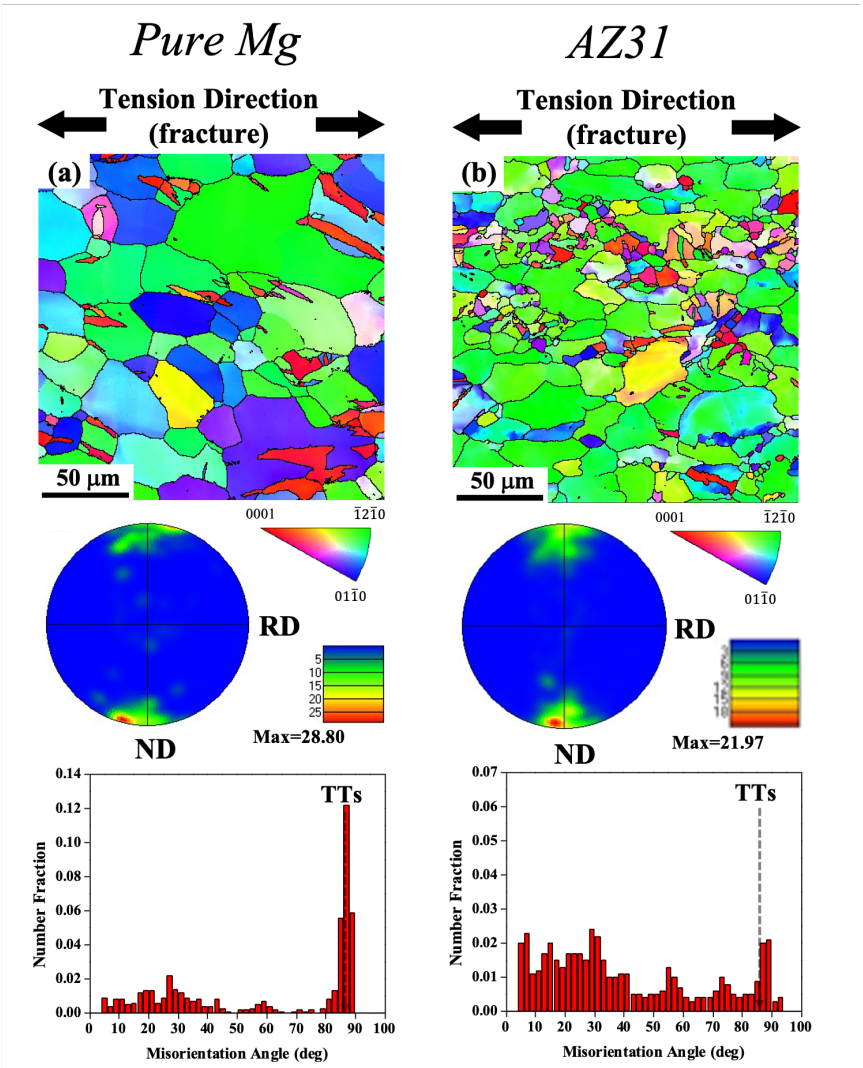

Figure A.7: EBSD IPF maps (out-of-plane crystal orientation) of (a) fractured pure Mg and (b) AZ31 microstructures, along with the corresponding (0001) pole figures and misorientation angle distributions.